

Copyright  
by  
Michael Drew Gammage  
2016

**The Dissertation Committee for Michael Drew Gammage Certifies that this is the approved version of the following dissertation:**

**LAMA-Produced Metal-on-Oxide Nanoparticles and Films**

**Committee:**

---

Desiderio Kovar, Supervisor

---

Michael F. Becker

---

John W. Keto

---

Graeme Henkelman

---

Donglei Fan

**LAMA-Produced Metal-on-Oxide Nanoparticles and Films**

**by**

**Michael Drew Gammage, B.S. Phy.**

**Dissertation**

Presented to the Faculty of the Graduate School of

The University of Texas at Austin

in Partial Fulfillment

of the Requirements

for the Degree of

**Doctor of Philosophy**

**The University of Texas at Austin**

**May 2016**

## **Dedication**

*To my family and friends; without whom I never could have endured*

## **Acknowledgements**

I would like to thank the many people who have helped, guided, mentored, and motivated me during my time as a graduate student. Foremost is Dr. Desiderio Kovar, he saw potential in me, and through his unwavering support I have begun my journey of fulfillment. The predominant figure in my education as an experimentalist is Dr. John Keto. His abundance of knowledge was shared with me throughout all stages of my graduate research. Another outstanding mentor has been Dr. Michael Becker. His guidance, both experimentally and professionally, has been priceless. I would also like to thank Drs. Graeme Henkelman and Donglei Fan for their encouragement and service to my committee.

Several people have gone above and beyond for me and I would like to acknowledge them. Dr. Karalee Jarvis is an amazing microscopist and trainer. Her help with the TEM analysis of my samples was vital to the progress of my experiments. Dr. Hugo Celio contributed much time in training and helping me understand XPS. Dr. Xiaobin Xu was integral in teaching me the Raman spectroscopy equipment and some of the theoretical concepts that were involved with my experiment. Dr. Richard Piner was also a huge source of Raman spectroscopy knowledge and without his expertise, I would have been struggling for much longer.

I would especially like to thank Guillaume Noiseau and for his help and friendship, and Zach Levine for his hard work in making the measurements used in Chapter 5. Lastly, I would like to thank my many coworkers who have been amazing teammates such as: Sergio Cortes, Malcom Hamilton, Tushar Chitrakar, Manuj Nahar, Claire Davis, Jean-Gil Gutierrez, Alex Scheuermann, Etienne Coffy, Romain Fleury, Kris Gleason, Michael Asoro, Nathan Erickson, and Blake Perez.

# **LAMA-Produced Metal-on-Oxide Nanoparticles and Films**

Michael Drew Gammage, Ph.D.

The University of Texas at Austin, 2016

Supervisor: Desiderio Kovar

The capability for the Laser Ablation of Microparticle (LAMA) process for producing unique nanostructured particles and films are studied. The processing parameters are adjusted to create nanostructures that have potential for producing superior properties in two distinct technologically important areas – olefin gas separations and plasmonic films. Two extremes in film nanostructure are targeted; 1) Highly porous metallic films for olefin separation and 2) Dense films for plasmonic optical films. For olefin separations, weak chemisorption of ethylene has been shown to be an important characteristic in the use of metals for the separation of ethylene from ethane. Previously, density functional theory (DFT) has been used to predict the binding energies of various metals and alloys, with Ag having the lowest chemisorption energy amongst the metals and alloys studied. Here non-equilibrium Au/Cu alloys are produced using LAMA and investigated by a combination of DFT calculations and experimental measurements. It is inferred from experiments that the binding energy between a Au/Cu alloy and ethylene is lower than to either of the pure metals Au or Cu, and DFT calculations confirm this results from Au segregation to the particle surface. Implications of this work suggest that it may be possible to further tune the binding energy with ethylene by compositional and morphological control of films produced from Au-surface segregated alloys. LAMA-

produced metal-on-oxide nanoparticles (NP) are investigated to determine whether the thermal stability of LAMA-produced nanoparticles can be improved without impacting their chemical reactivity. Investigations before and after heating using the transmission electron microscope show that Ag-on-TiO<sub>2</sub> nanostructures exhibit excellent resistance to coarsening at elevated temperatures and that there is no change to the binding energy of the ethylene to Ag. For plasmonic film applications, SiO<sub>2</sub> and metal-in-SiO<sub>2</sub> films were produced using LAMA and studied. Although dense SiO<sub>2</sub> films were not produced, it was demonstrated that it was possible to measure the plasmonic absorption peaks of metal NPs embedded in SiO<sub>2</sub> films. This opens up a new possibility for the investigation of the plasmonic properties of non-equilibrium metal NPs.

## Table of Contents

Table of Contents .....	viii
List of Tables .....	xi
List of Figures .....	xii
<b>CHAPTER 1: INTRODUCTION AND MOTIVATION</b>	<b>1</b>
Nanocatalysts .....	1
Au-on-TiO <sub>2</sub> Activity .....	4
Nanostructured Optical Films .....	5
Facilitated Transport Membranes for Ethylene/Ethane Separation .....	6
NPs and Films Produced by Laser Ablation of Microparticle Aerosols .....	7
Alternative Methods of Production of Oxide Films with Embedded NPs .....	9
Objectives .....	10
<b>CHAPTER 2: EXPERIMENTAL EQUIPMENT AND PROCEDURES</b>	<b>12</b>
Nanoparticle Synthesis: The LAMA Process .....	12
Aerosol Feed .....	14
Fluidized Bed Feeder Improvements .....	17
Ablation .....	18
Single Ablation .....	19
Double Ablation .....	22
Overview and Issues; Design of first double ablation cell .....	24
Second Ablation Cell .....	25
Simultaneous Ablation .....	26
Two-Chamber Approach .....	27
Filtration .....	28
Deposition .....	29
LabVIEW Control of Stepper Motors .....	30
Diffusion Collection of Nanoparticles for TEM Examination .....	31

LAMA Process Parameters.....	33
Single Chamber Ablation.....	33
Two-Chamber Ablation .....	35
Nanoparticle and Film Characterization .....	37
Raman Spectroscopy.....	37
Surface Enhanced Raman Spectroscopy.....	38
Gas Cell Design for Ethylene .....	40
Experimental Procedures for SERS .....	41
Metal-on-Oxide particles .....	42
<i>In-Situ</i> Heating Experiments.....	42
<i>Ex Situ</i> Heating TEM Micrographs.....	45
SiO <sub>2</sub> and Metal-in-SiO <sub>2</sub> Dense Films .....	45
SiO <sub>2</sub> NP Films.....	46
Metal-in-SiO <sub>2</sub> .....	46
Post-deposition heating Treatment .....	47
<b>CHAPTER 3: BINDING ENERGIES OF ETHYLENE TO NANOPARTICULATE FILMS PRODUCED BY LAMA</b>	<b>48</b>
Raman Spectroscopy and SERS of Ethylene on Metals.....	48
Ag, Au, and Au-Cu Alloy Films .....	49
Results.....	51
Discussion.....	61
Ag-on-TiO <sub>2</sub> NP Films .....	61
Discussion.....	63
Conclusions.....	63
<b>CHAPTER 4: METAL-ON-TiO<sub>2</sub> POROUS FILMS</b>	<b>65</b>
Morphology of Ag-on-TiO <sub>2</sub> NPs and NP Films .....	65
Temperature Stability of Ag-on-TiO <sub>2</sub> NPs .....	68
Ex Situ Heating Experiments.....	68
Ag Nanoparticles .....	69

Ag-on-TiO <sub>2</sub> Nanoparticles .....	72
<i>In Situ</i> Heating TEM.....	76
Discussion.....	78
Conclusions.....	78
<b>CHAPTER 5: SiO<sub>2</sub> AND METAL-IN-SiO<sub>2</sub> GLASS FILMS</b>	<b>80</b>
SiO <sub>2</sub> Films.....	81
Metal-in-SiO <sub>2</sub> .....	85
Conclusions.....	89
<b>CHAPTER 6: CONCLUSIONS AND FUTURE WORK</b>	<b>90</b>
Future Work .....	92
Alloy NP-on-TiO <sub>2</sub> .....	92
Facilitated Transport Membranes for Ethane/Ethylene Separation .....	94
Non-Equilibrium Alloys on a Porous TiO <sub>2</sub> Matrix for Catalysis .....	95
Metal and Alloy NP-in-SiO <sub>2</sub> Dense Films.....	95
<b>APPENDIX A: STEPPER MOTOR LABVIEW CODE</b>	<b>97</b>
<b>APPENDIX B: RAMAN GAS CELL SCHEMATICS</b>	<b>110</b>
<b>REFERENCES</b>	<b>113</b>
<b>VITA</b>	<b>117</b>

## List of Tables

Table 2.1:	Gas flows used in LAMA process for single chamber ablation deposition using 0.25 and 1 mm deposition nozzles. ....	33
Table 2.2:	Gas flows used in LAMA process for two-chamber ablation deposition using 0.25 mm nozzle. ....	35
Table 5.1:	Average change in UV-Vis transmission upon heating for three LAMA-produced SiO <sub>2</sub> films for several wavelength ranges. ....	84

## List of Figures

Figure 1.1: Schematics of cross-sections of a) a porous TiO <sub>2</sub> film with embedded Ag NPs, b) a cross sectional schematic of highly dense SiO <sub>2</sub> film with embedded Ag NPs, and c) a facilitated transport polymer membrane with embedded Ag NPs. ....	1
Figure 1.2: TEM images of Au NPs exposed to an electron beam intensity of $2.8 \times 10^9 - 2.9 \times 10^8$ e/cm <sup>2</sup> •s, after (a) 0 s (b) 90 s, and (c) 180 s. Taken from [7]. ....	2
Figure 1.3: An STM image of Au bilayer clusters on TiO <sub>2</sub> {110}. Taken from [8]. ....	3
Figure 1.4: TEM images of Au NPs on TiO <sub>2</sub> NPs exposed to an electron beam intensity of $2.8 \times 10^9 - 2.9 \times 10^9$ e/cm <sup>2</sup> •s. Taken from [7]. ....	4
Figure 1.5: Catalytic activity for CO oxidation as a function of particle size on the TiO <sub>2</sub> (110), with CO:O <sub>2</sub> = 1:5 and a total pressure of 40 Torr, at 353 K [8]. ....	5
Figure 1.6: Manufacturing process schematic for a self-assembled three-dimensional bi-continuous nano-architecture [30]. ....	10
Figure 2.1: Schematic of the LAMA process showing (a) aerosol generation, (b) ablation cell, (c) virtual impactor, and (d) supersonic impaction deposition chamber. ....	13
Figure 2.2: Schematic of a fluidized bed feeder that was used for aerosolizing the feedstock powder used for ablation. Redrawn from [22]. ....	14

Figure 2.3: Fluidized bed feeder flow diagram showing how the bypass flow affects the flow through the feeder. The flow rate through the feeder is directly proportional to the aerosol density generated. ....16

Figure 2.4: Schematic of two new glass bulb designs for the fluidized bed feeder. a) Design that moves the nozzle into the glass tube so that very small amounts of feedstock powder can be used. b) Design that allows a nanoparticle aerosol to be fed into the bulb where it can mix with the microparticle aerosol.....18

Figure 2.5: Ablation mechanisms for a) metal microparticle and b) transparent, spherical oxides. Redrawn from [22]......19

Figure 2.6: Schematic of the ablation chamber showing the center and outer flows, the ablation zone, and the skimmer and exhaust flows. Also shown, is the virtual impactor which will be discussed later. Taken from [22].21

Figure 2.7: Double ablation schematic showing how the gas flows through the first aerosol feeder on the top left, through the first ablation cell into a second feeder, and into the second ablation cell. This method was used to create islanded nanoparticles and core-shell nanoparticles. Taken from [7].23

Figure 2.8: TEM bright-field image of LAMA-produced metal-on-oxide NP consisting of Au-on-TiO<sub>2</sub>. Taken from [31]. ....23

Figure 2.9: Diagram showing the desired flow of aerosol during double ablation in green, and the actual flow of aerosol in red. ....25

Figure 2.10: Schematic of the second double chamber ablation cell. ....26

- Figure 2.11: Diagram showing the two-chamber method used to make islanded nanoparticles. The excimer laser was split using a mirror. Each beam was then focused into two separate ablation cells. The nanoparticle aerosol from the first ablation was then mixed with the microparticle aerosol of the second feeder, using the bulb design shown in Fig. 2.4b. This aerosol mixture was routed into the second ablation cell. ....28
- Figure 2.12: Schematic of the virtual impactor used to filter out unablated microparticles from the NP aerosol. This aerosol is then fed into the deposition chamber. Taken from [24].....29
- Figure 2.13: Schematic of the supersonic deposition chamber used to deposit patterned films of NPs generated by LAMA. The NP flow from the virtual impactor is passed through a nozzle into a vacuum chamber. The gas is accelerated by a pressure differential and this in turn accelerates the nanoparticles. These nanoparticles are impacted onto a substrate that is translated using an x-y stage and programmed to pattern films. Taken from [33].....30
- Figure 2.14: Schematic of the chamber used to collect TEM grid samples. The flow from the virtual impactor passes through this chamber filled with glass wool (shown in blue). TEM grids are placed on the glass wool so that the NPs diffuse onto the surface of the grids. ....32
- Figure 2.15: SEM micrographs of glass wool used to support TEM grid for diffusion collection. Magnifications were a) 70×, b) 160×, and c) 850×.....33

Figure 2.16: Flow diagram of the single chamber LAMA process. Gas was flowed through an aerosol feeder then through an ablation cell. An outer flow was also flowed to create laminar gas flow through the cell. Taken from [34].....34

Figure 2.17: Flow diagram of the two-chamber LAMA process. ....36

Figure 2.18 Simplified Jablonski diagrams illustrating schematically the Rayleigh (a) and Raman (b) scattering processes. An alternative way of visualizing these scattering processes from a quantum mechanical point of view is shown in (c) and (d). Taken from [36].....38

Figure 2.19 Electromagnetic enhancements responsible for increased signal in SERS, taken from [35].....39

Figure 2.20 Schematic of pressure cell for gas on NP Raman measurements. ....40

Figure 2.21: (a) Tip of Protochips® specimen holder showing heater chip clamped into place, with electrical leads connected. (b) Top view schematic of Protochips heater chip. The insets are low magnification TEM images of the central region of the chip showing the pattern of holes in the low-conductivity ceramic membrane and holey carbon support film overlaying the holes in the ceramic membrane. (c) Cross-section view of chip (courtesy of Protochips Inc.).....44

- Figure 3.1: Raman spectrum for ethylene on a SERS Au<sub>0.35</sub>/Cu<sub>0.65</sub> alloy (blue) film. The C=C peak of ethylene is shifted from the unbound position of 1623 cm<sup>-1</sup> [24] to ~1590 cm<sup>-1</sup>. The spectra for ethylene on SERS Ag (red) and Au (green) NP film are also shown for reference. Calculated frequency shifts of the C=C stretching mode of ethylene bound to Ag (red vertical line), Au (green vertical line), Cu (orange vertical line, and Cu@Au (core@shell, blue dashed line) nanoparticles are shown. ....52
- Figure 3.2: Raman spectra measured at two laser intensities for ethylene on commercially obtained Ag SERS substrates near the frequency of the C=C stretch. The peak breadth increases with laser power. The spectral intensities were scaled for ease of viewing.....54
- Figure 3.3: XPS spectra of Au/Cu NP film before sputtering (red) and after (black). The Cu 2p peaks are present after sputtering but not before indicating that Au has segregated to the surface of the film.....57
- Figure 3.4: Calculated binding energy versus C=C stretch frequency for 79 atom Ag, Au, Cu, Au<sub>0.35</sub>Cu<sub>0.65</sub> and Cu@Au (coreshell) NPs on different binding sites. Random Au<sub>0.35</sub>/Cu<sub>0.65</sub> alloys (labeled Au/Cu) are shown with the standard deviation taken from 30 calculations, and single calculations were carried out for all other NPs, since there is only one composition possible with these models. Data are presented by the adsorbing metal, Ag (red), Au (green) and Cu (orange) and are given as Ag-face (model composition-binding site). Experimental frequencies are indicated on the y-axis, Ag (red), Au/Cu (blue), Au (green). Inset: Image of the Cu@Au<sub>79</sub>-atom NP with adsorbed ethylene on a {111} facet site—Cu atoms (blue), Au (yellow), C (brown). ....59

- Figure 3.5: Binding energy versus C=C stretch frequency of ethylene on Au<sub>0.35</sub>/Cu<sub>0.65</sub> random alloy slab with a surface layer of gold (denoted as AuCu@Au). The calculated value for Ag, Au, and Cu slabs are given for reference, as well as the experimental values on the y-axis, Ag (red), Au/Cu (blue), Au (green). Inset: Image of AuCu@Au with an adsorbed ethylene molecule—Cu atoms (blue), Au (yellow), C (brown).....60
- Figure 3.6: Raman spectra measured for ethylene on LAMA-produced Ag and Ag-on-TiO<sub>2</sub> NP films near the frequency of the C=C stretch. The spectral intensities were scaled for ease of viewing.....62
- Figure 4.1: Agglomerated chains of amorphous TiO<sub>2</sub> decorated with Ag NPs. This Ag-on-TiO<sub>2</sub> NP chain is shown in: a) bright field TEM, b) high angle annular dark field (HAADF) STEM, c) a higher magnification bright field TEM, and d) a higher magnification HAADF STEM image showing a high density of small isolated Ag NPs on the surface of amorphous TiO<sub>2</sub>. .....67
- Figure 4.2: Ag NPs produced by a single-chamber LAMA process and collected using diffusion on to Au TEM grids with no carbonaceous support. The particles are polycrystalline and around 10 nm in diameter with some amorphous carbon contamination on the surface.....70
- Figure 4.3: Ag NPs produced by the single-chamber LAMA process and collected using diffusion on to Au TEM grids with no carbonaceous support. The grid was then heated to 500° C in flowing Ar for 1 hour and then allowed to cool. The particles have sintered into larger polycrystalline particles. ....71

Figure 4.4: Ag NPs produced by a single-chamber LAMA process and collected using diffusion on to Au TEM grids with no carbonaceous support. The grid was then heated to 500° C in open air for 1 hour. The particles have sintered into larger polycrystalline particles. ....72

Figure 4.5: Representative images of as –deposited Ag-on-TiO<sub>2</sub> NPs produced by the two-chamber LAMA process and collected using diffusion on to Au TEM grids with no carbonaceous support. The darker regions with lattice fringe corresponds to Ag NPs, as confirmed by analyzing the lattice parameters. ....73

Figure 4.6: Ag-on-TiO<sub>2</sub> NPs produced by the two-chamber LAMA process and collected using diffusion on to Au TEM grids with no carbonaceous support. The grid was then heated to 500° C in flowing Ar for 1 hour and then allowed to cool. ....74

Figure 4.7: Ag-on-TiO<sub>2</sub> NPs produced by the two-chamber LAMA process and collected using diffusion on to Au TEM grids with no carbonaceous support. The grid was then heated to 500° C in open air for 1 hour. Shown in a) is an anatase crystal with a small region of amorphous TiO<sub>2</sub> attached to a 10 nm Ag NP, b) a higher magnification of the Ag NP, c) a 100 nm agglomerate of crystalline TiO<sub>2</sub>, and d) a lower magnification of a crystallite showing lattice fringe spacing that corresponds to the rutile structure of TiO<sub>2</sub>. ....75

Figure 4.8: Ag-on-TiO<sub>2</sub> NPs produced by the two-chamber LAMA process and collected using diffusion on to Arduro Protochips® grids. Ag-on-TiO<sub>2</sub> NPs were then heated *in situ* in a TEM in 50° C increments and held to take micrographs at each step. The highest temperature with no change is shown in the top left at 475° C, then noticeable changes to the Ag NPs are shown at the corresponding temperatures.....77

Figure 5.1: UV-Vis transmission spectra of three LAMA SiO<sub>2</sub> NP films and the glass microscope slide used as a substrate.....82

Figure 5.2: Graph of the change in UV-Vis transmission spectra upon heating for three LAMA-produced SiO<sub>2</sub> NP films.....84

Figure 5.3: Transmission spectra of Ag-in-SiO<sub>2</sub> NP film before and after heating to 400° C for 1 hour.....86

Figure 5.4: Transmission spectra of Au-in-SiO<sub>2</sub> NP film before and after heating to 400° C for 1 hour.....87

Figure 5.5: Transmission spectra of Cu-in-SiO<sub>2</sub> NP film before and after heating to 400° C for 1 hour.....88

Figure 6.1: Schematic of a proposed LAMA configuration to minimize the distance between the two cells used for producing metal-on-oxide NPs.....94

## CHAPTER 1: INTRODUCTION AND MOTIVATION

Shown in Fig. 1.1a-c are three nanostructures that are of interest for applications in a number of important technological areas including fuel cells [1], water desalination [2], petrochemical processes [3], and solar cells [4]. In Fig 1.1a, a nanostructure consisting of a *porous* oxide with embedded, dispersed metallic nanoparticles (NPs) is shown. A schematic of a *dense*, transparent oxide with a small volume fraction of embedded metallic nanoparticles (NPs) is shown in Fig. 1b. A schematic of a facilitated transport polymer matrix consisting of metal NPs embedded in a polymer membrane is shown in Fig. 1.1c.

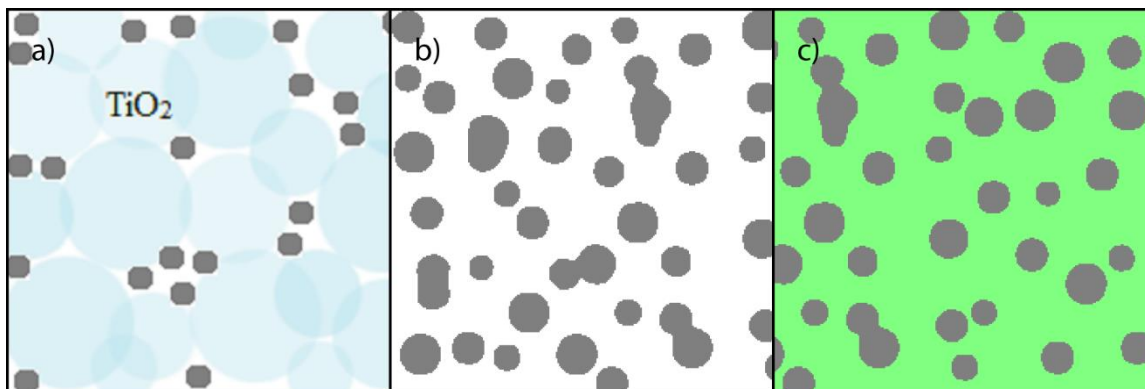


Figure 1.1: Schematics of cross-sections of a) a porous  $\text{TiO}_2$  film with embedded Ag NPs, b) a cross sectional schematic of highly dense  $\text{SiO}_2$  film with embedded Ag NPs, and c) a facilitated transport polymer membrane with embedded Ag NPs.

### NANOCATALYSTS

One application for a nanostructure consisting of a porous oxide scaffold with metallic nanoparticles on the surface of the oxide particles (Fig. 1a) is catalysis. The ideal nanostructure for this application consists of a highly porous, well-connected oxide

scaffold with a high density of small, 2 - 10 nm metal NPs on the surfaces of the oxide particles.

To understand why the structure shown in Fig. 1a would be ideal for this application, it is necessary to consider the current state-of-the art for catalysts. Fine particles increase reactivity because the high specific surface area that is characteristic of fine particles increases the number of reaction sites and therefore increases catalytic conversion efficiency. The nanostructure must be porous to allow gasses to pass through the nanostructure. In addition, metal NPs can have higher reactivity than the bulk, which further improves their performance relative to coarser particles or bulk materials [5].

Catalyst reactions often occur at moderate-to-high temperature, which can lead to challenges for maintaining an optimal NP size because particle coarsening typically lowers catalyst activity and lifetime [6]. An example of coarsening of nanoparticles that are not supported on an oxide is shown in Figure 1.2. The electron beam in a transmission electron microscope (TEM) was used to heat Au by applying a known electron flux to the particles that were placed on a carbon film [7]. The heating from the electron beam caused the Au NPs to neck and then sinter into a larger particle.

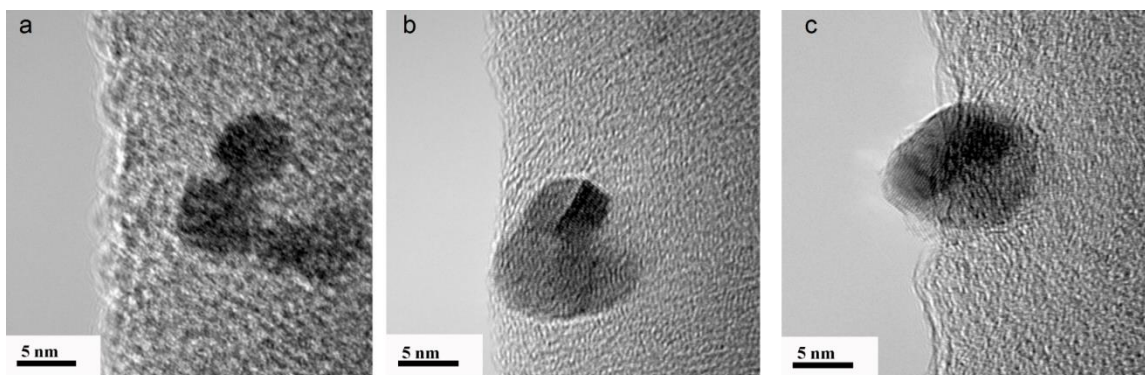


Figure 1.2: TEM images of Au NPs exposed to an electron beam intensity of  $2.8 \times 10^9 - 2.9 \times 10^8 \text{ e/cm}^2 \cdot \text{s}$ , after (a) 0 s (b) 90 s, and (c) 180 s. Taken from [7].

Previous studies have shown metal nanodisks that are supported on oxide substrates, as shown in Fig. 1.3, resist coarsening to higher temperatures than unsupported metals. This phenomenon has been attributed to pinning of the nanodisks to defect sites on the surface of a reduced oxide [8].

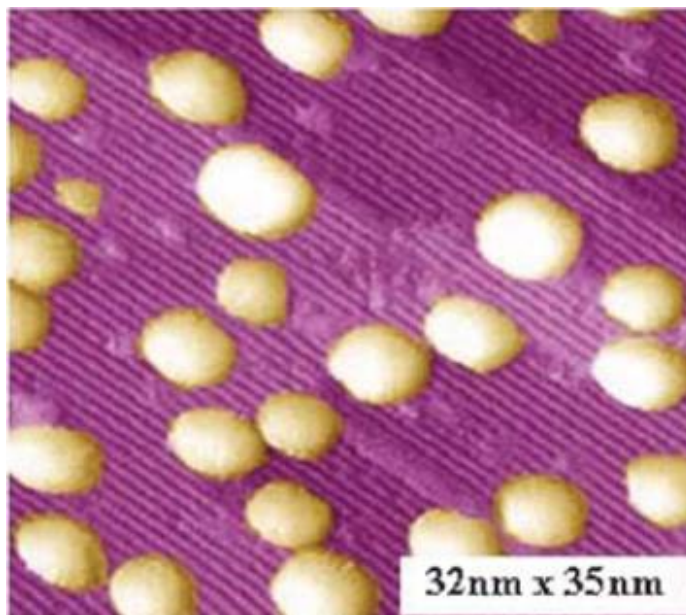


Figure 1.3: An STM image of Au bilayer clusters on  $\text{TiO}_2$  {110}. Taken from [8].

A variation of this principle that has greater practical significance has been demonstrated where metal nanoparticles were placed on the surfaces of larger oxide particles to produce three-dimensional NP-on-oxides nanostructures [7]. In this case the Au NPs were deposited onto  $\text{TiO}_2$  and the electron beam heating experiments were repeated. As shown in Fig. 1.4, Many of the Au particles were stationary and resisted migration and sintering. This suggests that metal-on-oxide NPs may be more sinter-resistant than free metal NPs. However, this experiment was limited to locally heating in a vacuum using only the electron beam to provide the heat, so the actual temperature

during the experiment was not known. Nevertheless, these results suggest that this nanostructure could provide enhanced resistance to coarsening relative to bare nanoparticles.

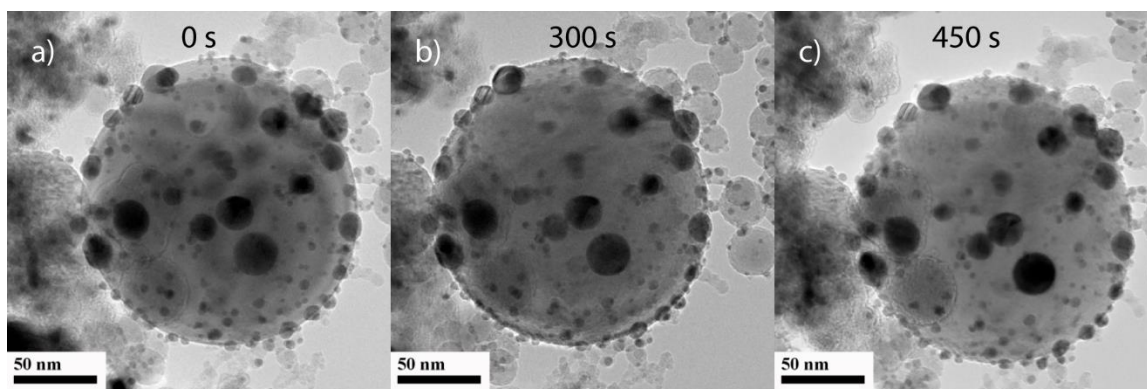


Figure 1.4: TEM images of Au NPs on TiO<sub>2</sub> NPs exposed to an electron beam intensity of  $2.8 \times 10^9 - 2.9 \times 10^9$  e/cm<sup>2</sup>·s. Taken from [7].

#### AU-ON-TiO<sub>2</sub> ACTIVITY

Au nanodisks that are bound to vacancy sites not only exhibit enhanced resistance to coarsening, but also increased activity. A peak in the activity has been observed when the Au nanodisks were around 3 nm, as shown in Fig. 1.5. Oxygen vacancies that result from reducing an oxide such as TiO<sub>2</sub> have been shown to interact with nearby metal to further increase catalytic activity [9]. It has also been shown that Au nanodisks chemisorb to these vacancies. This was confirmed by measuring the activity of Au nanodisks on reduced TiO<sub>2</sub> before and then after removal of the vacancies by heating in oxygen [10].

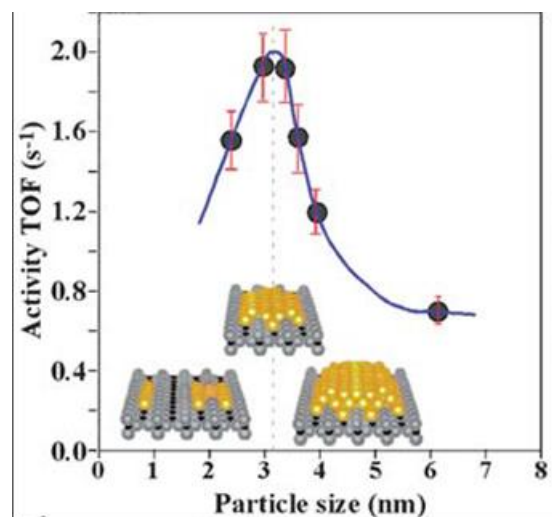


Figure 1.5: Catalytic activity for CO oxidation as a function of particle size on the TiO<sub>2</sub> (110), with CO:O<sub>2</sub> = 1:5 and a total pressure of 40 Torr, at 353 K [8].

### NANOSTRUCTURED OPTICAL FILMS

Applications for nanostructured optical films include solar cells, bio-sensing, non-linear optics, and lasing media [11]. The ideal structure for these applications consists of a fully dense, optically transparent oxide, with a small volume fraction of well-dispersed metallic inclusions in the 15 - 20 nm size range. For these applications, metal nanoparticles that result in plasmonic effects are beneficial and are a topic of much recent interest [11]. Three-dimensional plasmonic films such as these are an alternative to interference filters, but without the unwanted angular dependence that those films exhibit. Furthermore, the particle size and composition can tune the optical properties of the films. However, there has been little work in this area, probably because with existing manufacturing methods, it is difficult to produce films with controlled particle size and composition in the ranges that are of interest.

## **FACILITATED TRANSPORT MEMBRANES FOR ETHYLENE/ETHANE SEPARATION**

The massive global production of ethylene and its widespread use in polymer materials warrants investigation of potential efficiency improvements [11]. Fractional distillation is currently widely used for separating ethylene from a cracked gas mixture. This process occurs under high pressure and low temperature, thus making it expensive and energy intensive [12-14]. An alternative to separation by distillation is the use of a transport membrane that is engineered to have higher selectivity and/or permeability for one molecule over another in order to produce a higher transport of that molecule across the membrane. Selective, permeable membranes could be used to separate ethylene from the cracked gas mixture at a far reduced energy cost [12,13]. Polymer membrane designs have been proposed that utilize Ag(I) and Cu(I) complexation with olefins to enhance selectivity for gas mixtures. However, the metal ion-olefin complexes are unstable in air, which limits their use in industrial settings [2].

Another method that has been shown to be effective at increasing selectivity is through the use of a facilitated transport membrane that contains embedded particles [15]. The presence of the particles in the membrane can selectively increase the solubility of the membrane for a gas, increase permeability of that gas, or both increase the solubility and permeability. Since the selectivity is a product of the permeability and solubility, the selectivity will be enhanced with any of these changes.

An ideal facilitated transport membrane should contain a high volume fraction of fine, dispersed nanoparticles. Such NPs provide a high surface area and therefore a large number of binding sites to increase the solubility of the gas in the membrane. A high binding energy between the gas and the metal NP is desirable to increase solubility, but has the detrimental effect of decreasing permeability because the gas is then bound too strongly to the NP to move through the membrane. Thus, in practice, there is an optimum binding

energy that balances the solubility and permeability. Previous Monte Carlo simulations have suggested that the optimum binding energy for ethylene is very low and Ag has the lowest known binding energy with ethylene for a pure metal [16]. This suggests that Ag NPs could be used to increase the selectivity of a polymer membranes [17]. However even Ag's binding energy is above the optimum [17]. Alloys may provide a method to tune the binding energy to even lower values, and thus be an alternative to Ag for ethylene separation. However, for several alloys that were previously investigated [18,19], the binding energies with ethylene were between the pure, end members of the alloys, and therefore were not suitable.

Another challenge for producing facilitated transport membranes is that separations typically occur at elevated temperature where coarsening of the particles can occur. Placing the metal nanoparticles onto a large oxide particle which is then embedded in a polymer membrane could offer enhanced coarsening resistance. Embedding alloy NPs with a precisely tuned binding energy to ethylene into the polymer membranes would offer improved stability and selectivity of ethylene [16,17,20].

### **NPs and Films Produced by Laser Ablation of Microparticle Aerosols**

The Laser Ablation of Microparticle Aerosol (LAMA) process is a method for producing nanoparticles and depositing these particles at high velocities to make nanostructured films. In conventional LAMA, 2 - 40 nm particles are produced and then deposited to produce solid films that can range in thickness from nanometers to tens of microns [21]. In addition to metal NPs, alloy nanoparticles have also been produced using LAMA by ablation of alloy NPs or simultaneous ablation of two pure metals. Metallic NPs produced by LAMA have also been deposited into photo-polymerizable monomer liquids and the NP/monomer liquids were subsequently polymerized to produce

polymer films with embedded NP [22]. This method can be used to produce facilitated transport membranes.

Through a modification to the standard LAMA process known as double ablation, it has been shown that it is possible to create nanostructures that consist of small 2 - 5 nm metal particles dispersed on the surface of larger 20 - 30 nm oxide particles [19,23]. Figure 1.2 shows an example of a metal-on-oxide particle consisting of dispersed Ag NPs on a TiO<sub>2</sub> NP. Molecular dynamics (MD) simulations predict that by adjusting the NP impaction energy following ablation, one can tune the as-deposited density of films produced by LAMA [21,24] and recent experiments have corroborated this prediction [25]. This suggests that if the impaction energy is high enough, one could produce nearly dense, optically transparent, plasmonic films, and if the energy is low enough, one could also create low density, porous nanocatalyst films.

The LAMA process offers several potential advantages compared to existing methods for producing nanostructured films. For example, LAMA has the potential for producing active metal surfaces with extremely high surface areas, and without the need for added capping layers of organics that can interfere with device functionality. In addition, previous preliminary experiments with LAMA-produced nanostructures indicated that the NPs in such a system are resistant to coarsening, which suggests that these nanostructures could be stable, even at temperatures above ambient [7]. Other useful advantages of the LAMA process are that the feedstock materials (metals, oxides, and semiconductors) can be interchanged without changing the configuration of the equipment used for the process and the sizes of the NPs can be controlled from 2 nm to 40 nm by varying the gas type and gas pressure used in aerosol [26]. The LAMA process has the potential for high rates of NP production with laboratory-scale setup [24] and direct writing through supersonic impaction allows user control over the film density and

the geometry of the films [27]. Unique to the LAMA process, is the ability to produce equilibrium and highly non-equilibrium alloy NPs [23], which are useful for tuning both catalytic and plasmonic effects.

### **Alternative Methods of Production of Oxide Films with Embedded NPs**

There are numerous alternative methods to produce NPs and NP films and it is instructive to compare and contrast those processes with LAMA since each method has advantages and disadvantages. Conventional methods for producing these NPs and nanoparticulate films typically involve wet-chemical synthesis that results in an organic capping layer on the surface of the particles that is used to stabilize the particle suspensions when they are in liquids to prevent agglomeration [28]. Because the organic can interfere with the functionality of the devices from which they are made, the organic is usually removed through pyrolysis by heating. However, care must be taken to avoid coarsening of the metal particles during this heat treatment because the loss of specific surface area and the increase in particle diameter that occur when coarsening degrades properties [29]. Chemical growth techniques can produce metal NPs on oxide substrates, but the metal choices are limited to available synthesis routes and alloy compositions are limited to alloys on the first few atomic layers of the surface of a nanostructure, referred to as surface alloys [18].

Vapor deposition techniques can be useful in certain situations, but the geometries of the deposits are limited. One example of a vapor-phase deposition technique is metal nanodisks-on-flat oxides [8]. The nanodisks produced using this method have the disadvantages of having a low surface-to-volume ratio due to the flat support structure and low aspect ratio and the process requires ultra-high vacuum. Thus, although they are useful for academic studies, this method for producing metal-on-oxide particles is not

practical for technological applications. Furthermore, alloys for this process are also limited to surface alloys, just like chemical routes.

One novel approach to producing three-dimensional nano-architectures is the colloidal assembly of oxide structures [30]. This process can be followed by a chemical growth of metal nanoparticles or films, Fig. 1.6. This nanostructure is ideal for applications that require high surface-to-volume ratio, since the scaffolding provides a highly porous substrate, but there is a limited ability for this process to scale beyond laboratory test samples. Another practical problem with this process is fracturing of the relatively weak support scaffolding during thermal cycling.

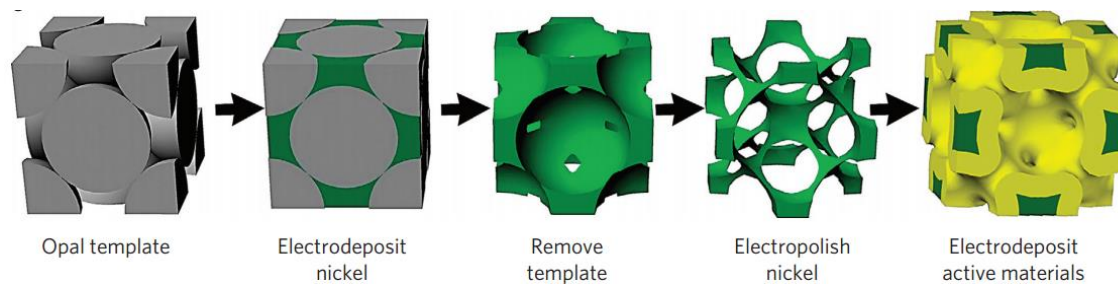


Figure 1.6: Manufacturing process schematic for a self-assembled three-dimensional bi-continuous nano-architecture [30].

## Objectives

The focus of this dissertation is the use of LAMA to produce nanoparticulate films with a range of nanostructures. To accomplish this goal, it is necessary to develop an understanding of the processing parameters that control the nanostructures and composition of films that are produced using the LAMA process. This understanding is then used to study the effects of nanostructure on the chemical properties, coarsening resistance, and optical properties of LAMA-produced films.

To accomplish these goals, films will be produced and studied with each of the three nanostructures shown in Fig. 1.1. The experimental procedures used in this dissertation are discussed in Chapter 2. In Chapter 3, the use of LAMA to produce metallic and metallic alloy nanoparticles is presented. As a first step towards developing facilitated transport membranes with embedded NPs, the binding energies for ethylene to metallic and metallic alloy NPs are determined using surface-enhanced Raman spectroscopy. The unique characteristics of LAMA are used to produce non-equilibrium alloys and computational tools are used to understand the experimental results that are obtained. In Chapter 4, the stability of metal-on-oxide NPs is studied through a combination of *in situ* and *ex situ* experiments. In Chapter 5, the use of LAMA to produce optical films is explored. First SiO<sub>2</sub> films are produced via LAMA and then subjected to a post-deposition sintering treatment to determine the feasibility of producing films with sufficient density so that optical performance can be assessed. Subsequently, SiO<sub>2</sub> films with metallic NPs embedded in them are produced to demonstrate the feasibility of this approach.

## **CHAPTER 2: EXPERIMENTAL EQUIPMENT AND PROCEDURES**

In this section, the LAMA process is explained, and the improvements that were made to the LAMA system for this dissertation are discussed in more detail. The different characterization techniques and equipment that were used for experiments are presented. Lastly, detailed procedures that were used for each experiment are provided.

### **Nanoparticle Synthesis: The LAMA Process**

The LAMA technique for producing NP aerosols has important advantages compared to more conventional chemical processes that are used to synthesize NPs, although there are disadvantages to consider as well. With LAMA, NPs from 2 – 40 nm can be produced from metals, semiconductors, or dielectrics [24]. In addition, LAMA is capable of producing NPs and nanostructures that may be difficult to produce using traditional NP synthesis routes, including non-equilibrium compositions, core-shell NPs metal-on-oxide islanded particles, and thick nanoparticulate films [7]. LAMA provides the unique ability to change the constituents of the multicomponent NPs with relative ease, as opposed to chemical processes where the design of a new synthesis route is generally required for each material system.

An overview of the LAMA process is presented in Fig. 2.1, microparticle aerosol generation is the first step in LAMA [7, 21, 22, 23, 24]. A powder of microparticles (1-20  $\mu\text{m}$  in diameter) may be obtained commercially or produced in the laboratory. The particles are aerosolized out of the feeder using an inert gas. The flow rate out of the aerosol generator is set so that the residence time for microparticles in the ablation region is equal to at least one pulse repetition interval of the laser [22]. The high-powered laser pulse is focused onto the microparticle aerosol, resulting in a shockwave that leads to a plasma breakdown of the particle; this occurs in the ablation cell shown in Fig. 2.1b. Once

the shockwave travels through the microparticle, rapid condensation occurs in the wake of the shock where the pressure is low, causing the formation of NPs. The expansion and therefore the NP size can be controlled by the type of gas used in the aerosol. Higher molecular weight gasses result in less expansion and the resulting NPs are larger. For NPs in the 2-10 nm range, helium is used whereas for NPs in the 20-50 nm range, argon is used. For the studies presented here, the pressure in the ablation cell is near ambient.

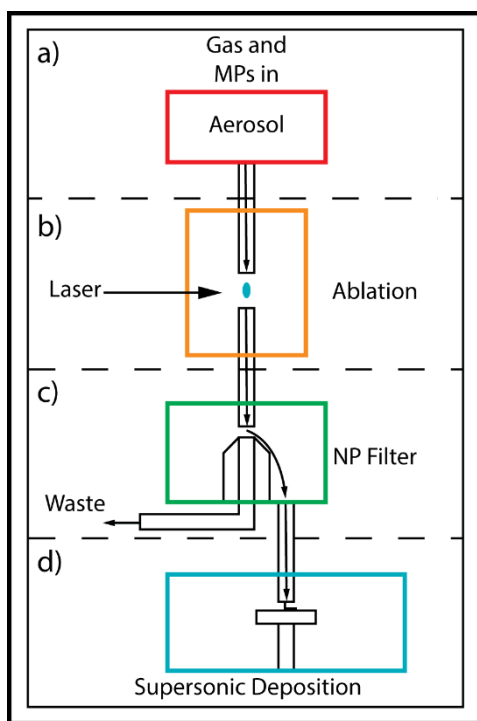


Figure 2.1: Schematic of the LAMA process showing (a) aerosol generation, (b) ablation cell, (c) virtual impactor, and (d) supersonic impaction deposition chamber.

As seen in Fig. 2.1, the LAMA process can be broken up into four major steps: aerosol feed, ablation, filtration, and deposition. In the next sections these steps are considered in more detail.

## AEROSOL FEED

The aerosol feeder used for the current work is a modified fluidized bed feeder that provides a user-adjustable feed rate. A mechanically coupled eccentric motor vibrates the body of the feeder creating a fluidized bed of powder at the bottom of the tube. The body of the feeder has a small orifice through which the gas is introduced and which creates a gas jet that aerosolizes the powder. Above the orifice the glass tube expands into a bulb that slows the gas and allows the larger agglomerates in the powder to settle back down since they have quicker settling times in the gas than the smaller particles. The remaining particles entrained in the gas flow out of the feeder and into the ablation chamber.

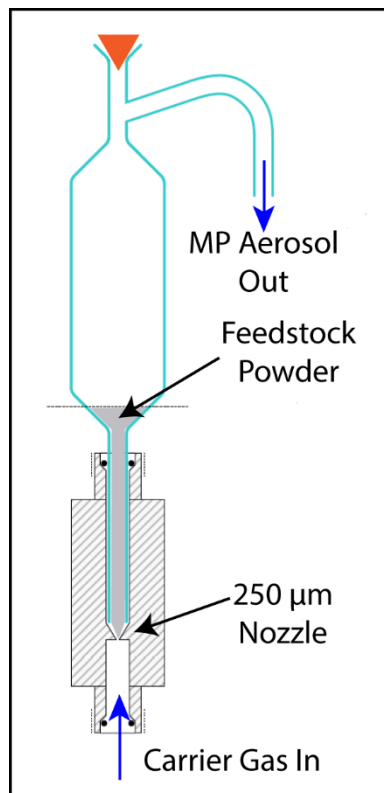


Figure 2.2: Schematic of a fluidized bed feeder that was used for aerosolizing the feedstock powder used for ablation. Redrawn from [22].

An overview of the gas handling used to control the aerosol feeder is presented in Fig. 2.3. The carrier gas is controlled using a mass flow controller through a 3-way split connector with a variable valve on the outlet that connects to the feeder. The other outlet is bypassed to another 3-way split connector on the aerosol outlet of the feeder. By varying the valve position, the amount of gas flow through the feeder can be controlled and this results in a change in the aerosol density of the feeder output. Details of the flow rates for all of the experiments are presented later in this chapter.

The fluidized bed feeder shown in Fig. 2.3 was successfully used to create microparticle aerosols for use with the LAMA, but some problems arose during the course of this research. Approximately one gram of material was the minimum needed to fill the glass tube to the top of the bulb and allow the feeder to operate; this is an excessive amount of material when using more precious materials. Another issue was that this design did not allow for sequential ablations of two materials, which was one of the original goals of this research. Sequential ablation was pioneered by previous students using a feeder that allowed a nanoparticle aerosol to feed into a secondary microparticle feeder and create a mixed aerosol. If a nanoparticle aerosol were to be fed into this feeder, the nanoparticles would agglomerate with the microparticles and this would not be a controllable process.

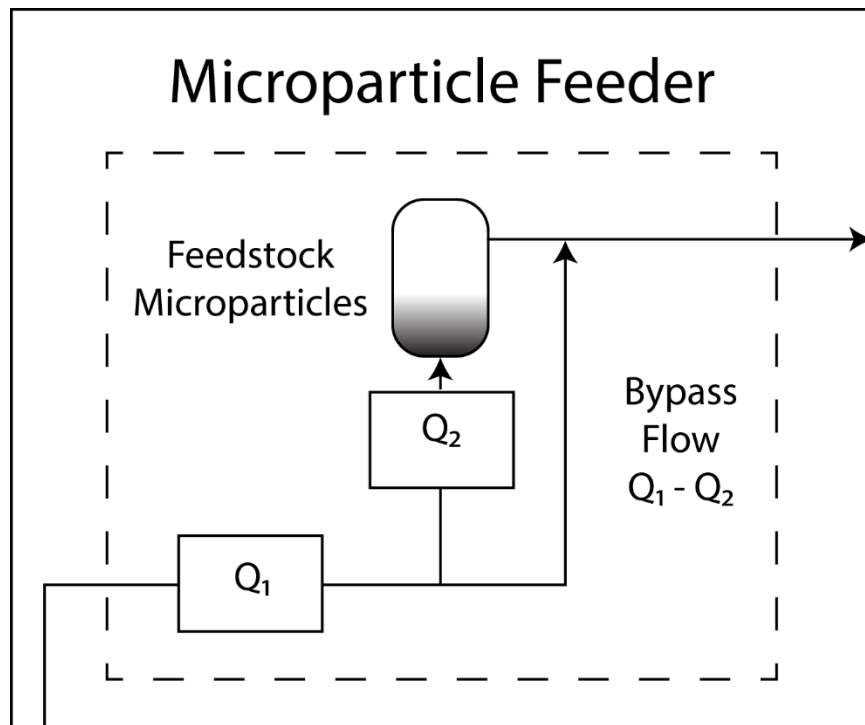


Figure 2.3: Fluidized bed feeder flow diagram showing how the bypass flow affects the flow through the feeder. The flow rate through the feeder is directly proportional to the aerosol density generated.

## **Fluidized Bed Feeder Improvements**

A number of improvements were made to the previously used feeder for this research. The nozzle consists of a small capillary tube located at the bottom of the tube where the gas enters. Glass wool was added below the nozzle to prevent the microparticle powders from falling into the lower portions of the mount. A new angled nozzle with an approximate diameter of 2 mm was added to the design to enhance mixing of microparticles with nanoparticles of a different material that enters the bulb from a separate ablation chamber, as shown in Fig. 2.4b. This two-chambered process allows it to be used to make metal-on-metal-oxide islanded nanoparticles. This tube can also be used as a bypass for single ablation to help lift out aerosolized powder from the bottom of the feeder for materials that are otherwise difficult to feed.

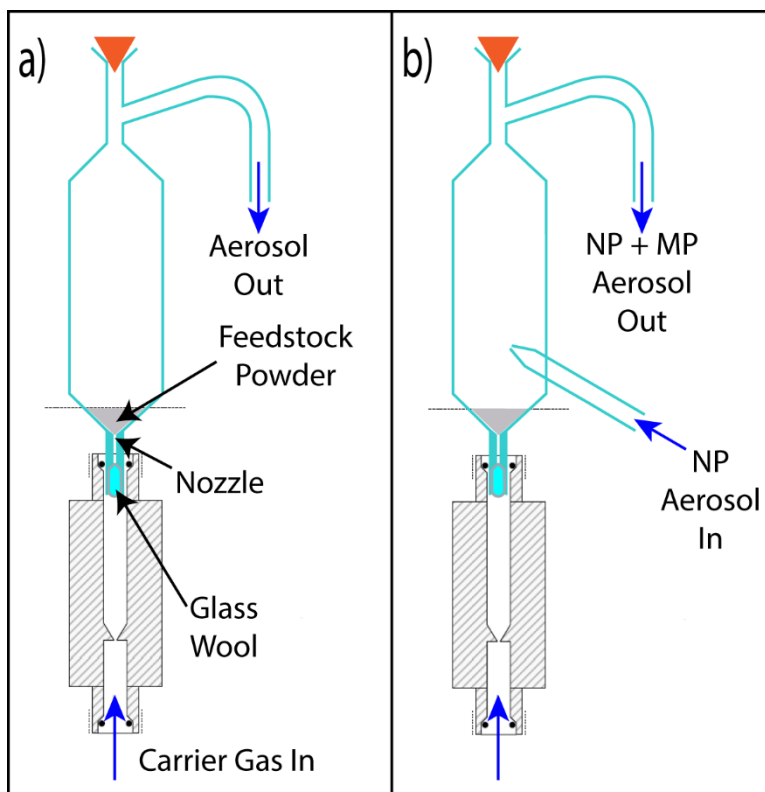


Figure 2.4: Schematic of two new glass bulb designs for the fluidized bed feeder. a) Design that moves the nozzle into the glass tube so that very small amounts of feedstock powder can be used. b) Design that allows a nanoparticle aerosol to be fed into the bulb where it can mix with the microparticle aerosol.

## ABLATION

Presented in this section is an overview of the ablation techniques used to produce NPs and NP films. First, a discussion of single ablation is presented, followed by a more detailed explanation of double ablation and several of the modifications of this technique. These modifications which use two ablation cells in series are collectively referred to as the redesigned double ablation chambers. Lastly simultaneous ablation of two components is presented.

## Single Ablation

Once the feedstock microparticles are aerosolized, the next step is to ablate them and create a NP aerosol. Previous work from our group has shown that the ablation and consequent NP formation is dependent on the type of material being ablated, as shown in Fig. 2.5 [22]. If the feedstock microparticle feedstock is metallic, then a laser with a 248 nm wavelength is absorbed into the skin depth of the material and the large, local energy density results in a shockwave that is formed near the surface of the microparticles. The propagation of this shockwave ablates the particles into a plasma and in the rarefaction behind the shockwave rapid condensation of nanoparticles occur.

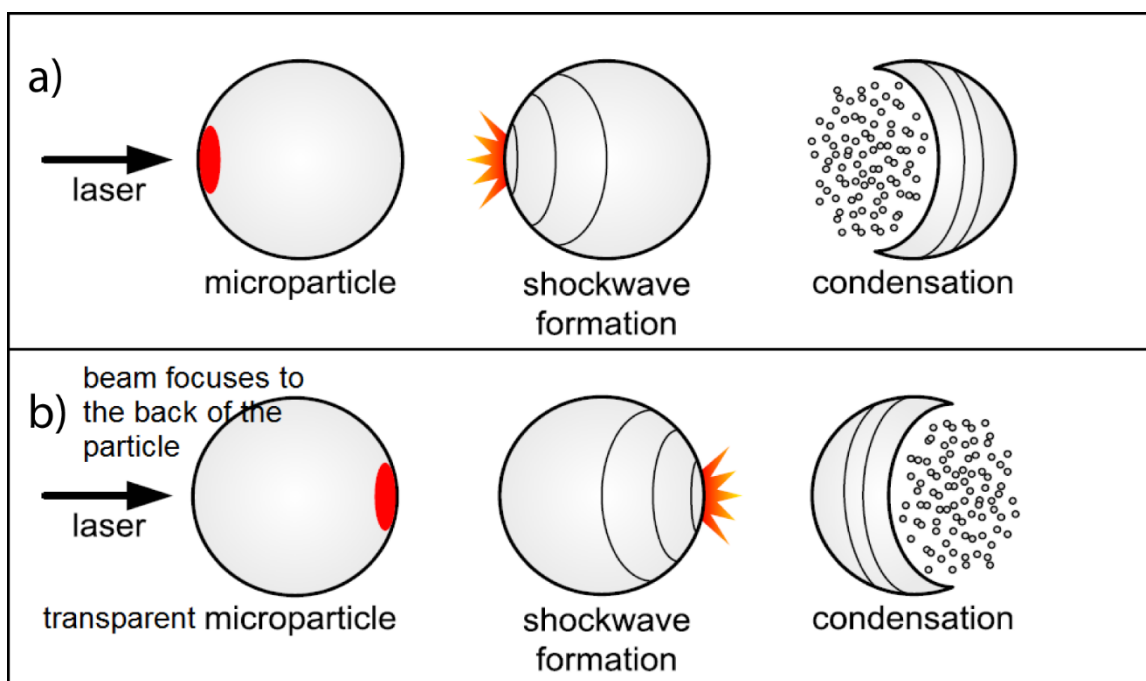


Figure 2.5: Ablation mechanisms for a) metal microparticle and b) transparent, spherical oxides. Redrawn from [22].

In the case of transparent, spherical dielectrics such as the oxides used in this study, the oxide is transparent to the laser. However, because the particle is spherical and acts like a lens, the laser is focused near the back surface of the particle, resulting in a locally high energy density. A shockwave initiates in this region of the particle and travels from the back of the particle towards the front. Rarefaction and rapid condensation occur behind the shockwave for dielectrics and metals once the shockwave is launched, but the shockwaves propagate in opposite directions. The ablation chamber design is shown schematically in Fig. 2.6. The inner diameter of the ablation cell chamber is 13 mm, the tip of the feed nozzle is bent into an ellipse with axes 1 mm  $\times$  5 mm, and the skimmer is a tube bent into an ellipse with axes 3 mm  $\times$  8 mm at the tip. The laminator is a plug with a series of straight holes that force the velocity of the outer flow to equalize azimuthally. The ablation zone height is set by the focus of the laser, and is 2 mm in height and 1.5 mm in width. At the ablation zone the fluence of the laser when running at 250 mW power is 2.6 J/cm<sup>2</sup>.

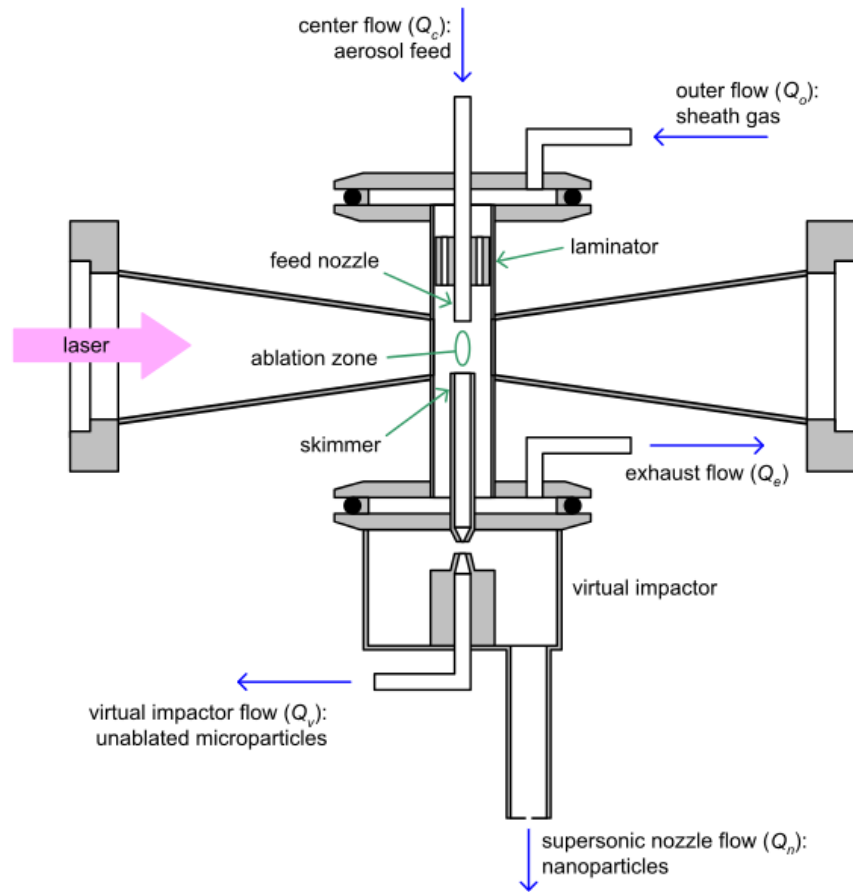


Figure 2.6: Schematic of the ablation chamber showing the center and outer flows, the ablation zone, and the skimmer and exhaust flows. Also shown, is the virtual impactor which will be discussed later. Taken from [22].

The center flow from the aerosol feeder is set so that each laser pulse (200 Hz) ablates a plug of aerosol flowing through the ablation zone just once. There is also an outer flow (sheath gas or coaxial flow) that is matched to the velocity of the center flow through the chamber so that laminar flow is maintained and this prevents the center gas from expanding into the open region of the cell. A skimmer tube is used to collect the ablated nanoparticles from the laminar flow and direct them into the virtual impactor.

The skimmer tube and virtual impactor are the same ones used previously [22]. The excess gas from the chamber is exhausted to a fume hood.

### **Double Ablation**

There are modifications to the LAMA process presented above that are used to produce unique nanostructures including islanded NPs, core-shell NPs, and non-equilibrium alloy NPs. An islanded NP consists of a large nanoparticle (10 - 40 nm) that is decorated with many isolated, smaller (1 - 5 nm) NPs of a different material, as shown in Fig. 2.8. To make islanded metal-on-oxide NPs, two ablations of different materials must be performed sequentially using the process illustrated in Fig. 2.7. First, ablation is conducted on oxide NPs and then these NPs are fed into a second chamber containing metal NPs. After the first ablation, the oxide NPs from the first chamber are too small to effectively focus the laser to the back surface and initiate a shock, and thus, the oxide NPs are largely unaffected by the laser. However, these particles provide the nucleation sites onto which the particles of the metal NPs can grow after the second ablation [31].

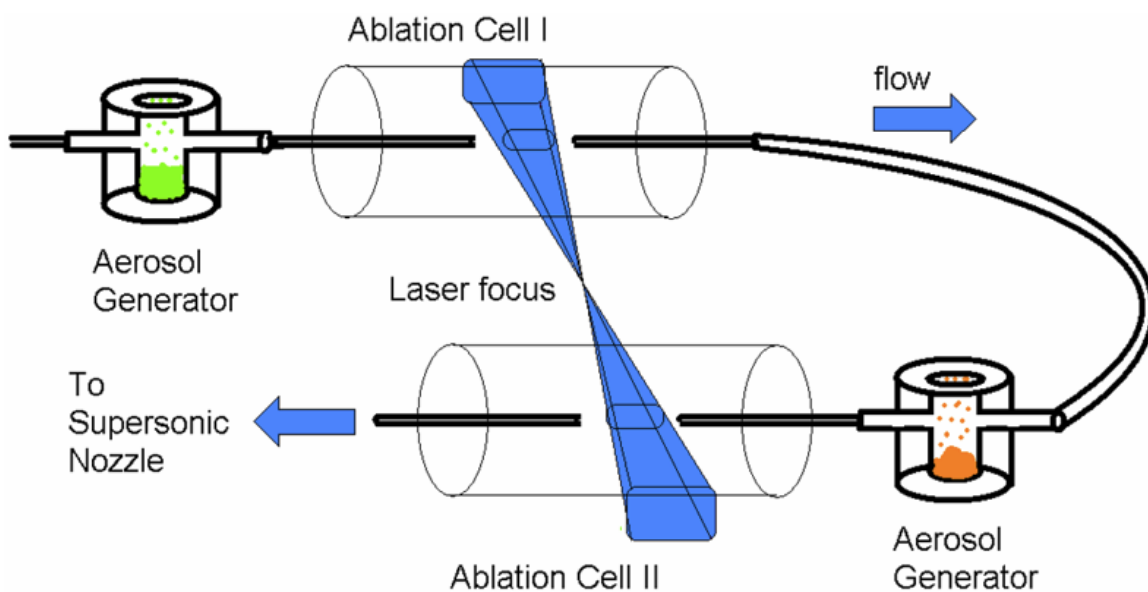


Figure 2.7: Double ablation schematic showing how the gas flows through the first aerosol feeder on the top left, through the first ablation cell into a second feeder, and into the second ablation cell. This method was used to create islanded nanoparticles and core-shell nanoparticles. Taken from [7].

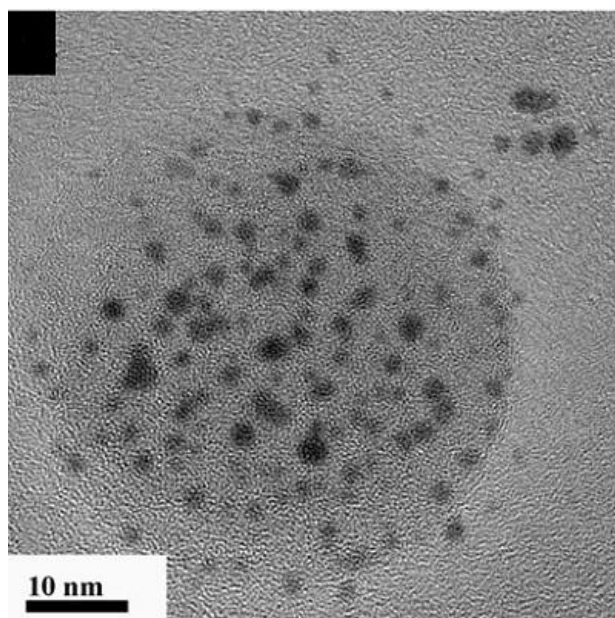


Figure 2.8: TEM bright-field image of LAMA-produced metal-on-oxide NP consisting of Au-on-TiO<sub>2</sub>. Taken from [31].

Core-shell particles have also been demonstrated using the same process as the islanded particles, Fig 2.7, but the materials used for both the core and shell were III-V semiconductors [32]. To obtain a shell rather than islanded particles, the density of particles produced during the second ablation must be sufficiently high to completely coat rather than partially coat the core and the coating material should be able to wet the seed particle.

Non-equilibrium, alloy nanoparticles have also been demonstrated using an approach similar to that used to produce islanded and core-shell NPs [23]. To produce alloy NPs, a mixture of two different metal NPs are introduced into the ablation chamber and ablated simultaneously. During ablation, the expanding plasma plumes overlap and where this occurs, the NPs that form are alloys of the two metals.

#### ***Overview and Issues; Design of first double ablation cell***

The original proof-of-concept and preliminary results demonstrating sequential double ablation were conducted by Gallardo and Nahar, respectively [32, 31]. These experiments were conducted using glass tubes to flow the aerosols and rubber stoppers as connections. This setup, while providing a high degree of flexibility in varying of experimental parameters, was neither repeatable or controllable.

The concept for the previous design was to allow the aerosol to follow the green arrows shown in Fig. 2.9; ablation would occur in the first chamber, then pass up and out to the second feeder and mix with the second microparticles of the second material before being ablation occurred in the second chamber. However, what actually happened is shown with the red arrow in Fig. 2.9; the aerosol would short circuit through the laser path. The particles within the short circuit experienced a much more prolonged laser exposure than was expected before mixing with the microparticles from the second feeder. This created

a turbulent ablation region that is not well controlled and resulted in a large distribution of particle sizes and also lowered production efficiency. Thus, this design for a double ablation cell was abandoned.

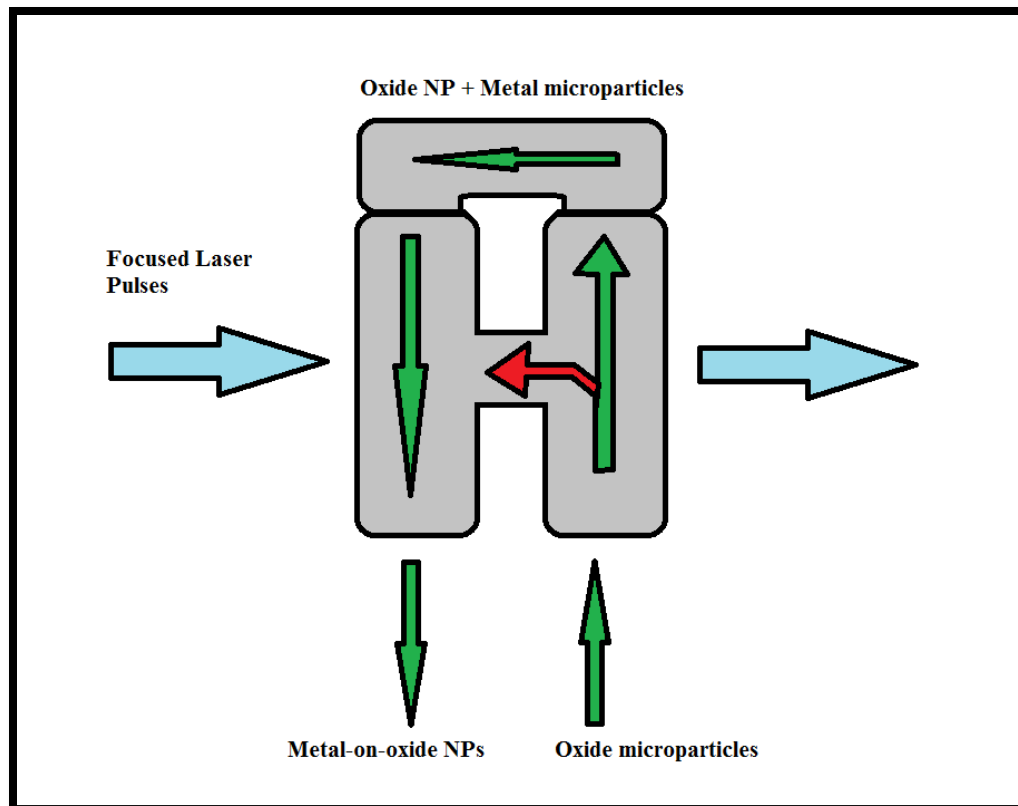


Figure 2.9: Diagram showing the desired flow of aerosol during double ablation in green, and the actual flow of aerosol in red.

### ***Second Ablation Cell***

An attempt at fixing the short circuiting problem was to design and build a cell that would minimize the diameter of the gap between the chambers so that it was no larger than necessary to allow the passage of the laser between the two ablations zones, as shown in Fig. 2.10. The premise was that, if the gap was small enough, most of the aerosol would

follow the green path in Fig. 2.9. Unfortunately, this design still suffered a significant amount of short circuiting of the particles and could not be used for controlled double ablation experiments.

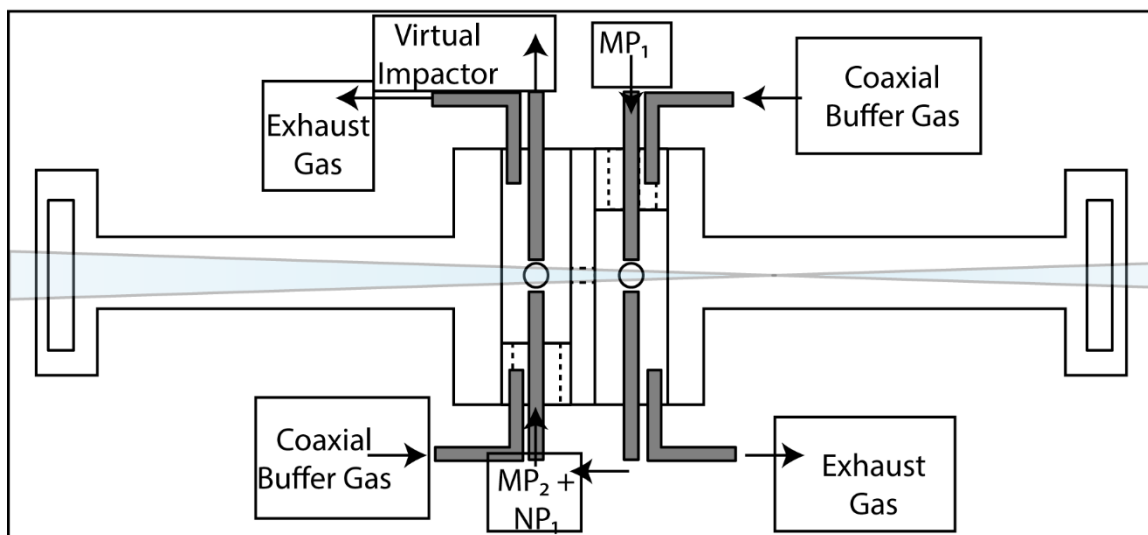


Figure 2.10: Schematic of the second double chamber ablation cell.

Nevertheless, this cell proved to still be useful as a single ablation chamber by closing off one ablation cell. The benefit of using this as a single chamber ablation cell is that there is no virtual impactor built in, and this is necessary for the first ablation of a two-chambered double ablation setup described later. The chamber diameter is 16.67 mm, the feed nozzle has a cross sectional area of  $4.23 \text{ mm}^2$ , and the skimmer nozzle is a thin walled 6.35 mm diameter tube.

### ***Simultaneous Ablation***

The second chamber was used for simultaneous ablation of two microparticles in a single chamber, as shown in Fig. 2.11. For these experiments, a metal and a metal oxide were ablated simultaneously resulting in the formation of individual nanoparticles of metal

and oxide. Upon impaction (discussed later in this chapter) metal-in-oxide films were produced using this approach.

### ***Two-Chamber Approach***

The final method used to make metal-on-oxide films was to use two separate single ablation chambers and split the laser beam in two, as shown in Fig. 2.11. The oxide was ablated in the first chamber and then the aerosol was routed directly into the second feeder. Within the second feeder, NPs mixed with metal microparticles and were fed into the second ablation chamber. Since the nanoparticles were much smaller than the wavelength of the laser, they did not absorb much energy, but the microparticles were ablated in an aerosol where the oxide nanoparticles already existed. The drawback with this method was that the laser must be run at twice the fluence compared to the other methods that were discussed earlier and this laser power can only be maintained for short run times before overheating of the laser caused it to shut down. Nevertheless, this was the method used to create all metal-on-oxide nanoparticles and metal-on-oxide nanoparticle films.

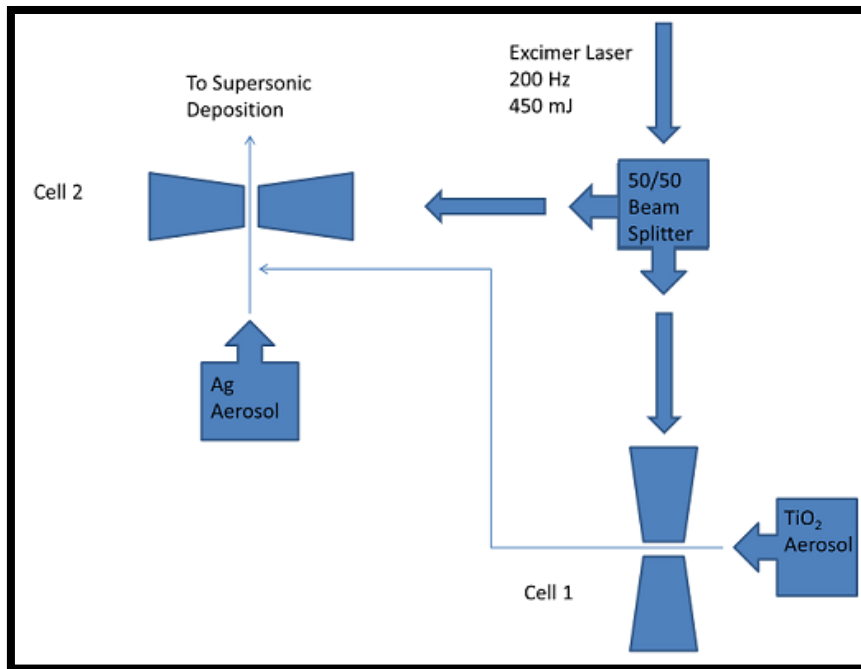


Figure 2.11: Diagram showing the two-chamber method used to make islanded nanoparticles. The excimer laser was split using a mirror. Each beam was then focused into two separate ablation cells. The nanoparticle aerosol from the first ablation was then mixed with the microparticle aerosol of the second feeder, using the bulb design shown in Fig. 2.4b. This aerosol mixture was routed into the second ablation cell.

## FILTRATION

As shown previously, the parameters of a virtual impactor can be tuned to filter the larger unablated microparticles from an aerosol stream containing NPs [24]. This is important so that the deposition dynamics are not disturbed by large microparticles and so that the uniformity of deposited films were maintained. As shown below, the aerosol from the skimmer of the ablation chamber is virtually impacted onto 3 mm diameter orifice filled with stagnant gas. Particles smaller than 500 nm remain entrained within the flow lines that lead to the exhaust outlet of the chamber, but the larger particles that have significant momentum stay in the stagnant region. A smaller flow of 100 SCCM is maintained out of

this region to ensure this region does not clog up with particles. The remaining nanoparticles are fed into the deposition chamber.

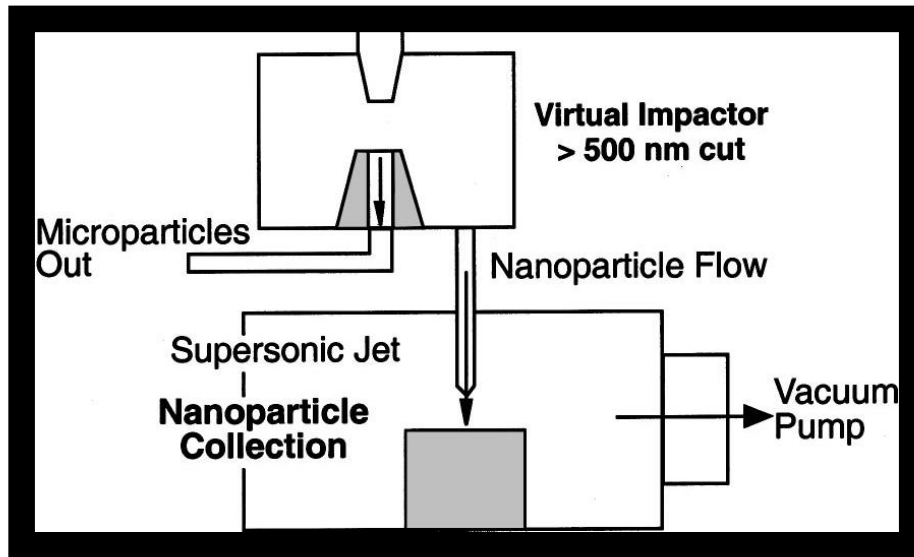


Figure 2.12: Schematic of the virtual impactor used to filter out unablated microparticles from the NP aerosol. This aerosol is then fed into the deposition chamber. Taken from [24].

## DEPOSITION

The supersonic deposition method was the same as that used previously to pattern films [27]. This method utilizes a large mechanical backing pump with a roots blower, to pump out the deposition chamber to 150 mTorr - 1 Torr. This chamber is equipped with a substrate holder on a motorized x-y stage. A small 250 or 1000  $\mu\text{m}$  diameter nozzle is positioned above the substrate which sits on the substrate holder. The NP aerosol flows into this nozzle at atmospheric pressure and the pressure differential across this nozzle accelerates the gas and NPs within the aerosol to high enough velocity that they stick to the substrate upon impaction. The programmed motion of the stage results in a patterned film.

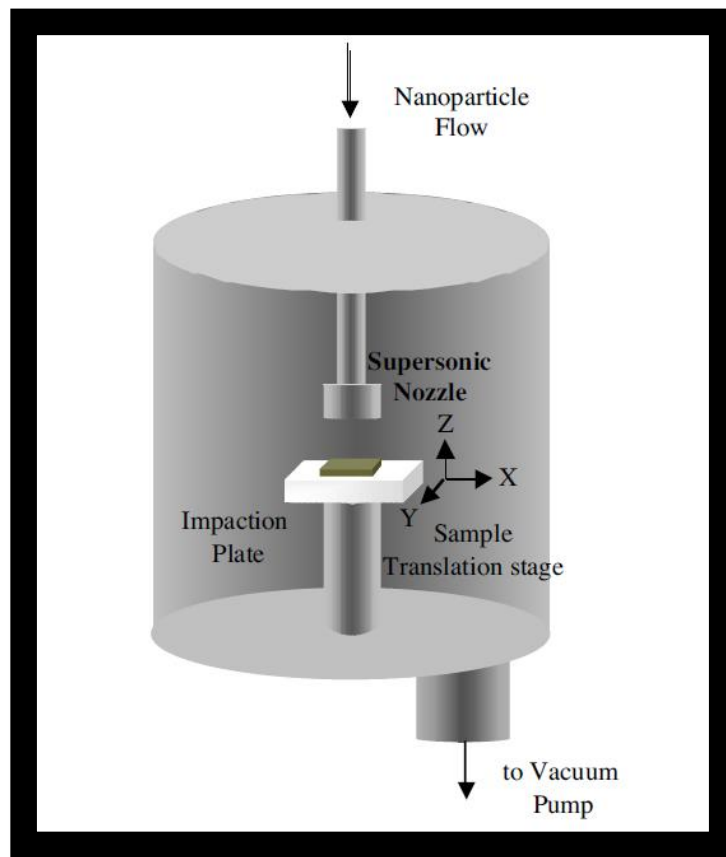


Figure 2.13: Schematic of the supersonic deposition chamber used to deposit patterned films of NPs generated by LAMA. The NP flow from the virtual impactor is passed through a nozzle into a vacuum chamber. The gas is accelerated by a pressure differential and this in turn accelerates the nanoparticles. These nanoparticles are impacted onto a substrate that is translated using an x-y stage and programmed to pattern films. Taken from [33].

### LabVIEW Control of Stepper Motors

The x-y stage consists of two stepper motors with control boards that were programmed with LabVIEW® software. The controller is used to generate a pulse-train of signals that drives the stepper motors. Although in theory this method of controlling an x-y stage should be effective, in practice there were many problems maintaining the

synchronization between the motors that resulted in missed steps at the end of a segment. This in turn would result in writing errors that would cause discrepancies between the programmed and actual patterns of the films.

As part of this dissertation research, the LabVIEW® code, Appendix A, was rewritten to force synchronization between the controller and stepper motor and to create an easier template for writing patterns. A preview window that showed the expected pattern was also made. Case states and error checking were introduced, as suggested by best practices in LabVIEW® coding. The results of these improvements were reductions in (1) the amount of time needed to program a new pattern, (2) the time taken to write the films, and (3) the number of attempts needed to write the film due to patterning errors.

### **Diffusion Collection of Nanoparticles for TEM Examination**

A novel method of collecting NPs was employed for collecting NPs without impacting the particles at high velocity. This method was used because previous attempts to collect NPs onto TEM grids via impaction resulted in significant damage to the TEM grids. For this method of collection, a previously used virtual impactor chamber (50 mm inner diameter and 6 mm tubes at the top and bottom) was modified for this dissertation research and inserted in between the functional virtual impactor and the deposition chamber, as shown in Fig. 2.14.

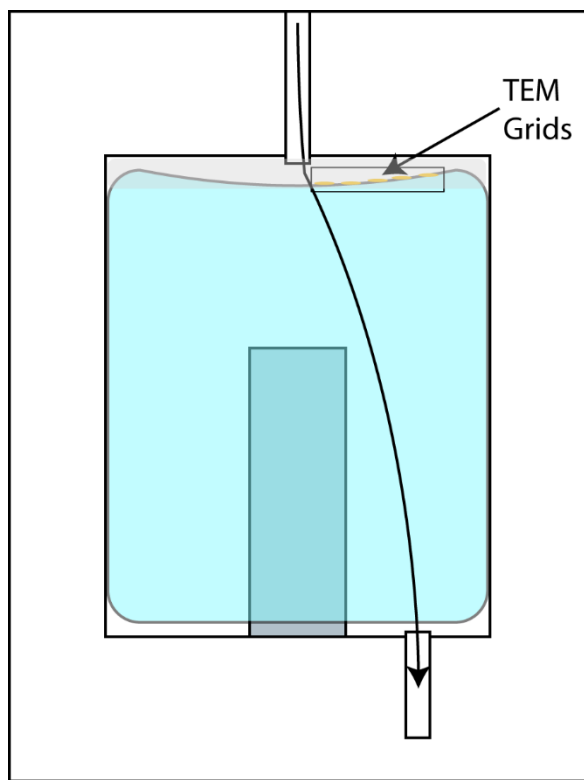


Figure 2.14: Schematic of the chamber used to collect TEM grid samples. The flow from the virtual impactor passes through this chamber filled with glass wool (shown in blue). TEM grids are placed on the glass wool so that the NPs diffuse onto the surface of the grids.

The bottom nozzle is removed, and the chamber is filled with glass wool such that the flow through this chamber is slowed to a rate where diffusion of NPs onto TEM grids occurs. TEM grids are placed on top of the glass wool with an average diameter of  $9.5 \pm 1.6 \mu\text{m}$ , SEM micrographs shown in Fig. 2.15, and after a few minutes, are covered with nanoparticles that have soft landed on the grids. Many grids can be collected at once.

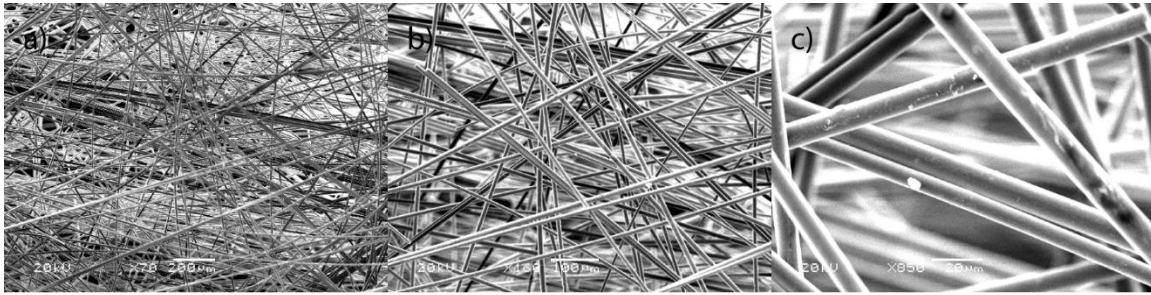


Figure 2.15: SEM micrographs of glass wool used to support TEM grid for diffusion collection. Magnifications were a) 70×, b) 160×, and c) 850×.

### LAMA PROCESS PARAMETERS

The process parameters used for each of the experimental set-ups are summarized in Tables 2.1 and 2.2 and in Figures 2.16 and 2.17.

#### Single Chamber Ablation

	Mass flow rate (sccm)		Description
Q1	200		Center flow, carrying MPs to ablation zone
Q2	0-200		Portion of center flow passing through feeder
Q3	5921		Coaxial flow to maintain a laminar flow regime
Q4	2401		NP aerosol + unablated MPs
Q5	4720		Excess gas exhaust
Q6	2209		NP aerosol
Q7	192		Unablated MPs exhaust
	Nozzle Diameter (mm)		
	0.25	1	
Q8	0	33135	Buffer gas
Q9	2209	35344	Supersonic nozzle flow (NP aerosol)

Table 2.1: Gas flows used in LAMA process for single chamber ablation deposition using 0.25 and 1 mm deposition nozzles.

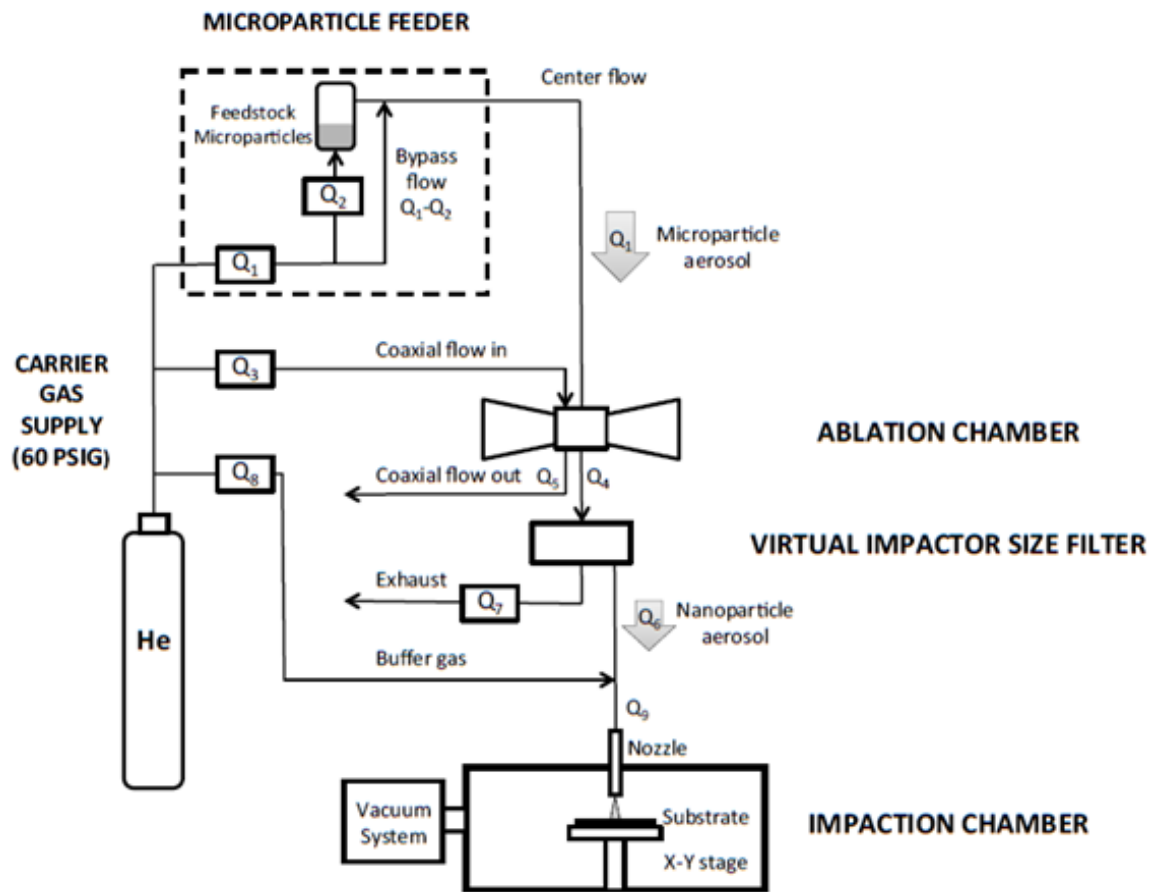


Figure 2.16: Flow diagram of the single chamber LAMA process. Gas was flowed through an aerosol feeder then through an ablation cell. An outer flow was also flowed to create laminar gas flow through the cell. Taken from [34].

## Two-Chamber Ablation

	Mass flow rate (sccm)	Description
Q1	100	Chamber 1 center flow, carrying oxide MPs to ablation zone 1
Q2	0-100	Portion of center flow passing through feeder 1
Q3	5136	Chamber 1 coaxial flow to maintain a laminar flow regime
Q4	100	NP aerosol + unablated MPs
Q5	5136	Chamber 1 excess gas exhaust
Q6	100	Additional center flow for feeder 2
Q7	0-100	Portion of center flow passing through feeder 2
Q8	5040	Chamber 2 coaxial flow to maintain a laminar flow regime
Q9	200	NP aerosol + unablated MPs
Q10	2840	Chamber 2 excess gas exhaust
Q11	2209	NP aerosol
Q12	192	Unablated MPs exhaust
Q13	2209	Supersonic nozzle flow (NP aerosol)

Table 2.2: Gas flows used in LAMA process for two-chamber ablation deposition using 0.25 mm nozzle.

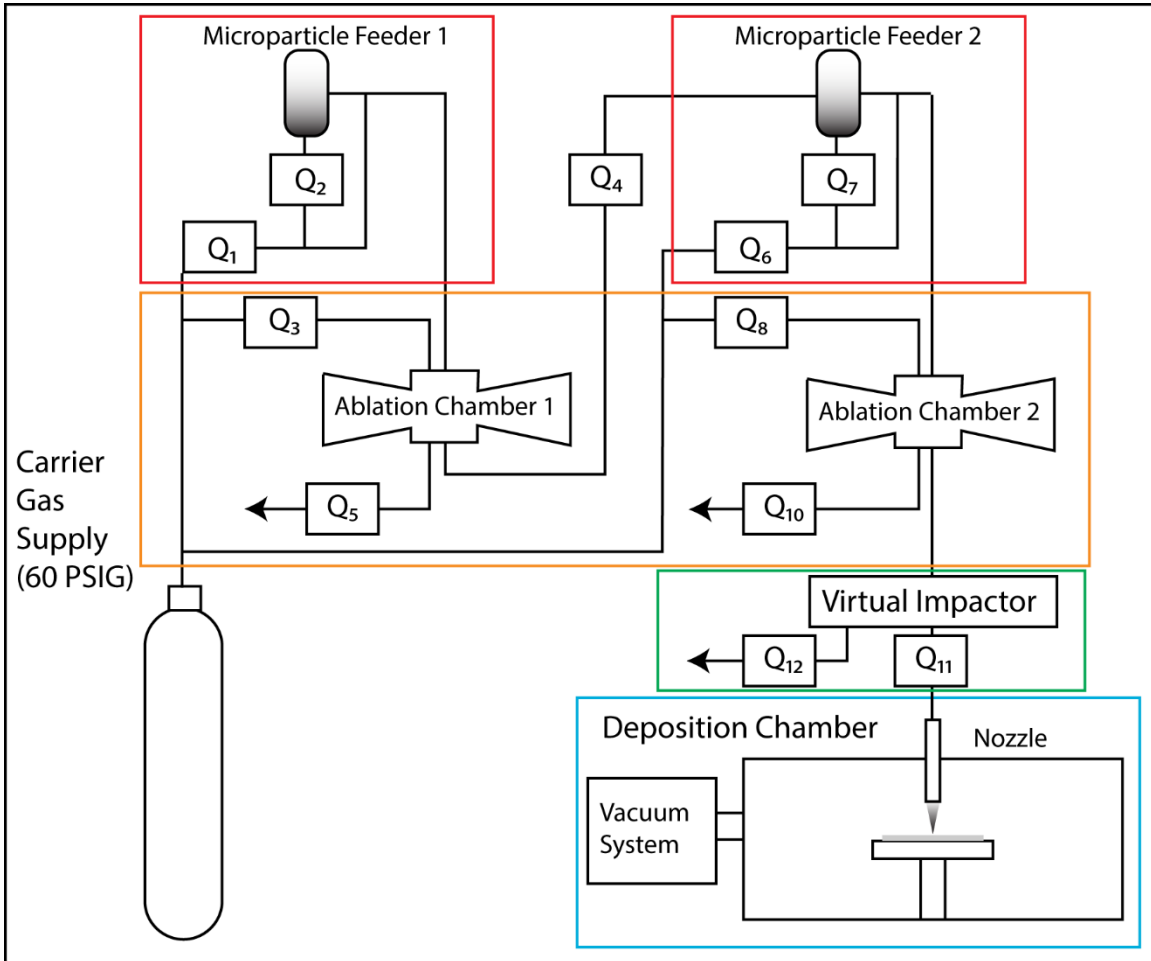


Figure 2.17: Flow diagram of the two-chamber LAMA process.

## Nanoparticle and Film Characterization

### RAMAN SPECTROSCOPY

Raman spectroscopy is a technique that utilizes inelastically scattered monochromatic light to measure vibrational, rotational, and other low-frequency modes of a system of molecules. Raman has been demonstrated to be an invaluable tool in understanding the adsorption and binding energy between hydrocarbons and metal catalysts [35]. As seen from Fig. 2.18, the energy levels of the vibrational states are probed with the Raman technique. Fig. 2.18a shows incident light of photon energy,  $E_L$ , which is scattered with no change in energy; i.e. elastic scattering. In contrast, when Raman scattering occurs there is a change in the scattered light  $E_S$  equal to  $E_L$  minus the energy of the vibrational mode  $\hbar\omega_v$ . However, the wavelength of the light incident on a molecule does not have to be resonant with the energy levels of the molecule to induce Raman scattering events. That is why the temporary excited state is called a virtual state, shown in Fig. 2.18c and Fig. 2.18d. The difference in photon energy between the incident light and the Raman scattered light can be measured to determine the energy of the probed vibrational states.

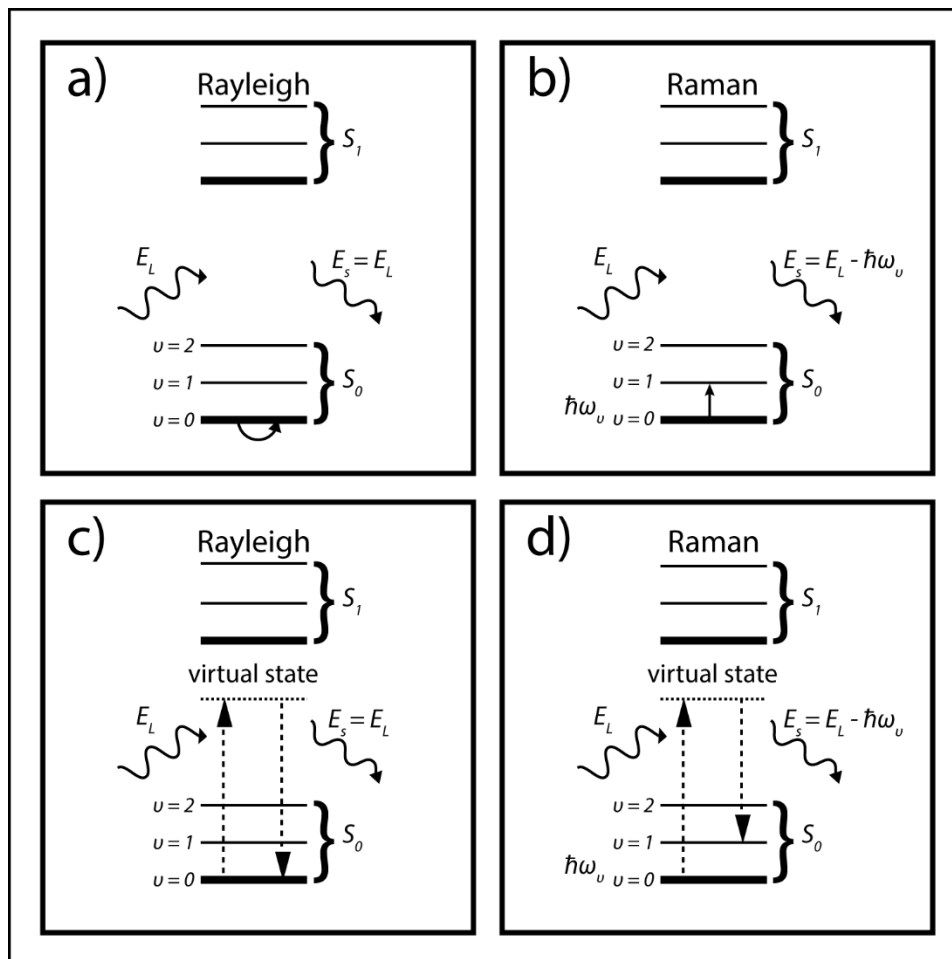


Figure 2.18 Simplified Jablonski diagrams illustrating schematically the Rayleigh (a) and Raman (b) scattering processes. An alternative way of visualizing these scattering processes from a quantum mechanical point of view is shown in (c) and (d). Taken from [36].

## SURFACE ENHANCED RAMAN SPECTROSCOPY

Surface-enhanced Raman spectroscopy (SERS) is a technique that utilizes the increase in the Raman signal that occurs near roughened or nano-structured metals. When a molecule is close to these metal surfaces, the Raman signals are much larger partly due to electromagnetic enhancements, called plasmon resonances, some of which are explained in Fig. 2.19. The first two plots show the differences between enhancement effects for 25

nm particles of glass and silver with respect to visible wavelengths. Silver has a very strong enhancement around 360 nm and the closer to this resonance the wavelength of the exciting laser is, the larger the enhancement in Raman signal. The last plot shows that when two NP's of silver are 2 nm apart there is a further enhancement occurs due to this gap and this enhancement is strong across most of the visible spectra. The total enhancement in SERS can be as large as about  $10^5$  compared to conventional Raman.

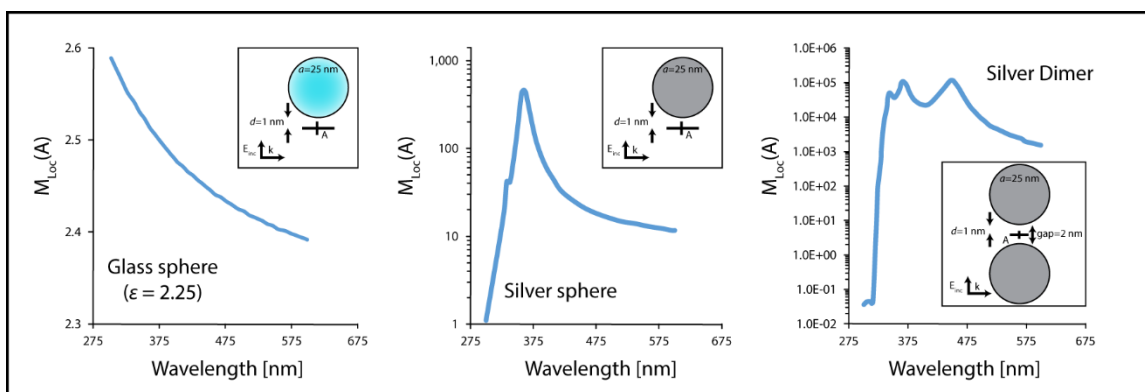


Figure 2.19 Electromagnetic enhancements responsible for increased signal in SERS, taken from [35].

Another point for consideration in SERS is that molecules bind to the surfaces of metal substrates and when this occurs the vibrational modes are altered and subsequently the Raman peaks shift as well. The degree to which the modes are altered is related to the binding energy between the metal and molecules and thus, the shift in the Raman peaks can be used to determine both the configuration of the molecule on the surface and the energy of adsorption. Since the adsorption energy for a molecule on a specific metal surface can also be calculated using density functional theory (DFT), these Raman peak shifts can be predicted [17]. The combination of experimental Raman measurements and

the DFT prediction can be a powerful technique in understanding and predicting adsorption behavior of gasses on metal surfaces.

### Gas Cell Design for Ethylene

To measure the Raman spectra of ethylene gas on the surface of LAMA-produced films, a method was devised to ensure that only ethylene gas was present when Raman measurements were taken. A pressure cell was designed, Appendix B, that allows Raman spectra to be taken from films produced via LAMA *in situ*, as shown in Fig. 2.20. The two valves that seal and allow gas to flow to and from the cell and are represented with the circles and crosses. NPs are deposited onto aluminum substrates. The film/substrate is then placed inside of the cell, the cell is evacuated, and then back-filled with ethylene. The window on the top allows the focused laser beam of a micro-Raman instrument to excite molecules on the surfaces of the film/substrate and then collect this light.

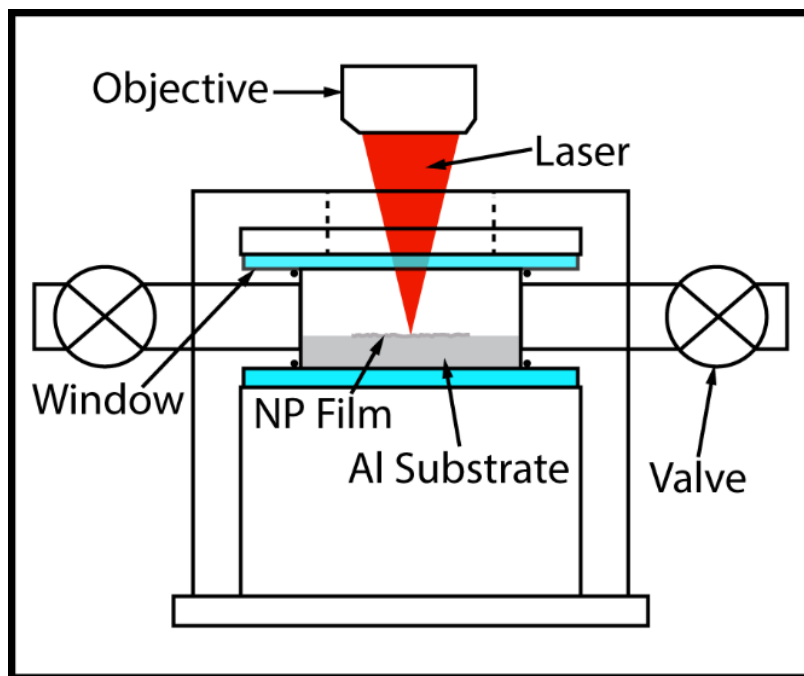


Figure 2.20 Schematic of pressure cell for gas on NP Raman measurements.

## Experimental Procedures for SERS

The single ablation chamber process was used to produce nanostructure films deposited on aluminum substrates. Gas flows are given in Table 2.1 and the routing is shown in Fig. 2.16. As shown in Fig. 2.4a, microparticles of the desired composition (Ag, Au, or Au-Cu alloy particles) were aerosolized using a fluidized bed feeder and the aerosol flowed through an ablation chamber, as shown in Fig. 2.6. A coaxial buffer gas that surrounded the aerosol was used to constrain the gas through the ablation cell. Helium was used at 1 atm for both the microparticle aerosol and the buffer gas. The microparticle powders were 1.5 - 2.0  $\mu\text{m}$  diameter Ag (P-311J®, DuPont Inc., Wilmington, DE), 1.5 - 2.0  $\mu\text{m}$  diameter Au (D100920-68®, DuPont Inc., Wilmington, DE), and 44  $\mu\text{m}$  diameter Au<sub>0.35</sub>/Cu<sub>0.65</sub> (35Au-65Cu-325MESH, Wesgo Metals, Hayward, CA). A KrF excimer laser (Lumonics Pulsemaster PM-848®, Nepean, ON, Canada) with a pulse energy of 250 mJ, wavelength of 248 nm, and pulse-width of 12 ns was focused into the aerosol using cylindrical lenses to an area of 3 mm by 1.5 mm, which resulted in a fluence on the microparticles of  $\sim 2.8 \text{ J/cm}^2$ . The resultant NPs, determined by observation in a transmission electron microscope, were spherical with distributions in sizes ranging from 2-10 nm in diameter.

The supersonic deposition process was used to impact the LAMA-produced NPs to produce films with nanoscale roughness [27]. The NP aerosol was first routed through a virtual impactor, shown schematically in Fig. 2.12, to separate any unablated particles. The aerosol was then directed to a flat-plate nozzle with a diameter and plate-thickness of 250  $\mu\text{m}$ . The substrates were placed on a motorized x-y motorized stage inside the deposition chamber, which was pumped down to  $<27 \text{ Pa}$  using a mechanical vacuum pump backing a roots blower that had a combined capacity of 5,500 l/min. The pressure differential at the nozzle accelerated the NPs to a velocity of  $\sim 600 \text{ m/s}$  prior to impaction onto aluminum

substrates [27]. The substrates were translated using x-y stepper motors to pattern films with x-y-z dimensions of 3 mm × 3 mm × ~100 μm, as shown in Fig. 2.13.

The resulting films were used as SERS substrates in the custom-built gas chamber, shown in Fig. 18, to determine the binding energy of ethylene gas to the metal NPs. For comparison with the LAMA-produced films, commercially available SERS substrates of Ag and Au were also obtained (SERStrates®, Silmeco, Copenhagen, Denmark). A Raman microscope (Horiba LabRam HR, Kyoto, Japan) was used with a 633 nm laser at ~2 mW laser power and a 20× long working distance objective (Zeiss LD Plan-Neofluar® 20x/0.4 Corr Ph2) for the Au and Au/Cu samples. Another Raman microscope (WiTec Alpha300 R®, Ulm, Germany) with a 488 nm laser at 2 - 10 mW and a 20× long working distance objective (Zeiss LD Plan-Neofluar 20×/0.4 Corr Ph2) was used for the Ag and Ag-on-TiO<sub>2</sub> samples. For both instruments, the custom gas chamber was filled with 2 atm of 99.999% ethylene and Raman spectra were taken from the surface of the films.

## **METAL-ON-OXIDE PARTICLES**

The thermal stability of metal NPs and metal-on-oxide NPs were studied using *in situ* and *ex situ* transmission electron microscope (TEM) experiments. These experiments used a specially designed heating stage that utilized a heated TEM holder.

### ***In-Situ* Heating Experiments**

The two-chamber ablation process was used to produce Ag-on-TiO<sub>2</sub> NP samples. Gas flows are given in Table 2.2 and the routing is shown in Fig. 2.17. First, TiO<sub>2</sub> microparticles were synthesized using a published process [37]. These particles were fed into the first ablation chamber using the fluidized bed feeder described in Fig. 2.4a. The TiO<sub>2</sub> NPs were then directed into the side of the feeder described in Fig. 2.4b. This feeder was filled with 1.5 - 2.0 μm diameter Ag microparticles (P-311J®, DuPont Inc.,

Wilmington, DE), and the resulting aerosol that consisted of a mixture TiO<sub>2</sub> NPs and Ag microparticles were fed into the second ablation chamber. A KrF excimer laser (Lumonics Pulsemaster PM-848®, Nepean, ON, Canada) with a pulse energy of 450 mJ, wavelength of 248 nm, and pulse-width of 12 ns passed through a half-mirror beam-splitter to create two beams with a pulse energy of approximately 225 mJ each. These beams were focused into the aerosols using cylindrical lenses to an area of 3 mm × 1.5 mm, which resulted in a fluence on the microparticles of ~ 2.5 J/cm<sup>2</sup>.

The Ag-on-TiO<sub>2</sub> NP aerosol was flowed through a virtual impactor to remove any unablated material, then flowed through the diffusion cell shown in Fig. 2.14. Arduro Protochips® grids, Fig. 2.21b, were used to collect the particles. These grids were loaded into a JEOL 2010F TEM, using the Arduro Protochips® holder, Fig. 2.21a. The NPs were heated rapidly and then held at a constant temperature for observations and to capture micrographs. The temperature was increased in 50 °C increments and micrographs were taken at each interval.

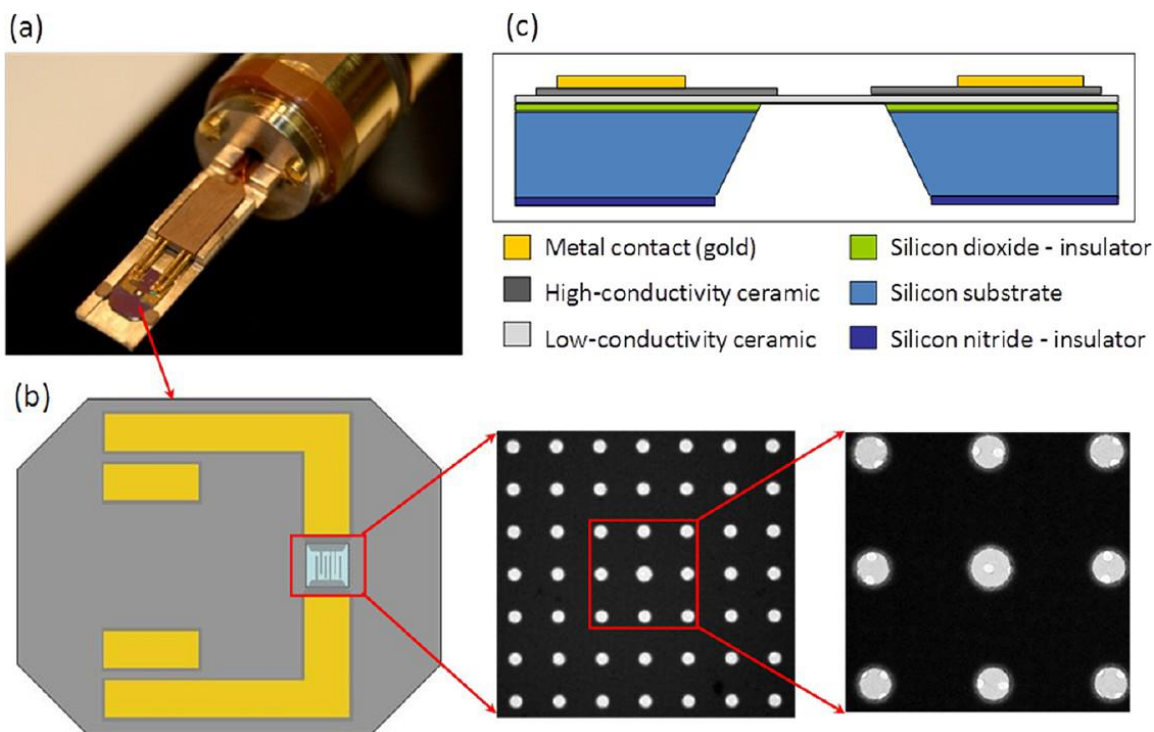


Figure 2.21: (a) Tip of Protochips® specimen holder showing heater chip clamped into place, with electrical leads connected. (b) Top view schematic of Protochips heater chip. The insets are low magnification TEM images of the central region of the chip showing the pattern of holes in the low-conductivity ceramic membrane and holey carbon support film overlaying the holes in the ceramic membrane. (c) Cross-section view of chip (courtesy of Protochips Inc.).

For the HR-TEM digital micrographs, lattice parameters were measured using ImageJ (version 1.50b, National Institutes of Health, United States) software. The scale bar was measured and the pixels/Å was set using the feature in the software. A line was drawn perpendicular to the lattice fringes that were being measured, with the starting and ending points representing either minimums or maximums in the lattice fringe. The plot profile feature was used to display the intensity changes across the line. The distance of the line was measured and the maximums of the intensity profile were counted. The distance was then divided by the number of maxima, and the result was the lattice spacing

distance. This was compared to known X-ray diffraction data for Ag and TiO<sub>2</sub> allotropes and used to identify the crystalline regions.

### ***Ex Situ* Heating TEM Micrographs**

Ag NPs were created using the same single chamber ablation conditions used for the Au NPs in the Raman experiments. Gas flows are given in Table 2.1 and the routing is shown in Fig. 2.16. Ag-on-TiO<sub>2</sub> NPs were produced using the same two chamber ablation conditions described above for the *in situ* samples. Ag and Ag-on-TiO<sub>2</sub> NPs were collected using the diffusion chamber on Au TEM grids (Pelco 500 mesh®, Ted Pella Inc., Redding, CA) which did not contain a carbonaceous support substrate.

One grid of each Ag and Ag-on-TiO<sub>2</sub> NPs were heated to 500°C for 1 hour in flowing Ar environment inside of a tube furnace, and one set was heated to 500°C for 1 hour in ambient air. One set was not heated as a control. Digital micrographs were captured with a JEOL 2010F TEM of NPs on each grid.

### **SiO<sub>2</sub> AND METAL-IN-SiO<sub>2</sub> DENSE FILMS**

The process for SiO<sub>2</sub> NP and metal-in-SiO<sub>2</sub> NP films manufacture and subsequent post-deposition annealing step is described below. It is assumed that the dominant mass transfer mechanisms at the temperatures used in this experiment are surface and grain-boundary diffusion. Ideally, the sintering conditions would favor grain-boundary diffusion which would result in densification of the films. Maximizing the as-deposited film density favors densification and because the as-deposited film density increases with impaction energy, the larger 1 mm supersonic deposition nozzle was used for deposition of the SiO<sub>2</sub> NPs. These process conditions have been shown to produce Ag NP films with as-deposited relative densities of 70% [25]. These Ag films were subsequently rapid-thermal annealed

and showed an increase in density to a final film density of greater than 90%. A similar heating process is described below for SiO<sub>2</sub> NP and metal-in-SiO<sub>2</sub> films.

### **SiO<sub>2</sub> NP Films**

SiO<sub>2</sub> (9010®, Duke, Palo Alto, CA) microspheres with a diameter of 9.6 μm were ablated using the single ablation conditions described previously and shown in Fig. 2.16 with gas flows given in Table 1. The SiO<sub>2</sub> NPs were supersonically impacted onto glass microscope slides and a 1 mm deposition nozzle was used to produce films. Additional gas was needed to be able to reach the choked flow regime of the nozzle; this was added after the virtual impactor with a 3-way t-connector. The transmission spectra of the films were measured using a UV-Vis spectrometer (Cary 5000, Agilent, Santa Clara, CA). A stylus profilometer (Dektak 6M, Veeco, Oyster Bay, NY) was used to measure the thickness of the films.

### **Metal-in-SiO<sub>2</sub>**

1.5 - 2.0 μm diameter Au (D100920-68®, DuPont Inc., Wilmington, DE), 1.5 - 2.0 μm diameter Ag (P-311J®, DuPont Inc., Wilmington, DE), Pt (1015609®, Degussa Corp., South Plainfield, NJ), and Cu (7440-50-8®, Aldrich, Milwaukee, WI) powders were mixed with 9.6 μm SiO<sub>2</sub> (9010®, Duke, Palo Alto, CA) microspheres. This powder mixture was ablated simultaneously using the feeder shown in Fig. 2.4a, and the single ablation conditions described for the Raman samples. Gas flows are given in Table 2.1 and the routing is shown in Fig. 2.16. Supersonic impactation onto glass microscope slides with a 1 mm deposition nozzle was used to produce films of metal-in-SiO<sub>2</sub>. Additional gas was needed to be able to reach the choked flow regime of the nozzle; this was added after the virtual impactor with a 3-way t-connector. The transmission spectra of the films were measured using a UV-Vis spectrometer (Cary 5000, Agilent, Santa Clara, CA). A stylus

profilometer (Dektak 6M, Veeco, Oyster Bay, NY) was used to measure the thickness of the films.

### **Post-deposition heating Treatment**

The study of the sintering characteristics of the SiO<sub>2</sub> and metal-in-SiO<sub>2</sub> NP films was conducted by using a hot-plate in a metal box and attached to a proportional-integral-derivative (PID) controller and a type K thermocouple was used to measure temperature. This hot-plate furnace was used to heat the NP films to temperatures of 400° C for 1 hour. The transmission spectra of the films were measured using a UV-Vis spectrometer (Cary 5000, Agilent, Santa Clara, CA). A stylus profilometer (Dektak 6M, Veeco, Oyster Bay, NY) was used to measure the thickness of the films.

## **CHAPTER 3: BINDING ENERGIES OF ETHYLENE TO NANOPARTICULATE FILMS PRODUCED BY LAMA**

In this chapter, the ability to tune the binding energy between ethylene and a metallic nanoparticulate films is studied by varying the compositions of NPs. Density functional theory (DFT) calculations<sup>1</sup> are used to predict the binding energies for a range of atomic configurations and alloy compositions. Nanoparticulate films were then produced using LAMA and the Raman spectra of ethylene gas adsorbed onto these metallic NP films are presented and used to assess the binding energies. One particular alloy composition, Au<sub>0.35</sub>/Cu<sub>0.65</sub>, is explored in more detail due to the interesting behavior of this alloy. In addition, the source of the unusually broad Raman peaks that were measured on LAMA films is explored and discussed. Lastly, a comparison of ethylene binding to Ag NP films to that of the binding to Ag-on-TiO<sub>2</sub> NP films is also presented.

### **Raman Spectroscopy and SERS of Ethylene on Metals**

Previously, DFT was used to calculate the binding energies between ethylene and various metals and metal alloys [17]. It was found that binding energies between ethylene and metals generally increases linearly as the d-band center approaches the Fermi level. Amongst the metals and alloys studied [17], Ag had the weakest chemisorption binding, although its binding was still too strong to be viable for industrial separations. For several alloys that were previously investigated [18, 19], the binding energies with ethylene were between the end members of the alloys.

---

<sup>1</sup> Simulations including DFT calculations were performed by Shannon Stauffer and Graeme Henkelman from the Department of Chemistry at the University of Texas at Austin.

Here, the binding energy of ethylene to Au and Au/Cu alloys are studied. DFT is used to calculate the binding energies, of ethylene to Ag, Au, Cu, and Au/Cu alloys and the results suggest that a Au/Cu alloy can have a lower binding energy than either Au or Cu. The binding energies of ethylene to metal surfaces is correlated to the C=C vibrational frequency,  $\nu(\text{CC})$ , which can be measured experimentally. Samples were prepared from the Au and Au/Cu alloys and experimental measurements were made of the surface-enhanced Raman spectra (SERS) of at the surfaces of these alloys in the presence of ethylene. The DFT calculations and experimental measurements show good agreement and subsequent analysis is presented to explain the apparent anomaly that the binding energy of ethylene to the Au/Cu alloy is weaker than either to pure Au or Cu.

#### **AG, AU, AND AU-CU ALLOY FILMS**

The laser ablation of microparticle aerosols (LAMA) process was used to produce the metal nanoparticles (NPs) and alloy NPs used in these experiments. LAMA has the advantage that very fast cooling rates allow non-equilibrium alloys to be produced. For example, it has previously been shown that face-centered cubic Au/Cu alloys can be produced with a broad spectrum of compositions, and without bulk phase segregation predicted by the equilibrium phase diagram [23]. A supersonic deposition process was used to impact the LAMA-produced NPs to produce films with nanoscale roughness [27]. The resulting films were used as SERS substrates in a custom-built gas chamber to measure the Raman spectra of ethylene gas on the metal NPs.

For modeling, the energies were calculated with DFT as implemented in the Vienna *ab initio* simulation package [38]. The projector-augmented wave framework was used to describe the core electrons [39, 40] and valence electrons were described by single-electron Kohn-Sham wave functions [38, 41]. The generalized gradient approximation with the

PBE functional was used to describe electronic correlation and exchange. The wave functions of the valence electrons were expanded in a plane-wave basis set up to a kinetic energy cutoff of 300 eV; increasing this cutoff to 350 resulting in changes of binding energy of only 0.005 eV. Spin-polarization was considered in all cases. Gaussian-type smearing with a width of 0.01 eV around the Fermi level was used to improve convergence. All systems were optimized to their ground-state geometry until the forces on each atom were less than 0.01 eV/Å.

Two geometries were considered, metallic NPs and slabs. Metallic NPs were modeled with 79-atom in a face-centered cubic (FCC) lattice and a truncated octahedral geometry with 8 Å of vacuum separating periodic images. Slabs were constructed with the lowest energy {111} surface planes. Four layers were used to describe all slabs except the alloy for which five were used. Lattice constants were determined from relaxation of bulk cells; the bottom two layers of the slabs were frozen in these bulk geometries. The slabs were separated by 20 Å of vacuum. The Brillouin zone was sampled at the  $\Gamma$ -point for the NPs and a 4x4x1 k-point mesh for the slabs. In the alloys, atoms were randomly assigned element types consistent with the overall composition.

Vibrational frequencies were calculated by diagonalization of the Hessian matrix, constructed by displacement of all atoms in the ethylene molecule by a finite-difference step size of 0.01 Å. Dispersion corrections were tested using the Tkatchenko-Scheffler method [42, 43] were found to increase binding energies by ~0.3 eV and decrease phonon frequencies by no more than 15 cm<sup>-1</sup>. The trends in binding energy and frequencies were not significantly impacted, thus no reported values are given with dispersion corrections. It is well documented that DFT calculations using generalized gradient-approximation (GGA) functionals tend to underestimate lattice constants and thus also underestimate vibrational mode frequencies [44].

## Results

Experimental Raman spectra for ethylene on  $\text{Au}_{0.35}/\text{Cu}_{0.65}$ , Au, and Ag are shown in Fig. 3.1. Broad peaks are clearly observed that correspond to the  $\nu(\text{CC})$  mode at  $\sim 1590 \text{ cm}^{-1}$  for Ag and  $\text{Au}_{0.35}/\text{Cu}_{0.65}$  and at  $\sim 1560 \text{ cm}^{-1}$  for Au. In addition, the  $\delta(\text{CH}_2)$  mode is observed at  $\sim 1325 \text{ cm}^{-1}$  for  $\text{Au}_{0.35}/\text{Cu}_{0.65}$  and Au and at  $\sim 1350 \text{ cm}^{-1}$  for Ag. Also shown on this plot are the predicted  $\nu(\text{CC})$  frequency shifts for Ag,  $\text{Au}_{0.35}/\text{Cu}_{0.65}$ , Au, and Cu. In previous studies, it was shown that the  $\nu(\text{CC})$  mode was at  $1539 \text{ cm}^{-1}$  on Au films and  $1543 \text{ cm}^{-1}$  on Cu films [35]. What is remarkable about the data in Fig. 3.1 is that the  $\nu(\text{CC})$  mode of ethylene on the Au/Cu alloy is higher than either Au or Cu, indicating that the binding energy for the alloy is lower than for either Au or Cu.

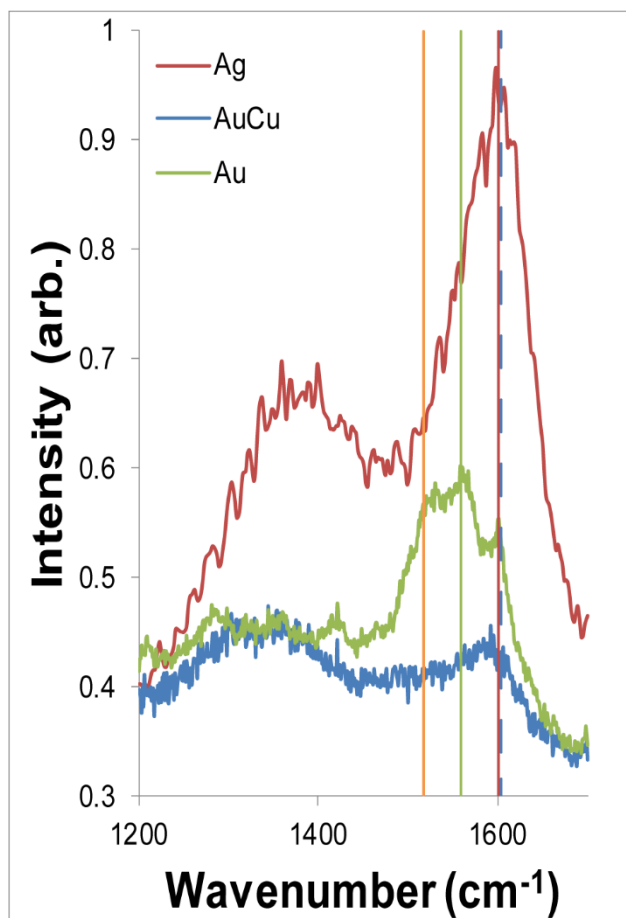


Figure 3.1: Raman spectrum for ethylene on a SERS Au<sub>35</sub>/Cu<sub>65</sub> alloy (blue) film. The C=C peak of ethylene is shifted from the unbound position of 1623 cm<sup>-1</sup> [24] to ~1590 cm<sup>-1</sup>. The spectra for ethylene on SERS Ag (red) and Au (green) NP film are also shown for reference. Calculated frequency shifts of the C=C stretching mode of ethylene bound to Ag (red vertical line), Au (green vertical line), Cu (orange vertical line, and Cu@Au (core@shell, blue dashed line) nanoparticles are shown.

The breadth of the peaks in the Raman spectra shown in Fig. 3.1 were considerably broader than those measured previously [35]. It should be noted that the current measurements were made using ethylene gas whereas the previous measurements were made after condensing the ethylene onto the SERS films. Measurements made on commercial Ag SERS substrates (see Fig. 3.2) using ethylene gas also show considerably

sharper peaks than those obtained on LAMA-produced films, indicating that some of the source of the broadening is related to characteristics of the LAMA film. However, the peak widths measured from commercial SERS substrates are still considerably broader than those obtained previously on metal films using condensed ethylene. As shown in Fig. 3.2, increasing the laser power from  $\sim 0.1$  mW to  $\sim 0.5$  mW (corresponding to fluences of  $\sim 880$  and  $\sim 4400$  W/cm<sup>2</sup>, respectively) further broadened the peaks. Observations of the surfaces of the LAMA-produced films in a scanning electron microscope revealed that, although they were relatively rough at the nanoscale, regularly spaced gaps between the NPs were largely absent. It is well known that the gap spacing plays a critical role in peak enhancement in SERS [36], so non-optimized gap sizes such as observed in the LAMA-produced films would be expected to significantly weaken and broaden the SERS spectra. Further weakening and broadening is expected in Au and Au/Cu alloys relative to Ag since previously it has been shown that peak intensities decrease going from Ag to Cu to Au [45]. For the current experiments, the advantages of LAMA in being able to produce quantities of non-equilibrium alloy NPs sufficient to produce thick films outweighs their non-optimized performance as SERS substrates compared to commercial substrates.

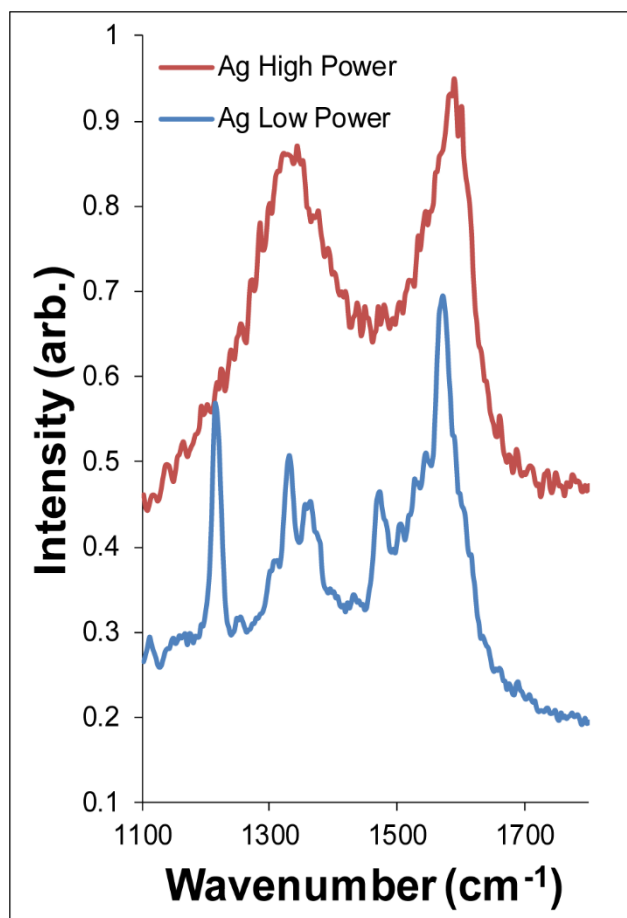


Figure 3.2: Raman spectra measured at two laser intensities for ethylene on commercially obtained Ag SERS substrates near the frequency of the C=C stretch. The peak breadth increases with laser power. The spectral intensities were scaled for ease of viewing.

DFT calculations of ethylene binding to pure Au, Cu, Ag and alloy Au/Cu systems were conducted in an effort to explain the observed Au/Cu alloy Raman spectra. Small,  $\sim 1.0$  nm (79-atom) NPs and infinite slab surfaces were considered, and it was found that size effects did not significantly affect the trends in binding energies and frequencies across compositions that are of interest here. Different binding sites exhibited similar trends for 79-atom NPs and slabs, which is consistent with previous findings [17]. Therefore 79-atom NPs were initially sampled for trends in binding energy over a range of binding sites

and NP compositions. Figure 4 shows the predicted binding energy versus C=C stretch frequency for different binding sites of Ag, Au, Cu, and Au/Cu alloy 79-atom NPs. A nearly linear correlation is apparent between the binding energy and the frequency with Ag {111} face sites having the weakest binding (highest  $\nu(\text{CC})$  frequency), followed by the Ag edge (step), Au {111} and the Cu edge sites. Cu {111} face sites are an outlier having similar binding energy to Au {111} sites, but much lower frequency than Ag edge (step) sites. These results are consistent with the predictions of a previous study that showed that ethylene binds strongly to edge sites and less strongly to {111} surfaces for all systems [17]. This linear correlation of C=C stretch frequency and ethylene binding energy holds for Au/Cu random alloy particles as well, with the binding energies and  $\nu(\text{CC})$  frequencies lining within the range of the pure Au and Cu systems.

In our search for a plausible theoretical model for the measured ethylene on Au/Cu alloy Raman spectra, we identified a trend in binding energy for both pure metal NPs and alloyed Au/Cu NPs, but the predicted range of binding energies and frequencies of the  $\text{Au}_{0.35}/\text{Cu}_{0.65}$  random alloy NPs using this approach is between its end-member metal NPs, Au and Cu, which is not consistent with the experimentally determined Raman spectra. To understand the source of this inconsistency, it was necessary to consider likely scenarios for preferential ethylene binding and surface segregation. Ethylene binding to Cu sites on an alloy surface is stronger than binding to Au sites of equivalent alloys, and thus ethylene should preferentially bind to all available Cu sites before Au. For a  $\text{Au}_{0.35}/\text{Cu}_{0.65}$  random alloy, a majority of surface sites would be Cu, and since ethylene strongly binds to Cu, the average  $\nu(\text{CC})$  stretching frequency would be lower than for ethylene adsorbed on a Au surface. The SERS Au/Cu substrate, though, had a measured  $\nu(\text{CC})$  frequency much higher than that of the SERS Au substrate, 1590 and 1560  $\text{cm}^{-1}$ , respectively. This suggests that the ethylene binding measured is ethylene bound to Au sites. These results can be

explained by preferential segregation of Au atoms to the surfaces of the Au/Cu alloys, and indeed this is the expected behavior in the Au/Cu system [46]. To test whether segregation of Au to the surface is thermodynamically stable, we swapped the identity of a surface Cu to Au of a  $\text{Au}_{0.35}/\text{Cu}_{0.65}$  random alloy NP. The energy difference of the swapped NP and the original configuration was -0.21 eV, indicating it is thermodynamically favorable for Au to segregate to the surface. X-ray photon spectroscopy (XPS) performed on our Au/Cu film was consistent with this hypothesis, shown in Fig. 3.3. XPS conducted on the surface of the Au/Cu film showed the presence of only Au but sputtering to remove the surface revealed the presence of both Au and Cu.

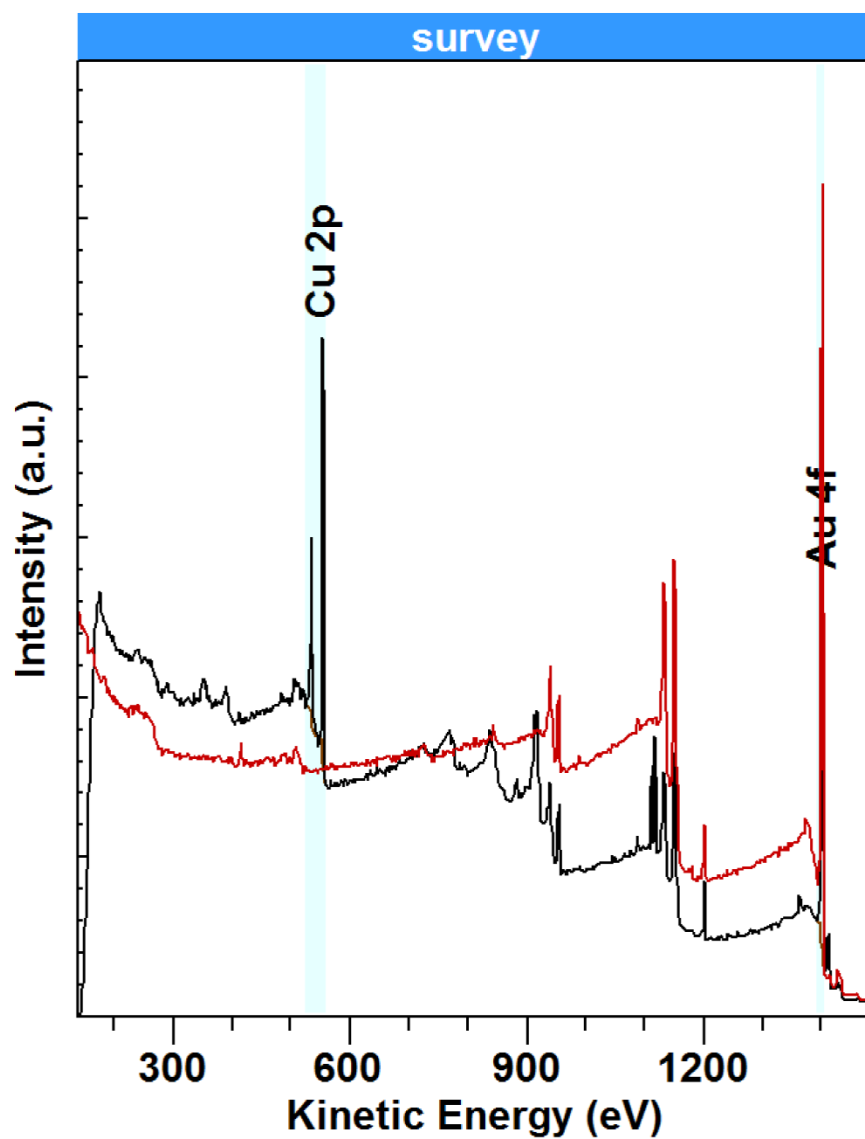


Figure 3.3: XPS spectra of Au/Cu NP film before sputtering (red) and after (black). The Cu 2p peaks are present after sputtering but not before indicating that Au has segregated to the surface of the film.

Accordingly, we considered a model in which Au was segregated to the surface of the Au/Cu alloy particle. This model was the core@shell Cu@Au 79-atom NP shown in Fig. 3.4. The binding energy of ethylene on a {111} facet is appreciably weaker for the alloy, 0.03 eV, than a pure Au or Ag metal NP, 0.32 and 0.09 eV, respectively, while binding to an edge site, 0.41 eV, is within the range of random alloy NP binding sites. The predicted C=C stretch frequency for ethylene bound to a Cu@Au NP on the {111} facet and edge site are 1674 and 1563  $\text{cm}^{-1}$ , respectively.

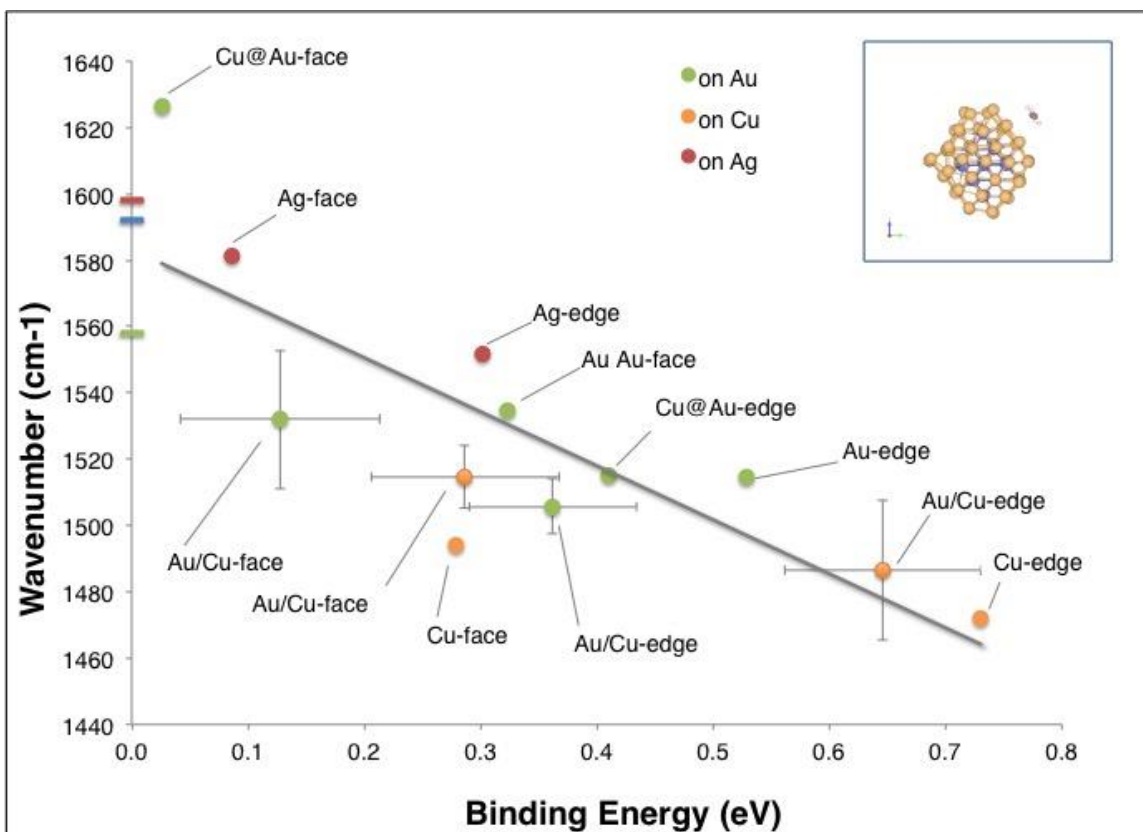


Figure 3.4: Calculated binding energy versus C=C stretch frequency for 79 atom Ag, Au, Cu, Au<sub>0.35</sub>Cu<sub>0.65</sub> and Cu@Au (coreshell) NPs on different binding sites. Random Au<sub>0.35</sub>/Cu<sub>0.65</sub> alloys (labeled Au/Cu) are shown with the standard deviation taken from 30 calculations, and single calculations were carried out for all other NPs, since there is only one composition possible with these models. Data are presented by the adsorbing metal, Ag (red), Au (green) and Cu (orange) and are given as Ag-face (model composition-binding site). Experimental frequencies are indicated on the y-axis, Ag (red), Au/Cu (blue), Au (green). Inset: Image of the Cu@Au<sub>79</sub>-atom NP with adsorbed ethylene on a {111} facet site—Cu atoms (blue), Au (yellow), C (brown).

Since the nanoparticles in the SERS film were larger than the DFT model, with particles in the range of 2 - 10 nm, the calculations were repeated for the large-size limit: metal slabs. Specifically, the lowest energy {111} surface was chosen, which is expected to dominate in the experiment. Figure 3.5 shows the results for Ag, Au, and Cu slabs compared to a Au<sub>0.35</sub>/Cu<sub>0.65</sub> random alloy slab with a monolayer of gold on the surface

(denoted as AuCu@Au). The results are consistent with the NP calculations. The AuCu@Au slabs were found to weakly adsorb ethylene to the surface with a  $\nu(\text{CC})$  stretching frequency of  $\sim 30 \text{ cm}^{-1}$  higher than an Ag {111} surface; a shift of  $70 \text{ cm}^{-1}$  was calculated for the Cu@Au.

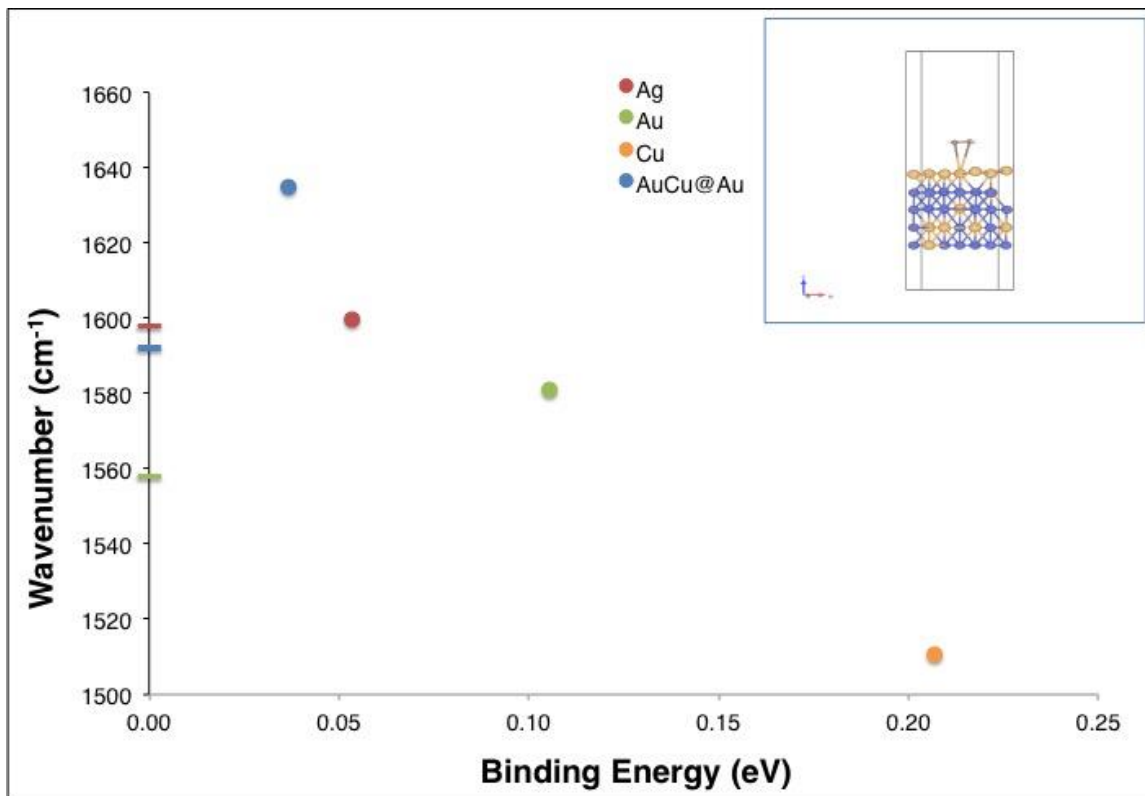


Figure 3.5: Binding energy versus C=C stretch frequency of ethylene on Au<sub>0.35</sub>/Cu<sub>0.65</sub> random alloy slab with a surface layer of gold (denoted as AuCu@Au). The calculated value for Ag, Au, and Cu slabs are given for reference, as well as the experimental values on the y-axis, Ag (red), Au/Cu (blue), Au (green). Inset: Image of AuCu@Au with an adsorbed ethylene molecule—Cu atoms (blue), Au (yellow), C (brown).

## Discussion

In a previous theoretical study, adsorption energy to a core@shell NP was at the extremes of the alloy end-members [47], and a related experimental study noted the segregation of a more noble metal to the surface of a NP increased the catalytic activity of the substrate [48]. In the Au/Cu alloy system studied here, it was found that the binding energy of ethylene to the Cu@Au {111} facets are lower than either end-member. Experimental and theoretical evidence suggests that the nanoparticle substrate is Au-surface-enriched. The calculated weaker binding energy on this surface corresponds to a higher  $\nu(\text{CC})$  frequency than on Ag by  $30\text{ cm}^{-1}$ , pushing the predicted frequency above the measured Au/Cu SERS peak. The Au-surface segregated model therefor provides a plausible explanation of the experimental frequency shifts measured in our SERS experiments of Au/Cu films.

## AG-ON-TiO<sub>2</sub> NP FILMS

To study the how TiO<sub>2</sub> affects the binding of ethylene to Ag, Raman spectra of ethylene on Ag and Ag-on-TiO<sub>2</sub> films were conducted. Since the nanodisk-on-TiO<sub>2</sub> produced by Goodman *et al.* were only several atomic layers thick, the substrate had an effect on the catalytic activity of the Au. The Ag NPs decorating the TiO<sub>2</sub> for the current study are an order of magnitude thicker than Goodman *et al.*'s, and the short-range order of this effect would not be expected to change the binding energy of Ag to ethylene. However, if metal-on-TiO<sub>2</sub> is to be considered for applications in lieu of unbound metal NPs, it must be known for certain if any long-range effects to the binding energy between the metal NPs and the analytes exist.

Experimental Raman spectra for ethylene on Ag-on-TiO<sub>2</sub> and Ag are shown in Fig. 3.6. Broad peaks are clearly observed that correspond to the  $\nu(\text{CC})$  mode at  $\sim 1590\text{ cm}^{-1}$  for Ag-on-TiO<sub>2</sub> and Ag. In addition, the  $\delta(\text{CH}_2)$  mode is observed at  $\sim 1350\text{ cm}^{-1}$  for both.

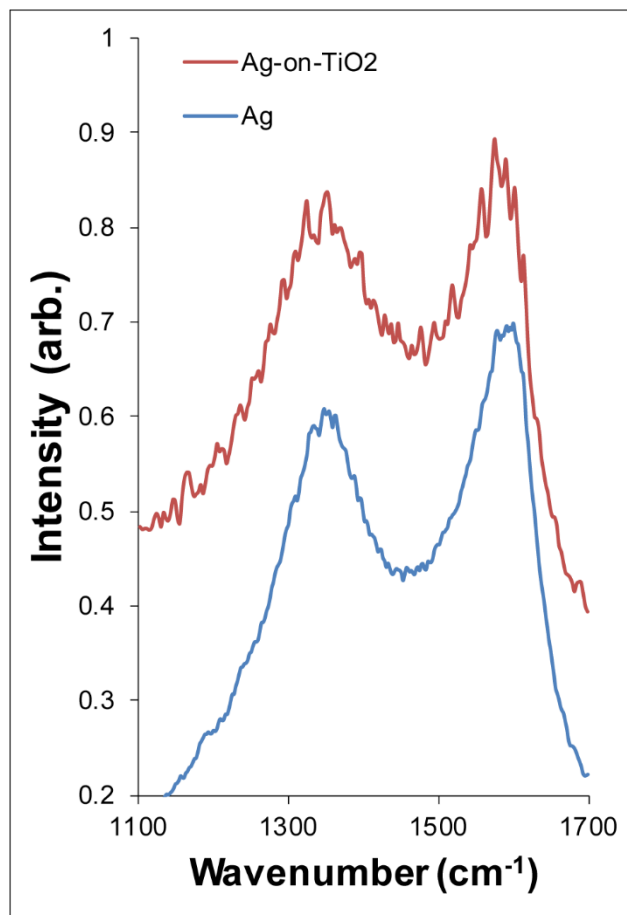


Figure 3.6: Raman spectra measured for ethylene on LAMA-produced Ag and Ag-on-TiO<sub>2</sub> NP films near the frequency of the C=C stretch. The spectral intensities were scaled for ease of viewing.

The experimentally determined peak locations of ethylene on Ag were found to be in good agreement with the predicted peak shifts, and the Ag-on-TiO<sub>2</sub> films also align very closely with these same peaks. The broadening that was observed from the ethylene spectra measured from the Ag, Au, and Au<sub>0.35</sub>/Cu<sub>0.65</sub> films was also observed with the Ag-on-TiO<sub>2</sub> films.

## Discussion

What is interesting about the spectra in Fig. 3.6 is that the  $\nu(\text{CC})$  mode of ethylene on Ag NPs is in the same location as the ethylene on Ag-on-TiO<sub>2</sub> NPs. This suggests that the binding energy of the ethylene to Ag is not altered by the TiO<sub>2</sub> NPs as a substrate. This confirms that since the Ag NPs are thick enough that there is no measurable interaction with the TiO<sub>2</sub> and does not influence the binding energy with ethylene. LAMA-produced metal-on-oxide NPs in this size regime are not a method of tuning the binding energy of the metal NPs. However, if these metal-on-oxide NPs were shown to have the same sintering-resistance as the particles of Goodman *et al.*[49], they could be used in higher temperature systems by using an oxide NP as an inert substrate to stabilize smaller metal NPs. Compared to the ultra-high vacuum deposition process used to Goodman *et al.*, LAMA offers the advantage of high production rates and a robust environment.

## CONCLUSIONS

Since weak chemisorption of ethylene is crucial to developing a facilitated transport, nanoparticle composite membrane, a promising Au/Cu alloy was studied using a combination of DFT modeling and SERS measurements. It was found that ethylene has a similar binding energy to Au<sub>0.35</sub>/Cu<sub>0.65</sub> and Ag surfaces, and a considerably lower binding energy than to Au or Cu and this was rationalized by showing that Au segregates to the surface of Au<sub>0.35</sub>/Cu<sub>0.65</sub> alloys. An optimal alloy for a nanoparticulate membrane for separations should have an even lower binding energy to ethylene than that measured here for Ag and our Au<sub>0.35</sub>/Cu<sub>0.65</sub> systems [16]. The current work suggests that, this may be possible via a thorough screening of compositions and surface structures of Au/Cu alloy nanoparticles. Previously calculated compositions that show promise are Au<sub>0.25</sub>/Ag<sub>0.75</sub> random alloy and Ag@Au core/shell NPs [17].

Additionally, once a composition and surface structure is found that is most favorable for the use in a facilitated transport membrane for the separation of ethylene from ethane, these metal NPs can be produced on TiO<sub>2</sub> NPs without any change to the engineered binding energy with ethylene. These metal-on-TiO<sub>2</sub> NPs could potentially allow for higher operating temperatures of the membrane without microstructural changes to the metal NPs.

## CHAPTER 4: METAL-ON-TiO<sub>2</sub> POROUS FILMS

As discussed in the Chapter 2, a critical bottleneck in the use of nanoparticles in high temperature catalysis is their lack of thermal stability. Specifically, at elevated temperatures, coarsening of the metal nanoparticles occurs by either surface diffusion of the particles or by an Ostwald ripening process where individual atoms or small clusters of atoms dissolve onto the substrate surface, diffuse on the surface, and then redeposit onto larger particles [50]. Coarsening decreases the specific surface area of the nanoparticles and therefore decreases catalytic activity. The development of coarsening-resistant nanoparticles would therefore greatly expand potential application areas for nanoparticles in catalysis.

In this chapter, a process method for producing Ag-on-TiO<sub>2</sub> NPs and NP films is presented and the thermal stability of these nanostructures is studied. The hypothesis is that the thermal stability of the metal particles on the TiO<sub>2</sub> surface is strongly related to binding of the particles on the oxide surface. However, the binding mechanism of the Ag NPs to the TiO<sub>2</sub> NPs is not understood, although oxygen vacancy sites on the oxide are thought to locally bind particles more strongly to the surface. Thermal stability is studied by *ex situ* and *in situ* TEM heating Ag-on-TiO<sub>2</sub> NPs produced via LAMA. These results suggest that the Ag NPs are bound to oxygen vacancies in the TiO<sub>2</sub>, which previous research has shown provides strong resistance to coarsening of metal NPs [7].

### Morphology of Ag-on-TiO<sub>2</sub> NPs and NP Films

A two-chambered ablation method, depicted previously in Fig. 2.11, was used to produce Ag-on-TiO<sub>2</sub> NPs. First, 1 - 4  $\mu\text{m}$  spherical TiO<sub>2</sub> powder was synthesized using a previously published method [37]. This powder was used in the first feeder and subsequently ablated in the first chamber. The resultant NPs were flowed into a second

feeder, shown in Fig. 2.4b, containing Ag feedstock powder. This aerosol composed of Ag microparticles and TiO<sub>2</sub> NPs was flowed into the second ablation chamber where ablation of the Ag occurred, but the TiO<sub>2</sub> remained largely unaffected. The result was the metal NP deposited onto the oxide surface. The NPs were collected onto TEM grids with Formvar<sup>®</sup> substrate backings, using the diffusion cell shown in Fig. 2.14.

High resolution TEM (HR-TEM) and high angle annular dark field (HAADF) STEM studies were conducted on the Ag-on-TiO<sub>2</sub> samples collected onto the TEM grids and representative micrographs are shown in Fig. 4.1a-b. Figure 4.1a shows that samples consist primarily of chains of agglomerates of TiO<sub>2</sub> NPs as the support structure with Ag NPs decorated on the surface of the oxide particles. The sizes of the support agglomerate structures vary from a few TiO<sub>2</sub> NPs to chains as long as 200 nm. The TiO<sub>2</sub> primary particles within the agglomerates range in size from approximately 5 – 25 nm. Since the TiO<sub>2</sub> NPs formed by the LAMA process are rapidly cooled, the observed structure is amorphous. This increases the difficulty of visualizing the NPs, since the contrast between the TiO<sub>2</sub> and the polymer TEM support is minimal and the usual methods of enhancing contrast of crystalline materials, such as tilting the specimen, are not effective for amorphous materials. Thus, HAADF STEM (Fig. 4.1b) was used because the atomic mass contrast that arises in HAADF STEM allows easier identification of the Ag particles. The Ag particles range in size from 1 - 20 nm and are mostly isolated from each other, Fig. 4.1d.

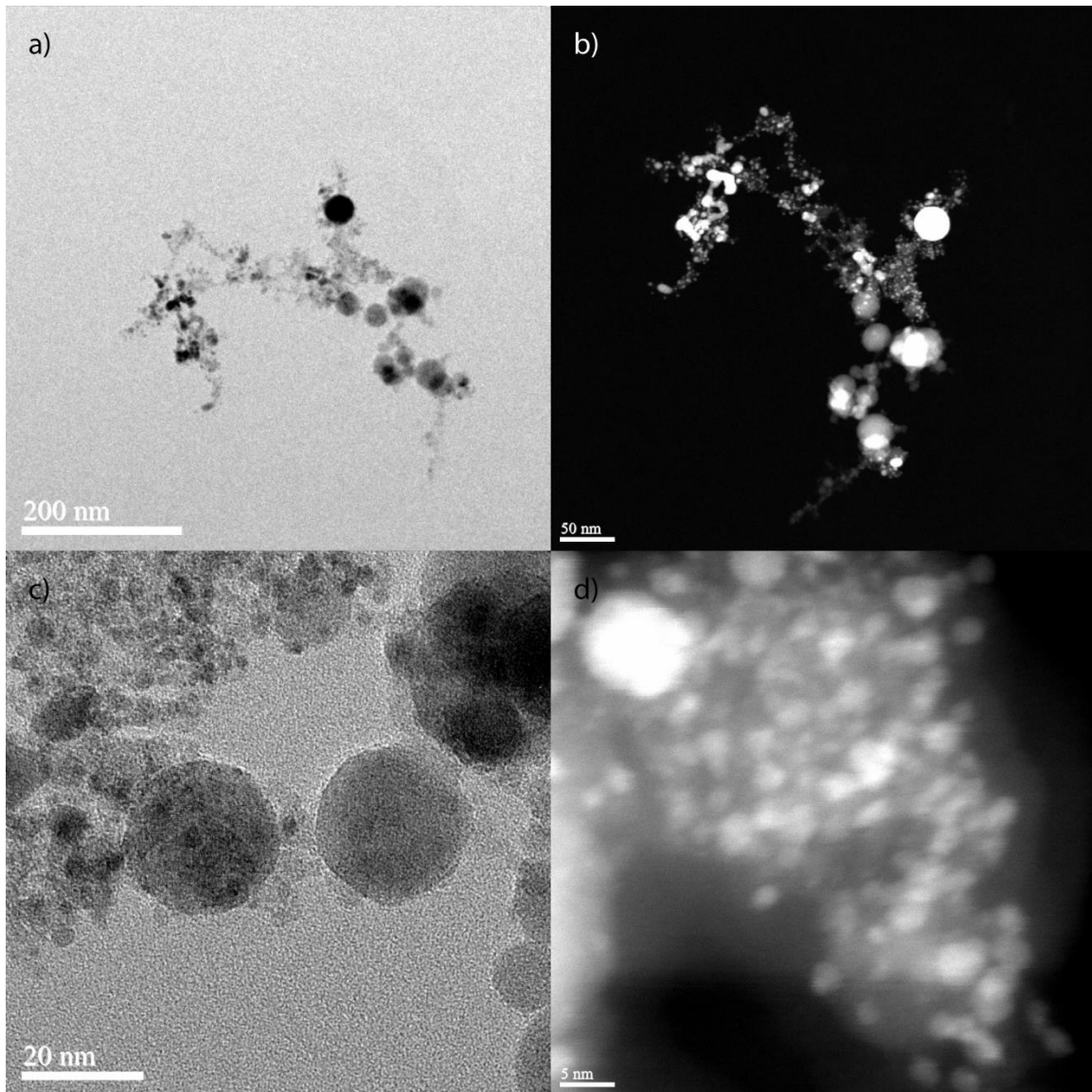


Figure 4.1: Agglomerated chains of amorphous TiO<sub>2</sub> decorated with Ag NPs. This Ag-on-TiO<sub>2</sub> NP chain is shown in: a) bright field TEM, b) high angle annular dark field (HAADF) STEM, c) a higher magnification bright field TEM, and d) a higher magnification HAADF STEM image showing a high density of small isolated Ag NPs on the surface of amorphous TiO<sub>2</sub>.

## Temperature Stability of Ag-on-TiO<sub>2</sub> NPs

Studies that utilized *ex situ* and *in situ* heating of Ag NPs and Ag-on-TiO<sub>2</sub> NPs were conducted to study and compare their temperature stability. It has been shown that metal NPs bound to oxygen vacancies on TiO<sub>2</sub> substrates resist coarsening to a much higher temperature than Ag NPs on free surfaces [7, 10, 50]. Thus, by observing the effects of heating Ag-on-TiO<sub>2</sub> NPs in an oxygen-free environment to those heated in an oxidizing environment of air, it should be evident if LAMA-produced Ag NPs on TiO<sub>2</sub> resist sintering and if there is an effect of oxidizing the oxygen vacancies of the TiO<sub>2</sub>.

The methods described in Chapter 3 to produce Ag NPs and Ag-on-TiO<sub>2</sub> NPs were used. Ag NPs were produced using a single-chamber ablation process and the Ag-on-TiO<sub>2</sub> NPs were produced using a two-chamber ablation process.

### EX SITU HEATING EXPERIMENTS

For the first study, Ag and Ag-on-TiO<sub>2</sub> NPs were collected on Au TEM grids (Pelco 500 mesh, Ted Pella Inc., Redding, CA) with no carbonaceous support substrate using the diffusion process shown in Fig. 2.14. A grid of each, Ag and Ag-on-TiO<sub>2</sub>, were heated in a tube furnace to 500° C in an environment of flowing argon and a set of each was also heated in a tube furnace to 500° C with the tube open to the air. A third set was not heated and was used as a control. After the heating experiments were conducted, the particles collected on the surfaces of the Au wires that made up the grids were studied using HR-TEM.

Compositions of metal-on-oxide particles are typically confirmed using energy dispersive x-ray spectroscopy (EDS), but it is not a useful tool for these samples since all of the particles that could be observed were on the surfaces of the Au TEM grids. Because the grids without carbon supports are made with thicker grids with those made with carbon

supports, and because the NPs have a small cross-section relative to the Au wires, there is a large signal from the Au that overwhelms the signal from the Ag NPs and makes it very challenging to measure the Ag signal. Thus, we did not attempt to use EDS to confirm the presence of Ag. EDS was used to reveal the Ti peaks that were present in the samples, because the Ti signal is present in greater quantities than the Ag and thus the signal was detectable. To confirm the presence of Ag on the particles, high resolution TEM images were taken of the samples and the lattice fringe spacing was measured and compared to known data, as described in the Chapter 2.

### **Ag Nanoparticles**

Fig. 4.2 shows are a few typical Ag NPs prior to heating. Only particles around 10 nm and above were observed in the TEM. Previous research has shown that the LAMA process produces particles smaller than this [21], but, they were either not located on the edge of the grids, or were not collected at all. Since the particles on the edge should contain a random distribution of sizes, it follows that NPs smaller than 10 nm were not collected. This could be because the smaller NPs stayed in the stream lines of the aerosol flow and did not settle on to the grids. Lattice spacing on a few of the areas, shown in Fig. 4.2, were measured and found to correspond to the  $\{111\}$  planes of Ag, as expected. The typical Ag NPs collected are polycrystalline and approximately 10 nm in diameter.

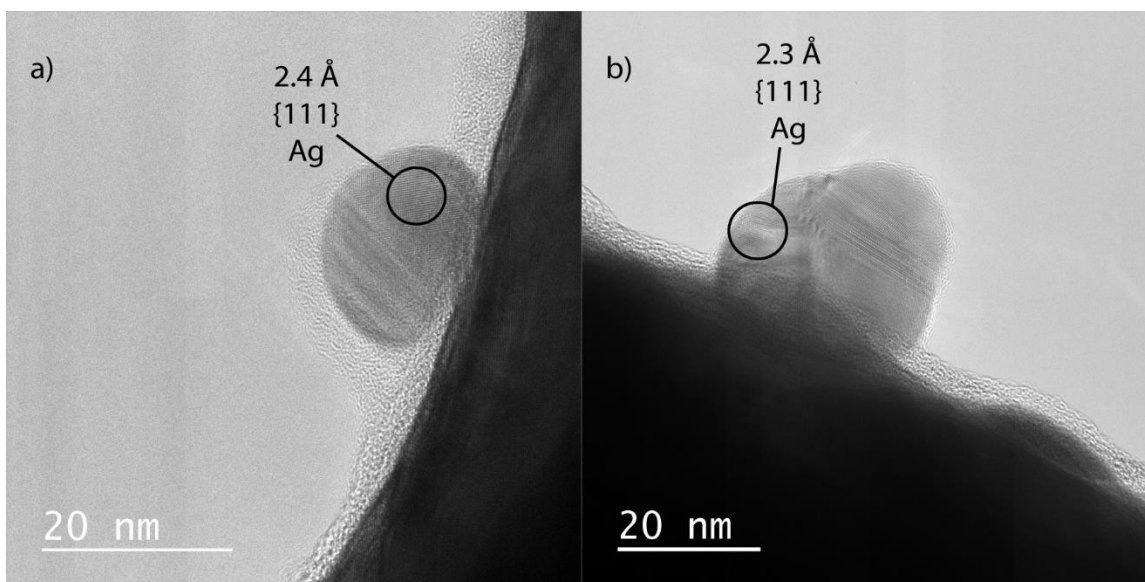


Figure 4.2: Ag NPs produced by a single-chamber LAMA process and collected using diffusion on to Au TEM grids with no carbonaceous support. The particles are polycrystalline and around 10 nm in diameter with some amorphous carbon contamination on the surface

Shown in Fig. 4.3, are Ag NPs heated to 500° C in flowing Ar for 1 hour and allowed to cool. The presence of Ag was confirmed by measuring the {111} lattice spacing in regions of the image where there were no overlapping particles or grains. By comparing both the sizes and the morphologies of these NPs to the as deposited NPs, it is clear that these particles have sintered into larger NPs than the Ag NPs that have not been heated and the twins that were present in the as-deposited particles have annealed out. There is also less amorphous carbon contamination on the surface than the Ag NPs that have not been heated (Fig. 4.2), since some carbonaceous materials likely has sublimated at this temperature.

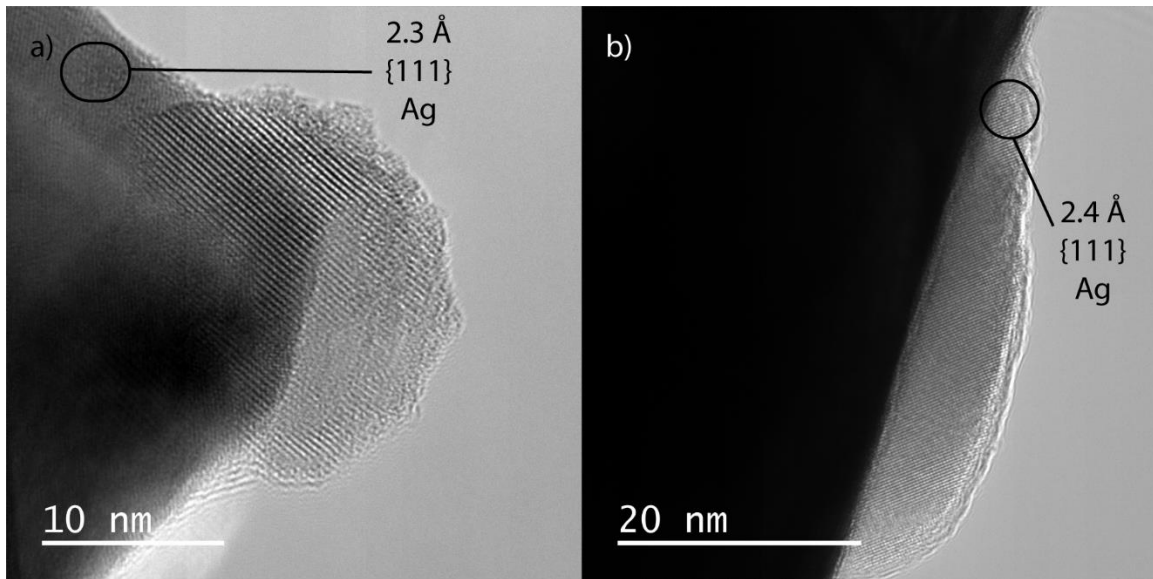


Figure 4.3: Ag NPs produced by the single-chamber LAMA process and collected using diffusion on to Au TEM grids with no carbonaceous support. The grid was then heated to 500° C in flowing Ar for 1 hour and then allowed to cool. The particles have sintered into larger polycrystalline particles.

Ag NPs heated to 500° C in air for 1 hour are shown in Fig. 4.4. Like the NPs that were heated in argon, these NPs also have sintered into larger polycrystalline particles than the Ag NPs that have not been heated. The microstructure is essentially the same as the NPs heated in Ar, with larger polycrystalline particles than the Ag NPs that were not heated.

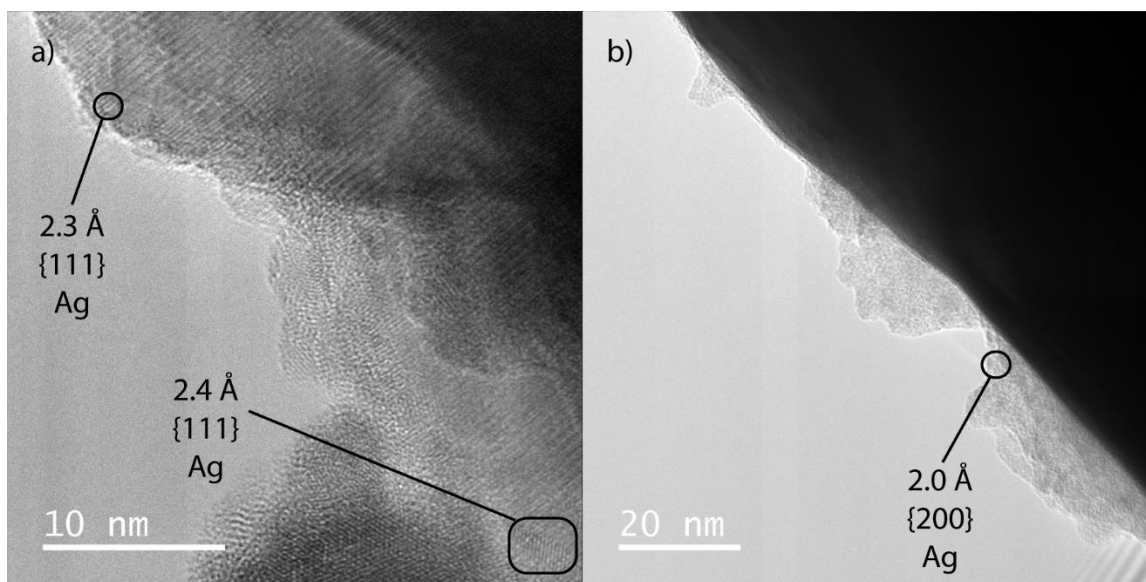


Figure 4.4: Ag NPs produced by a single-chamber LAMA process and collected using diffusion on to Au TEM grids with no carbonaceous support. The grid was then heated to 500° C in open air for 1 hour. The particles have sintered into larger polycrystalline particles.

### Ag-on-TiO<sub>2</sub> Nanoparticles

Shown in Fig. 4.5 are as-produced Ag-on-TiO<sub>2</sub> NPs that have not been heated. Crystalline regions of Ag can be seen on the amorphous TiO<sub>2</sub> support. Again, it was confirmed by analyzing the lattice parameters that these lattice fringes are associated with Ag and not with TiO<sub>2</sub>. Typically, the Ag regions are shown to have a circular shape when isolated and clear contrast can be observed. Since TEM images represent the projection of a three-dimensional shape onto a plane, a circular shape in a TEM micrograph likely corresponds to spherical or semi-spherical Ag NPs of diameter 2 - 10 nm.

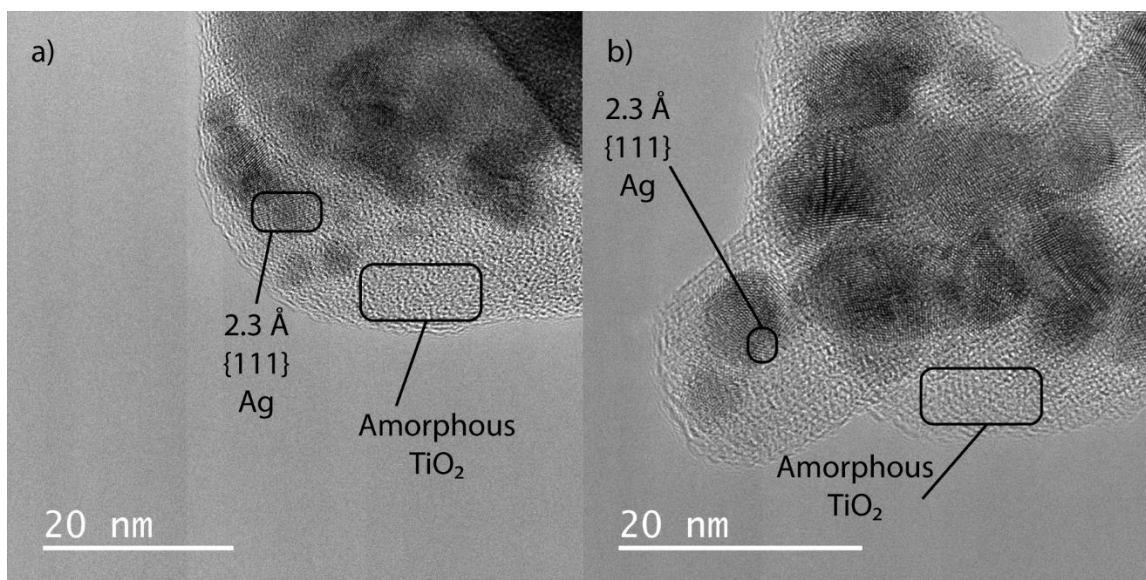


Figure 4.5: Representative images of as-deposited Ag-on-TiO<sub>2</sub> NPs produced by the two-chamber LAMA process and collected using diffusion on to Au TEM grids with no carbonaceous support. The darker regions with lattice fringe corresponds to Ag NPs, as confirmed by analyzing the lattice parameters.

Shown in Fig. 4.6, are Ag-on-TiO<sub>2</sub> NPs that have been heated to 500° C in flowing Ar for 1 hour then allowed to cool. In Fig. 4.6a, regions of Ag are visible on the surfaces of the agglomerates of TiO<sub>2</sub>. The Ag NPs shown in Fig. 4.6b appear to be similar in shape and size to those that were observed prior to heating.

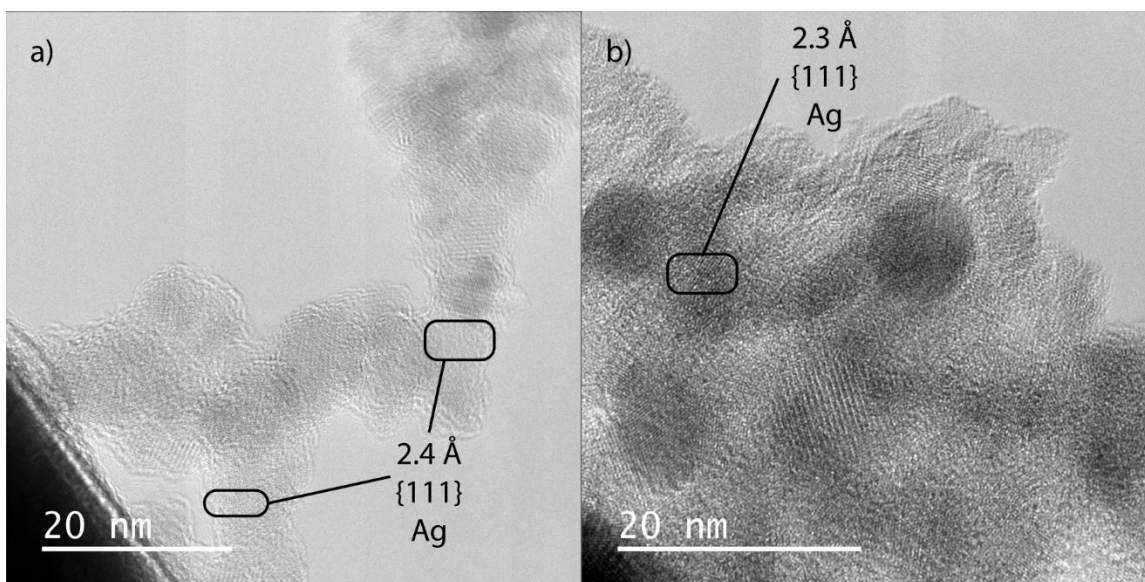


Figure 4.6: Ag-on-TiO<sub>2</sub> NPs produced by the two-chamber LAMA process and collected using diffusion on to Au TEM grids with no carbonaceous support. The grid was then heated to 500° C in flowing Ar for 1 hour and then allowed to cool.

In Fig. 4.7, TEM micrographs are shown of Ag-on-TiO<sub>2</sub> NPs that have been heated to 500° C in air. A 10 nm Ag NP, shown in Fig. 4.6b, was identified, but this was not typical. Most regions analyzed using lattice fringe measurements showed 20-50 nm crystalline TiO<sub>2</sub> with either the anatase (Fig. 4.6a) and/or rutile crystal structure (Fig. 4.6d), but there is otherwise little evidence of Ag following heating.

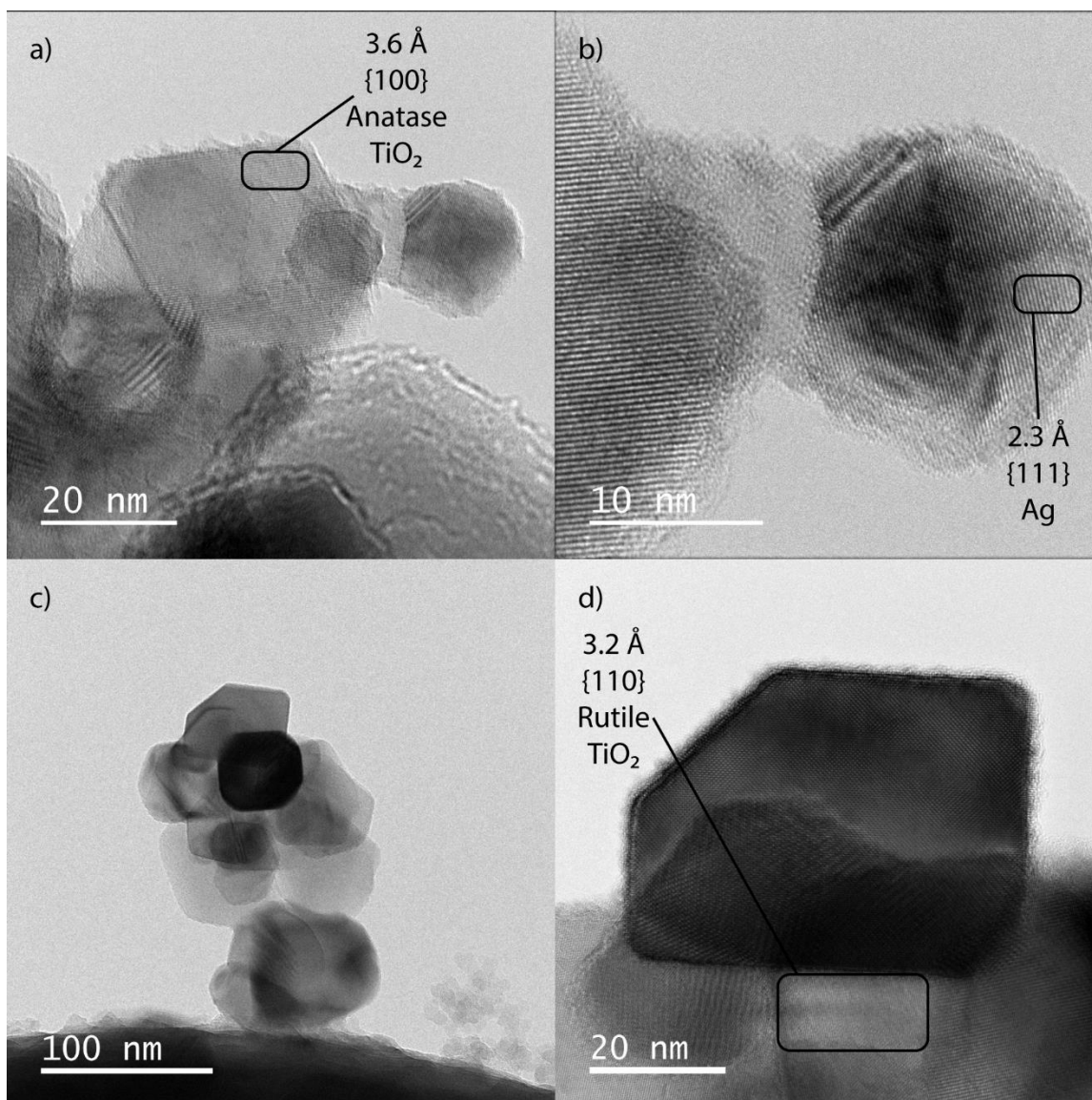


Figure 4.7: Ag-on-TiO<sub>2</sub> NPs produced by the two-chamber LAMA process and collected using diffusion on to Au TEM grids with no carbonaceous support. The grid was then heated to 500° C in open air for 1 hour. Shown in a) is an anatase crystal with a small region of amorphous TiO<sub>2</sub> attached to a 10 nm Ag NP, b) a higher magnification of the Ag NP, c) a 100 nm agglomerate of crystalline TiO<sub>2</sub>, and d) a lower magnification of a crystallite showing lattice fringe spacing that corresponds to the rutile structure of TiO<sub>2</sub>.

## ***IN SITU* HEATING TEM**

Previously, the sintering of Au NPs and Au-on-TiO<sub>2</sub> NPs have been studied *in situ* in a TEM [51]. In this study, the beam of the TEM was focused onto Au and Au-on-TiO<sub>2</sub> NPs. An estimate of the heating was obtained from a model, and the results showed a strong dependence of NP size to the rate of sintering. The free Au particles necked and sintered very easily when heated, but when supported on amorphous TiO<sub>2</sub> some of the Au NPs resisted sintering. Since this study was conducted on Au NPs and there was no direct measurement of the temperature, a new study on Ag-on-TiO<sub>2</sub> NPs was conducted here in hopes of confirming a similar finding for Ag NPs, but using Arduro Protochips system so that temperature could be measured.

This second study, consisted of collecting Ag-on-TiO<sub>2</sub> NPs on Arduro Protochips® grids and then observing changes in morphology *in situ* during heating in a TEM. The Arduro Protochips holder allowed the samples to be rapidly heated in 50 °C increments and then held at this temperature for observation; micrographs were taken at each increment in temperature. Due to the irreversible nature of the effects of heating, only one region of interest could be studied in detail for each sample.

In Fig. 4.8, a series of micrographs of Ag-on-TiO<sub>2</sub> NPs are shown at different temperatures. Heating of the NPs to 475° C showed no change to the original structure. Surprisingly, even the Ag NPs that are in close contact did not sinter. Further heating of the NPs caused smaller Ag NPs to sublime. As the temperature increased, the larger Ag NPs also sublimated, until there were no Ag NPs left. These results show that, in the absence of oxygen, the Ag-on-TiO<sub>2</sub> NPs exhibit resistance to coarsening to temperatures of at least 475°C.

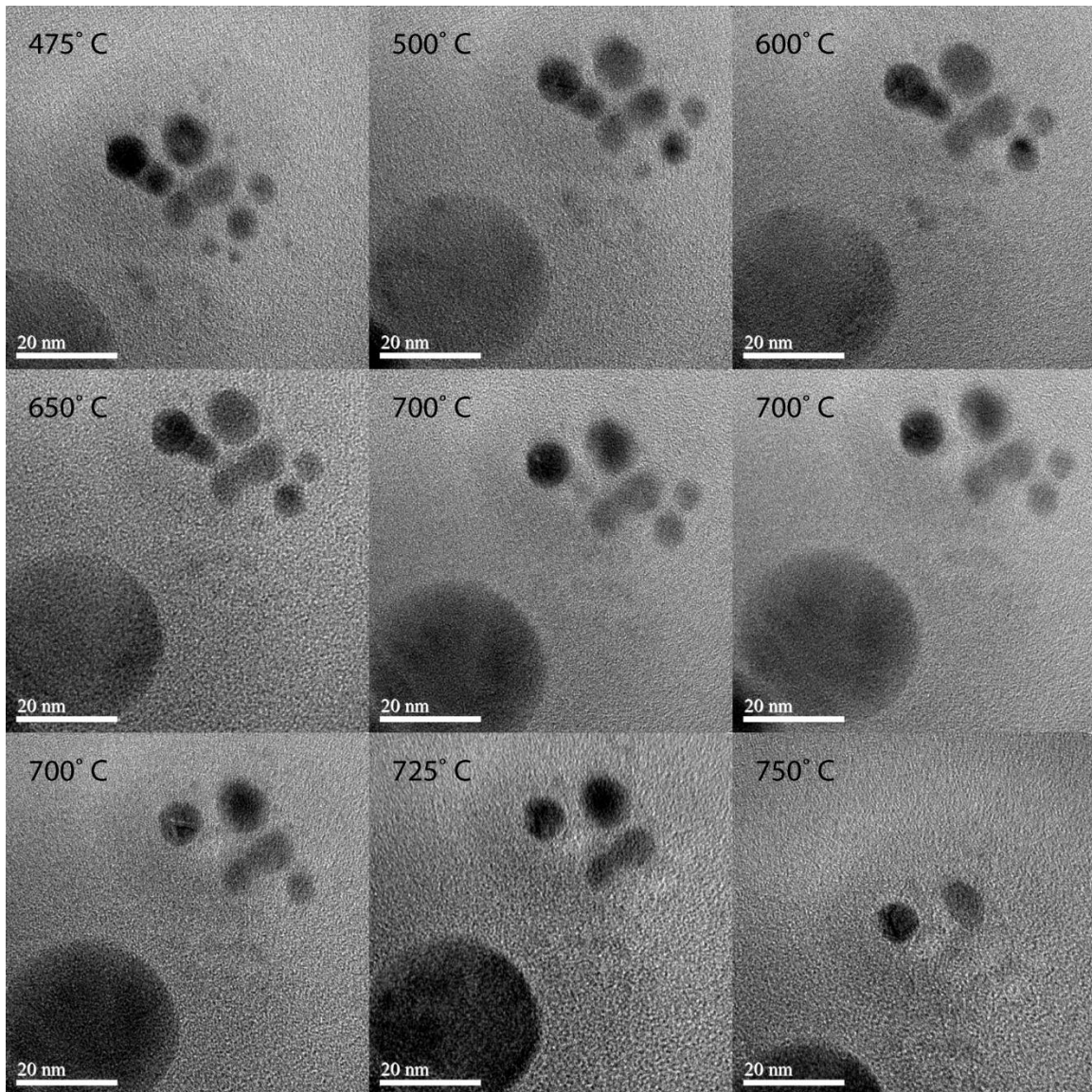


Figure 4.8: Ag-on-TiO<sub>2</sub> NPs produced by the two-chamber LAMA process and collected using diffusion on to Arduro Protochips® grids. Ag-on-TiO<sub>2</sub> NPs were then heated *in situ* in a TEM in 50° C increments and held to take micrographs at each step. The highest temperature with no change is shown in the top left at 475° C, then noticeable changes to the Ag NPs are shown at the corresponding temperatures.

## Discussion

The *ex situ* experiments confirm the hypothesis that Ag NPs produced on the surface of amorphous TiO<sub>2</sub> using the LAMA process do resist sintering to higher temperatures than unsupported Ag NPs. These experiments also confirm that this resistance to sintering is removed when the oxygen vacancies in the TiO<sub>2</sub> are removed by heating in air. This would suggest that the Ag NPs are formed and bound to oxygen vacancies in the amorphous TiO<sub>2</sub>. When these oxygen vacancies are removed by heating the density of the Ag NPs on the TiO<sub>2</sub> is greatly diminished to the point where Ag is difficult to find. Similar pinning effects of oxides on NPs have been previously studied [49, 52]. The only two mechanisms for the Ag NPs to leave the surface of the TiO<sub>2</sub> are sublimation and dissolution into small clusters and migration. To distinguish these two mechanisms, would require the ability to heat and oxidize the TiO<sub>2</sub> *in situ* while observing the samples at a high enough magnification where atoms or small clusters of atoms could be observed (e.g. in an aberration-corrected TEM). Due to limitations in the TEMs available, this experiment could not be conducted. The *in situ* experiments that could be performed, however, show the degree of sintering resistance of these Ag-on-TiO<sub>2</sub> NPs. The Ag NPs were heated to 700° C before they sublimated. If any dissolution of Ag into clusters and migration occurred in this experiment, it could not be observed with the TEM used. These results show that Ag-on-TiO<sub>2</sub> NPs behave in a similar manner as other metal catalyst on oxide supports do [5].

## Conclusions

It has been shown, that Ag NPs will sinter into films when heated to 500° C for 1 hour, regardless of the presence of oxygen. On the other hand, when Ag NPs are on the surface of amorphous TiO<sub>2</sub> NPs they are resistant to sintering. Crystallizing the TiO<sub>2</sub>

support by heating in the presence of oxygen removes oxygen vacancies and allows the Ag NPs to migrate and form films. The fraction of Ag present on the TiO<sub>2</sub> was significantly less relative to the amount seen on the crystalline TiO<sub>2</sub> that had been heated. It has been observed that Ag NPs will sublime at temperatures below 500° C and it would be reasonable to assume the mechanism for Ag depletion was sublimation. Lastly, these results have technological significance because they show that Ag NPs can be used as an active material in a reducing atmosphere process up to 500° C for up to 1 hour, if they are supported on amorphous TiO<sub>2</sub>.

## CHAPTER 5: SiO<sub>2</sub> AND METAL-IN-SiO<sub>2</sub> GLASS FILMS

In this chapter, a process method for producing SiO<sub>2</sub> NP and metal-in-SiO<sub>2</sub> NP films is presented and the transmission spectra and thickness of these films is studied. These films were manufactured by supersonic deposition using parameters that produced the highest NP velocities possible with the current configuration of the LAMA process. Ideally, the films would be impacted at a high enough velocity to create a high film density, and would allow for a heat treatment that produces densification. For this to occur, surface diffusion must be suppressed and grain-boundary diffusion must dominate, otherwise coarsening will be the only result [25]. These were preliminary experiments to study the current capacity for using the LAMA process for producing high density films from oxides.

Firstly, films of SiO<sub>2</sub> with a thickness of 1-2 μm were produced and studied<sup>2</sup> to understand the effect of a low temperature post-deposition annealing treatment on the transmission of visible light through the oxide. The hypothesis is that, if the low temperature annealing densifies the films, then the voids in the film will be reduced in both size and number. These voids in the films cause Rayleigh scattering, which results in a size-dependent decrease in the transmission of light. If these voids grow in size due to coarsening, then the transmission spectra will drop due to an increase in Rayleigh scattering as the void size approaches the wavelength of the light. Thus, by measuring the transmission spectra, the response of the film to annealing can be indirectly determined.

Lastly, films of various metal-in-SiO<sub>2</sub> compositions were produced to study changes in the transmission spectra due to plasmon absorption peaks of the metal NPs embedded in the SiO<sub>2</sub> films. Since the optical transmission of the LAMA-produced films

---

<sup>2</sup>Measurements including UV-Vis spectra and profilometry were performed by Zach Levine from the Department of Mechanical Engineering at the University of Texas at Austin.

has not been optimized yet, it is very likely that a post-deposition heating step will be necessary. These metal-in-SiO<sub>2</sub> NP films were subject to the same heating process as the SiO<sub>2</sub> NP films. If there is connectivity between the metal NPs it is likely that any agglomerates of metal NPs will densify when heated to 400° C. This could cause the plasmon absorption peaks to change because the peak location depends on the particle size and follows well-known trends. Oxidation of some metal NPs is also a concern due to the size of the NPs. Metal oxides typically do not have strong plasmon absorption peaks. Thus, by determining the peak intensity and location of the plasmon peaks, the influence of film annealing on the size and oxidation state of the metal NPs present in the films can be indirectly probed.

### **SiO<sub>2</sub> Films**

The single chamber ablation process with a 1 mm deposition nozzle was used to make SiO<sub>2</sub> films and the UV-Vis transmission spectra are shown as thin lines in Fig. 5.1. Also shown as thick lines are the corresponding UV-Vis transmission spectra after heating the films to 400° C and holding for 1 hour. The transmission spectra for the bare glass that was used as a substrate are also shown for reference before and after heating. The increase in transmission for the bare glass after heating could possibly arise from annealing of strain left from the manufacture of the glass slides or could simply be a measure of the experiment-to-experiment scatter from each measurement.

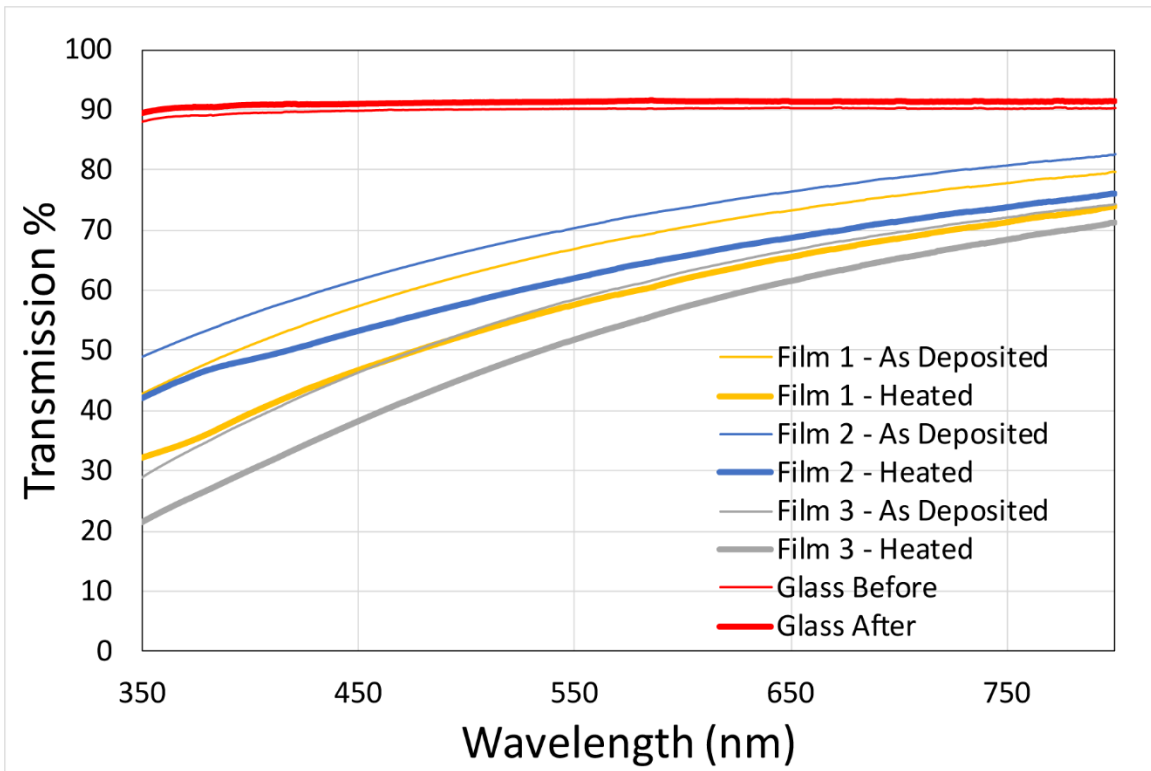


Figure 5.1: UV-Vis transmission spectra of three LAMA SiO<sub>2</sub> NP films and the glass microscope slide used as a substrate.

Film 1 was produced using the highest particle feed rates and also formed the thickest film. Higher feed rates result in higher local aerosol densities in the ablation. It has been previously shown that higher local aerosol densities in the ablation region produce NPs aerosols with a higher concentration of agglomerates, and also produce lower film densities when supersonically impacted [22, 53]. The thickness and standard deviation for film 1 was measured at  $1150 \pm 540$  nm after the heating treatment. The film thickness was unfortunately not measured before heating, and so the degree of densification of this film is not known.

Film 2 was produced using a lower feed rate than film one. The feed rate was reduced by increasing the amount of gas that bypasses the powder feeder. This was done

to reduce the degree of agglomeration in the NP aerosol and therefore in the film. The thicknesses and standard deviations was measured using optical profilometry to be  $1140 \pm 380$  nm and  $1090 \pm 400$  nm, before and after heating respectively.

Film three was produced by lowering the feed rate further than both of the previous films. This film had the more uniform appearance upon visual inspection. The thicknesses and standard deviations were measured as  $1700 \pm 510$  nm and  $1610 \pm 440$  nm, before and after heating respectively.

Figure 5.2 shows the change in film UV-Vis transmission after heating to  $400^\circ$  C for 1 hour. All three films showed a decrease in transmission, shown in Table 5.1 broken out by wavelength ranges. The data shows a wavelength dependence on the change in transmission after heating. This can be explained by the Rayleigh scattering of the voids in the films. As-deposited films produce voids on the order of the deposited NPs. These voids can be well connected for low density films or less so for higher density films. If the starting density of the films 1, 2, and 3 were low enough that surface diffusion dominated, then coarsening would have occurred and well connected voids would have grown in size. Since Rayleigh scattering intensity is size-dependent on the scatterer and wavelength dependent for the incident light, this is consistent with the data in Fig. 5.2. Such a trend would be expected for a film with voids that grow larger than the starting NP size, since the most scattering happens from 350 - 450 nm and Rayleigh scattering dominates for scatterers smaller than  $\frac{1}{4}$  wavelength of the light.

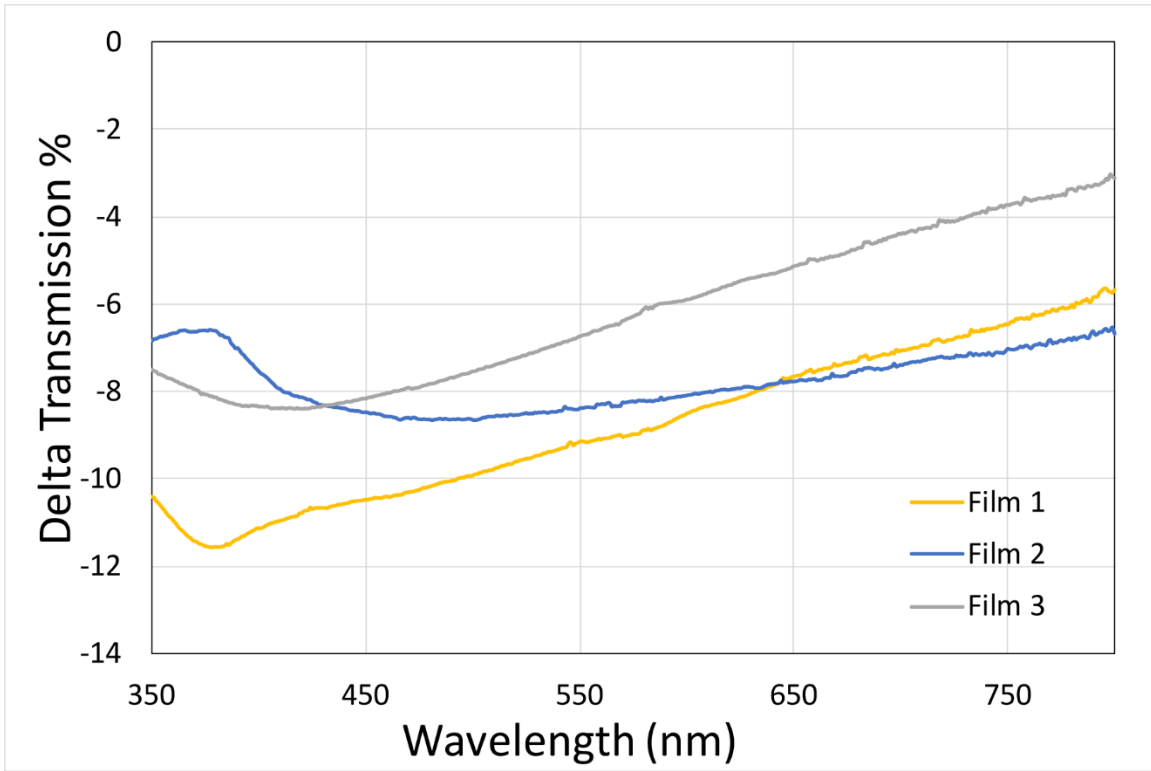


Figure 5.2: Graph of the change in UV-Vis transmission spectra upon heating for three LAMA-produced SiO<sub>2</sub> NP films.

Avg. Delta Trans. %	450-550 nm	550-650nm	650-750 nm	450-750 nm
<b>Film 1</b>	-9.9	-8.5	-7.1	-8.5
<b>Film 2</b>	-8.5	-8.1	-7.4	-8.0
<b>Film 3</b>	-7.5	-5.9	-4.4	-5.9

Table 5.1: Average change in UV-Vis transmission upon heating for three LAMA-produced SiO<sub>2</sub> films for several wavelength ranges.

It was the original intention to determine the volume change of the films after the heating process by measuring the height profiles of the films at random areas of the film before and after heating. The films height profiles were not uniform across the films due to the variability of the aerosol feeder. The standard deviation in the film height is much

too large to be used to determine a change in volume, especially since registration of the measurement locations is not possible, which makes it impossible to measure the same region of the film before and after post-deposition heating. The average heights of the films two and three did show ~5% reduction in height, but the standard deviation of the measurements varied from 28-45% and thus the measurements of densification from volume changes are not conclusive.

### **Metal-in-SiO<sub>2</sub>**

Three films were produced using a single-chambered ablation process to simultaneously ablate metal and glass. This was done by mixing the feedstock powders. This process is challenging, because the powders feed at different rates, and thus mixing the desired loading ratio of the feedstock microparticles in the feeder does not necessarily produce the same ratio of NPs in the films so the degree of control of the composition of the films is limited using this approach. The films were deposited using the same process as the previous SiO<sub>2</sub> films. The UV-Vis transmission spectra of these films were also measured before and after the same post-deposition heating used for the SiO<sub>2</sub> films.

Figure 5.3 shows that the plasmon absorption peak is located at 459 nm for as-deposited Ag-in-SiO<sub>2</sub>. After heating, the local minimum in the transmission spectra associated with the plasmon absorption peak increases in transmission. Since oxidation of Ag NPs was not observed in the heating experiments conducted for the Ag-on-TiO<sub>2</sub> NPs in Chapter 4, it is not likely that oxidation is occurring here, especially since the annealing treatment for these films was conducted at a lower temperature than for the experiment conducted in Chapter 4. The change in plasmon absorption peak intensity is likely due to a change in morphology of the Ag NPs. At 400° C there exists enough driving force to sinter any agglomerates of the Ag NPs produced in this process. Without studying the

microstructure of the films using a direct but time consuming method such as TEM, it is not possible to conclude anything more detailed about the nature of the Ag metal particles.

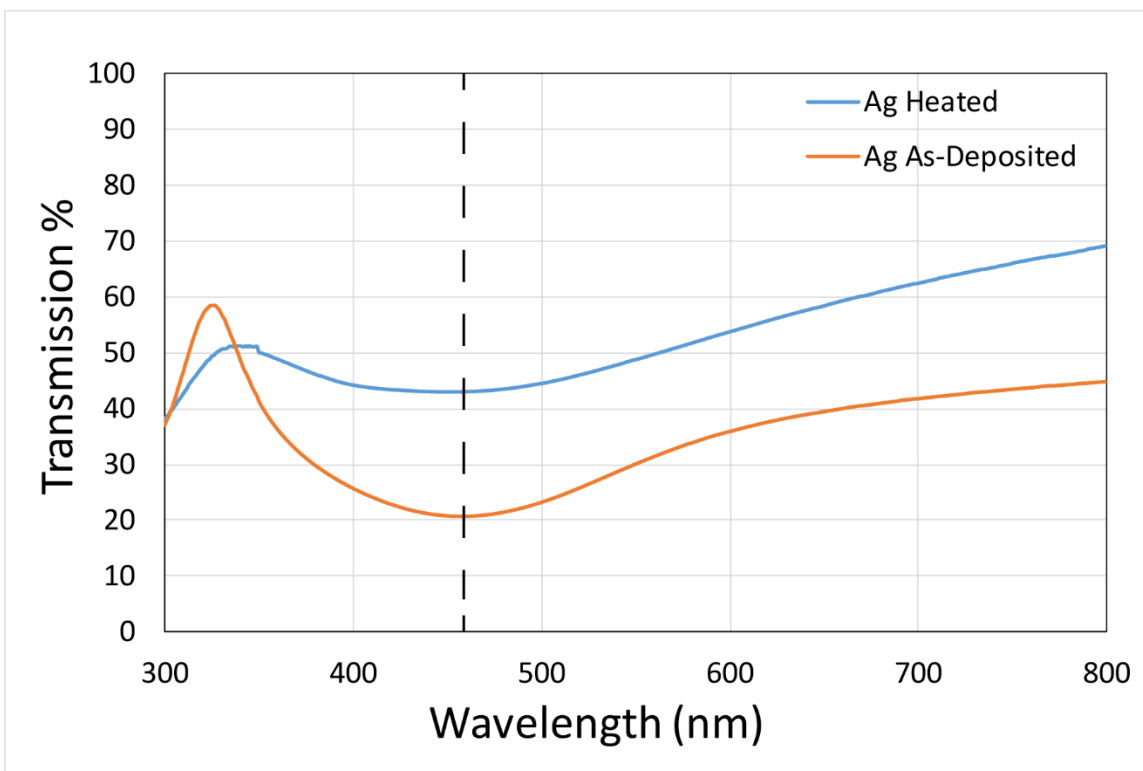


Figure 5.3: Transmission spectra of Ag-in-SiO<sub>2</sub> NP film before and after heating to 400° C for 1 hour.

Figure 5.4 shows that the plasmon absorption peak for Au-in-SiO<sub>2</sub> is located at 533 nm. After heating, the local minimum in the transmission spectra associated with the plasmon absorption peak increases in transmission. Since oxidation of Au NPs was not observed in the heating experiments conducted for the Au-on-TiO<sub>2</sub> NPs, it would follow that oxidation does not likely occur at this lower temperature heating. Just like the Ag-in-SiO<sub>2</sub> film, the change in plasmon absorption peak intensity is likely due to a change in

morphology of the Au NPs and we can conclude that, at 400° C there exists enough driving force to sinter any agglomerates of the Au NPs produced in this process.

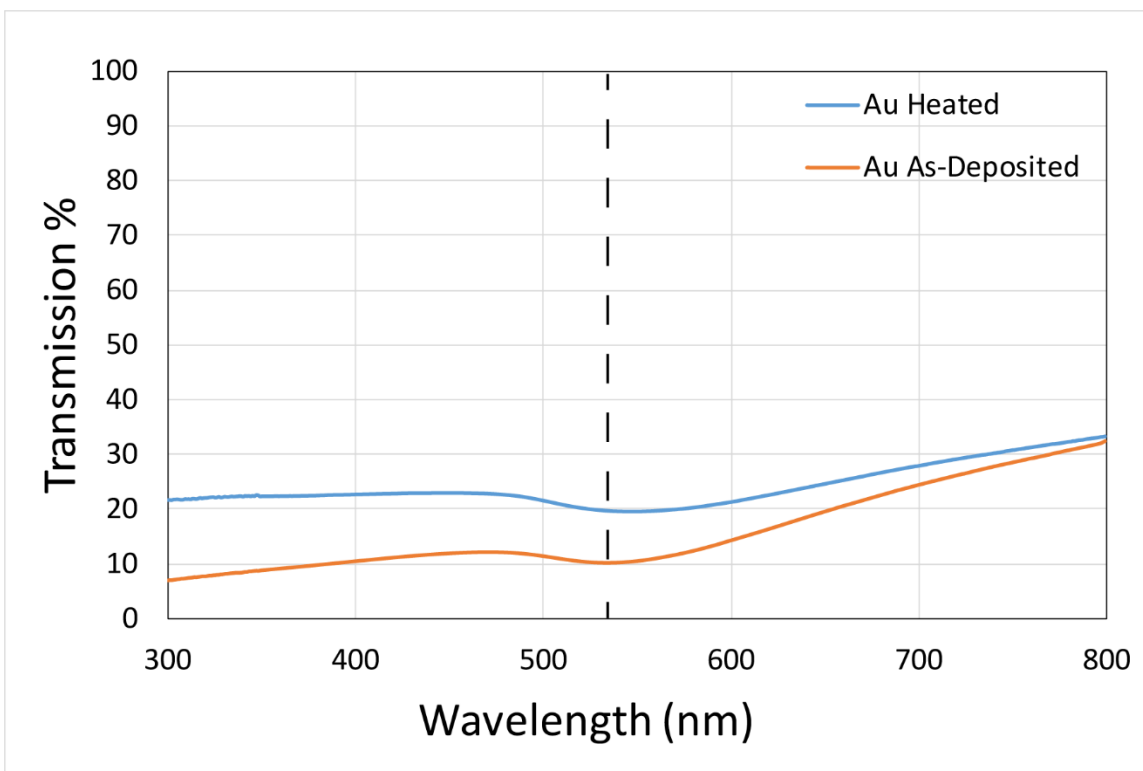


Figure 5.4: Transmission spectra of Au-in-SiO<sub>2</sub> NP film before and after heating to 400° C for 1 hour.

Figure 5.5 shows that the plasmon absorption peak for Cu-in-SiO<sub>2</sub> is located at 627 nm. After heating, the local minimum in the transmission spectra associated with the plasmon absorption peak is no longer visible. This data can be explained when oxidation of Cu NPs is considered. Previous Cu NPs produced by LAMA oxidize when exposed to air [22, 54]. Embedding Cu NPs in SiO<sub>2</sub> films appears to suppress complete oxidation at room temperature, but once the films are heated, it appears that oxidation of the Cu NPs does occur.

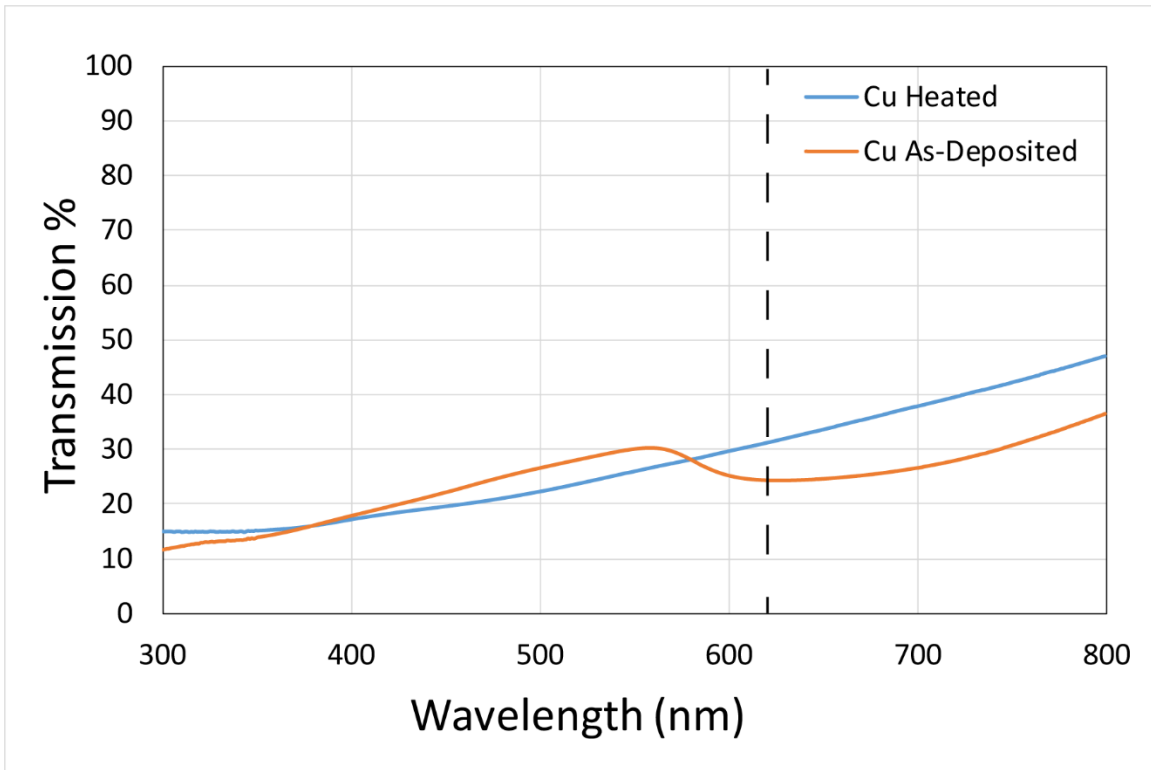


Figure 5.5: Transmission spectra of Cu-in-SiO<sub>2</sub> NP film before and after heating to 400° C for 1 hour.

The transmission spectra shown in Fig. 5.3 - 5.5 for the metal-particle embedded SiO<sub>2</sub> films generally show an increase in the transmission spectra upon heating at wavelengths away from the plasmon resonance, in contrast to the pure SiO<sub>2</sub> films which shows a decrease. The increase in transmission for the films containing the metals is consistent with the observed small decrease in films thickness and both suggest that the films may be densifying upon heating. However, the degree of densification measured from the change in film thickness is small, and these results are not consistent with the observed transmission spectra for the pure SiO<sub>2</sub> films. As suggested earlier, the transmission spectra are sensitive not only to the fraction of scatters, but also their size. In

addition, the index of refraction of the films also depends on the void fraction. Since there are multiple interfaces present in these films, the differences in the transmission spectra are also likely affected by changes to the index of refraction of the films that occur upon heating. In summary, although these experiments have demonstrated the capability of LAMA for producing metal-particle embedded films, resolving the complexity of these spectra would require further analysis that is beyond the scope of this study.

## **Conclusions**

The UV-Vis transmission spectra decrease when as-deposited SiO<sub>2</sub> films are subjected to a low temperature annealing, suggesting that coarsening due to surface diffusion is the dominant mass transfer mechanism at this temperature and film density. It is possible that higher film densities or higher temperatures could result in a transition in dominant mass transfer mechanisms to grain boundary diffusion, which would result in densification, as has been observed in Ag [25]. Further experimentation would be required to establish this, however. The wavelength dependence of the change in UV-Vis transmission after heating corresponds to the wavelength dependence of Rayleigh scattering of subwavelength scatterers, which suggest that the growth of voids in the film coarsen during the heat treatment.

It is evident from the UV-Vis transmission spectra of LAMA-produced metal-in-SiO<sub>2</sub> NP films that a plasmon absorption peak exist for the Ag, Au, and Cu films. However, the decrease in plasmon absorption peak intensities after heating suggest that film deposition techniques and post-deposition heating must improve to maintain the as-deposited plasmonic properties. Ongoing experiments in our research group are aimed at increasing the deposition velocity further, which would be beneficial for potentially realizing high quality plasmonic films with tunable resonances.

## CHAPTER 6: CONCLUSIONS AND FUTURE WORK

The development of a NP-facilitated transport membranes for the separation of ethylene from ethane hinges on the ability to find NPs with the optimal binding energy to ethylene. The binding energy to Ag is the lowest of metals and metal alloys that have been studied to date. However, the predicted optimum binding energy is even lower than that to Ag. In this dissertation, the binding energy of ethylene to Au<sub>0.35</sub>/Cu<sub>0.65</sub> NPs was studied using DFT modeling and SERS measurements, and it was found that this alloy exhibited a similarly low binding energy as Ag NPs. Even more notable, Au<sub>0.35</sub>/Cu<sub>0.65</sub> NPs were found to have a lower binding energy to ethylene than either Au NPs or Cu NPs. This is remarkable because alloys studied to date exhibit a binding energy with ethylene between that for the end-member, pure metals. This result was rationalized by showing that Au segregates to the surface of Au<sub>0.35</sub>/Cu<sub>0.65</sub> NPs and this monolayer of Au on Au/Cu alloy has a different binding to ethylene than pure Au. Taken together, these results suggest a viable methodology for the discovery of alloy particles that have even lower binding energies to ethylene than Ag through a combination of DFT calculations and experiments. Thus, it may be possible to achieve the optimal binding energy for facilitated transport.

When Ag NPs are present on the surface of amorphous TiO<sub>2</sub>, it was shown that the Ag NPs do not sinter when heated to 500° C. This is in contrast to unsupported Ag NPs, which coarsened rapidly and even formed films when heated to 500° C. The coarsening resistance of oxide-supported Ag was attributed to pinning of the Ag NPs to the defect sites on the surface of the amorphous TiO<sub>2</sub>. Crystallizing the TiO<sub>2</sub> NPs and removing oxygen vacancies by heating to 500° C caused Ag NPs on their surface to become unpinned. When unpinned, the Ag became highly mobile and lost its sintering

resistance. These findings suggest that it should be possible to use Ag NPs as an active material in a reducing atmosphere up to 500° C provided that the oxide does not crystallize, which is rather remarkable.

In Chapter 6 it was shown that the optical transmission of as-deposited SiO<sub>2</sub> films produced by LAMA exhibited significant loss due to scattering from defects. It was also shown that the optical transmission in the visible spectrum is decreased by ~6 - 9% after low temperature sintering of SiO<sub>2</sub> films at 400°C for 1 hour. It was determined that coarsening of the films caused an increase in the size of the voids in the films. These larger voids exhibited increased Rayleigh scattering of the incident light and reduced the optical transmission. This finding is significant because although the current LAMA process does not provide sufficient impaction velocity for SiO<sub>2</sub> to enable low temperature sintering, future improvements may allow films to be produced that are sinterable. To demonstrate the feasibility of producing plasmonic films using LAMA, metal particles were embedded into SiO<sub>2</sub> films during deposition, and the transmission spectra were subsequently measured. For the metals that were studied, the plasmon absorption local minimums decreased by 10-25% after heating. The plasmon absorption peak was not present for Cu after heat treatment was performed, as expected, because Cu oxidizes readily in an oxidizing atmosphere at elevated temperatures. Although this work was limited to pure metal particles, it demonstrates a potential manufacturing route for producing plasmonic films from non-equilibrium alloys that would allow tuning of the resonance through compositional control.

## **Future Work**

There are two major directions for future work that are suggested below. The first direction is to continue research using the two-chambered double ablation process to produce alloy NPs-on-TiO<sub>2</sub>. For this direction there are several engineering improvements for two-chambered ablation that would improve the process. There are also many more research opportunities for alloy and non-equilibrium alloy development to be explored.

The second direction presented below is the continued research into metal-in-SiO<sub>2</sub> optical films. This direction has the opportunities for studying multi-component aerosol modeling, (metal, alloy, and non-equilibrium alloy) plasmonic effects, and supersonic deposition engineering improvements.

Both of these directions share one area of research that must be explored: devising a method for producing alloy feedstock MPs with the characteristics needed for LAMA. Many alloy compositions that would be promising cannot be purchased in powders in the sizes or compositions needed for LAMA. One proposed method of synthesis is to start by synthesizing or purchasing a powder that will serve as a core particle and seed to chemically grow a shell consisting of a second metal. For example, Pt could be precipitated on the surface of Au. With our current understanding of the LAMA process, we expect the two metals in this core/shell should mix in the ablation plume and produce alloy NPs.

### **ALLOY NP-ON-TiO<sub>2</sub>**

For the proposed future work, many improvements to the double ablation process would be needed. Currently, the two-chamber process uses a very long tube to bring the

ablated TiO<sub>2</sub> to the second ablation setup. This long path allows enough time for the TiO<sub>2</sub> NPs to lose any residual charge from the ablation and this causes the NPs to then agglomerate. Even though agglomerated metal NPs still form on the surface of the TiO<sub>2</sub> and may exhibit improved chemical properties and sintering resistance, they are not ideal. The supersonic deposition of these long chain agglomerates that we observed has not been studied by our group. The morphology of the agglomerates is complicated and could result in inconsistency in the ability to control the deposition of films, poor film densities, and difficulty in further densifying the films during post-deposition annealing.

One proposed method of minimizing the agglomeration of the TiO<sub>2</sub> NPs is to reduce the distance of the tubing between the two chambers. This would require that the ablation and deposition cells be moved so that they are very close to each other or possibly built into one two-chambered cell with two sets of windows for the laser paths to pass. The optics for this setup would pass the beam through the first cell, reflect it twice, and also refocus it to the second ablation region, as shown in Fig. 6.1. This setup would not suffer from the same problem as the current double chambered cell, since flow between the two chambers could not occur, as it does now. The second feeder would implement the new design for double ablation that was previously discussed to mix the NPs and MPs.

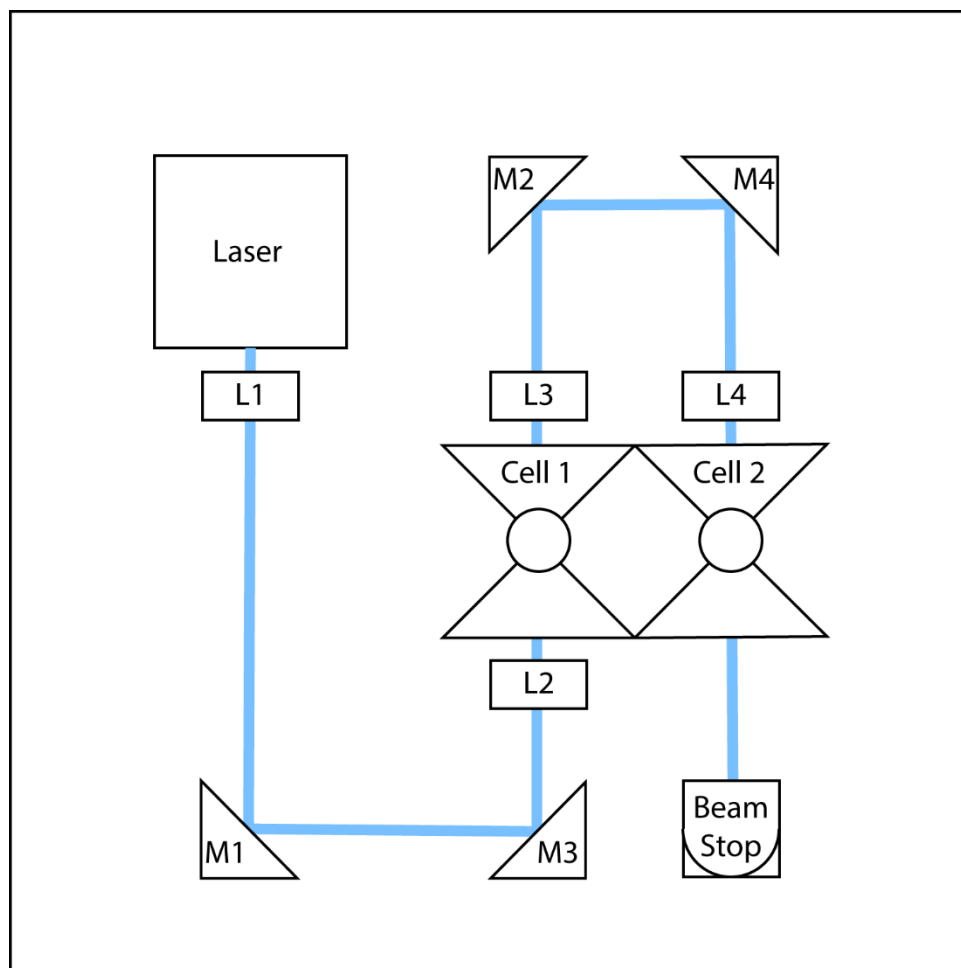


Figure 6.1: Schematic of a proposed LAMA configuration to minimize the distance between the two cells used for producing metal-on-oxide NPs.

### Facilitated Transport Membranes for Ethane/Ethylene Separation

There are still many alloy compositions for NPs that can be explored to find a favorable alloy for use in a facilitated transport membrane for the separation of ethylene from ethane. Since these metal alloy NPs can be produced on  $\text{TiO}_2$  NPs without any change to their respective binding energy with ethylene, these metal-on- $\text{TiO}_2$  NPs could potentially allow for higher operating temperatures of the membrane without microstructural changes to the metal NPs. In addition to making it possible to increase

the selectivity for ethane/ethylene selectivity through alloy design, placing the alloy particles on the oxide was shown to provide enhanced resistance to NP migration, so long as the oxide remains amorphous. Thus, the metal alloy-on-oxide particle concept should also allow very high concentrations of metal alloy to be present in the membrane, without agglomeration of the metal particles. This would increase the performance of the membrane further.

A method of collection of the metal-on-TiO<sub>2</sub> NPs would have to be developed for the two-chambered ablation process that would allow for impregnation of the metal-on-oxide nanostructures into the polymer. Previously, a liquid collection method was developed for the single ablation chamber and it may be possible to adapt this process to double ablation. The manufacturing process and a testing methodology for measuring selectivity of these films was previously developed and is discussed by Kristopher Gleeson in his Ph.D. Dissertation [22].

### **Non-Equilibrium Alloys on a Porous TiO<sub>2</sub> Matrix for Catalysis**

The ability to manufacture large quantities of non-equilibrium alloy NPs is unique to the LAMA process, and future collaborations with other research groups that can test and/or model prospective catalyst NPs should be pursued. Using SERS to measure vibrational modes of analytes then using computational models to relate those modes to binding energy is a circuitous method and has many issues. Direct measurement of a NP films catalytic activity should be a priority for future work in this area.

### **METAL AND ALLOY NP-IN-SiO<sub>2</sub> DENSE FILMS**

The preliminary work presented in this section of the dissertation was an attempt to show that optical quality films could be produced by LAMA. While high quality films were not produced, the feasibility of producing these films was demonstrated. Based on

molecular dynamics modeling, increasing impaction energies/velocities of the SiO<sub>2</sub> NPs beyond the values we currently can produce would lead higher as-deposited film densities, which even if they were not fully dense, would still reduce the temperatures and times required for further densification during a post-deposition annealing treatment. If post-deposition annealing is required, rapid thermal annealing should be conducted to minimize the temperature required for densification, and so that the oxidation of the metal inclusions is minimized. Another task is to investigate methods that could produce a more uniform deposition, like the addition of a feedback control system to control the fluidized bed feeder and upgrading the x-y stage by improving the step precision.

Another important task to ensure repeatability and control of the deposited films, is to model the aerodynamics of the mixed feedstock aerosol. The diameter and density of the feedstock material affects the flow rate through the fluidized bed feeder. If the feeding characteristics of a particular powder is known, then ratios of the powders can be mixed to obtain the proper volume fraction of metal NPs in the SiO<sub>2</sub> films.

Lastly, investigations of non-equilibrium alloy NPs-in-SiO<sub>2</sub> films could open up areas of research previously not accessible. The plasmonic properties of these alloys could be studied by co-depositing a non-equilibrium alloy NPs and SiO<sub>2</sub> into a dense film and measuring the UV-Vis spectra of these films.

# APPENDIX A: STEPPER MOTOR LABVIEW CODE

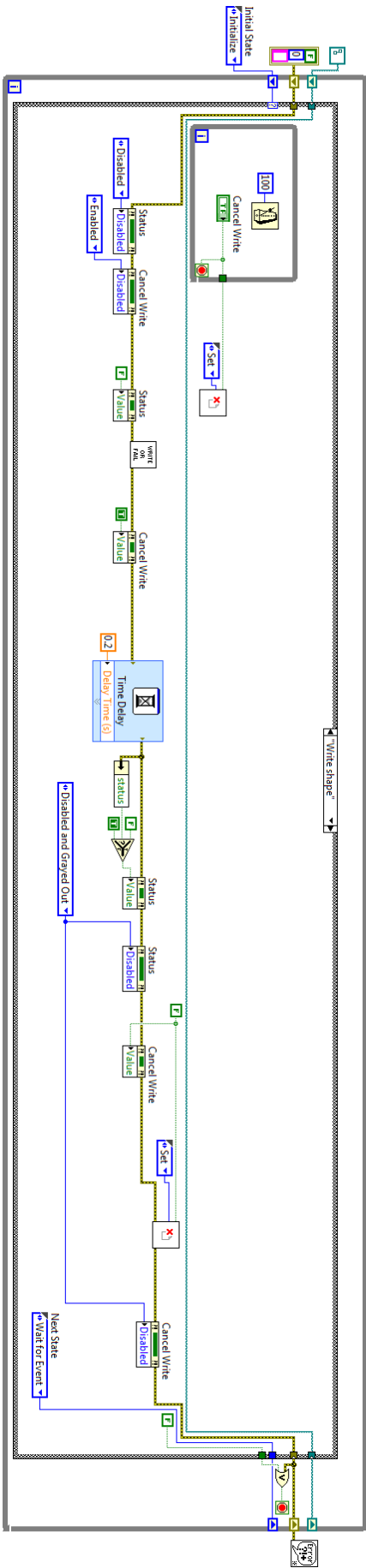
## Front Panel

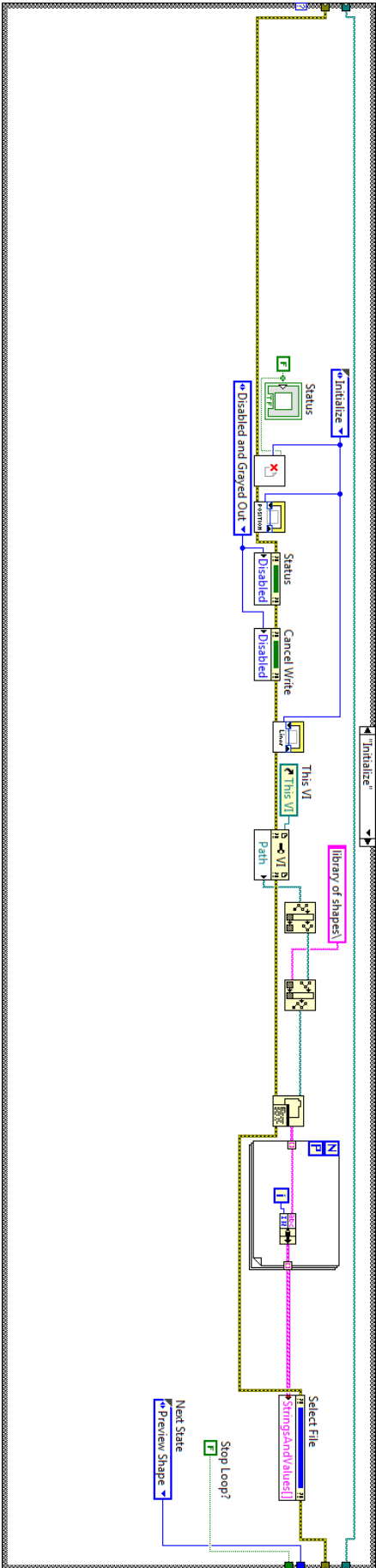
The LabVIEW front panel is divided into two main sections. The top section contains control elements for file operations and motor status. It includes a file path input field set to "East 5000 5000.txt", a "Write Shape" button with a right-pointing triangle, a "Cancel Write" button with a red square, a "Stop" button with a red square, and a "Status" indicator light (currently green). Below these are two digital readout (DRO) displays for "Nozzle Position", both showing "0", and a "Reset Position" button. The bottom section features a large black rectangular area representing the nozzle's path, with "X" and "Y" axes labeled. A small "Outer" button with a blue icon is located at the bottom right of this area. The top section also contains a grid of 20 columns and 10 rows of numeric indicators, all displaying "0".

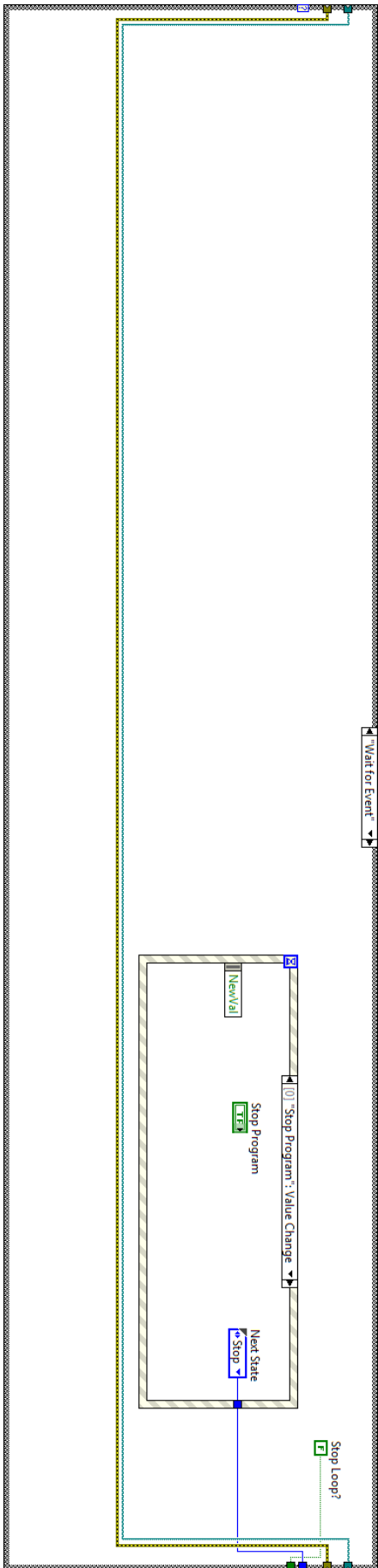
## Controls and Indicators

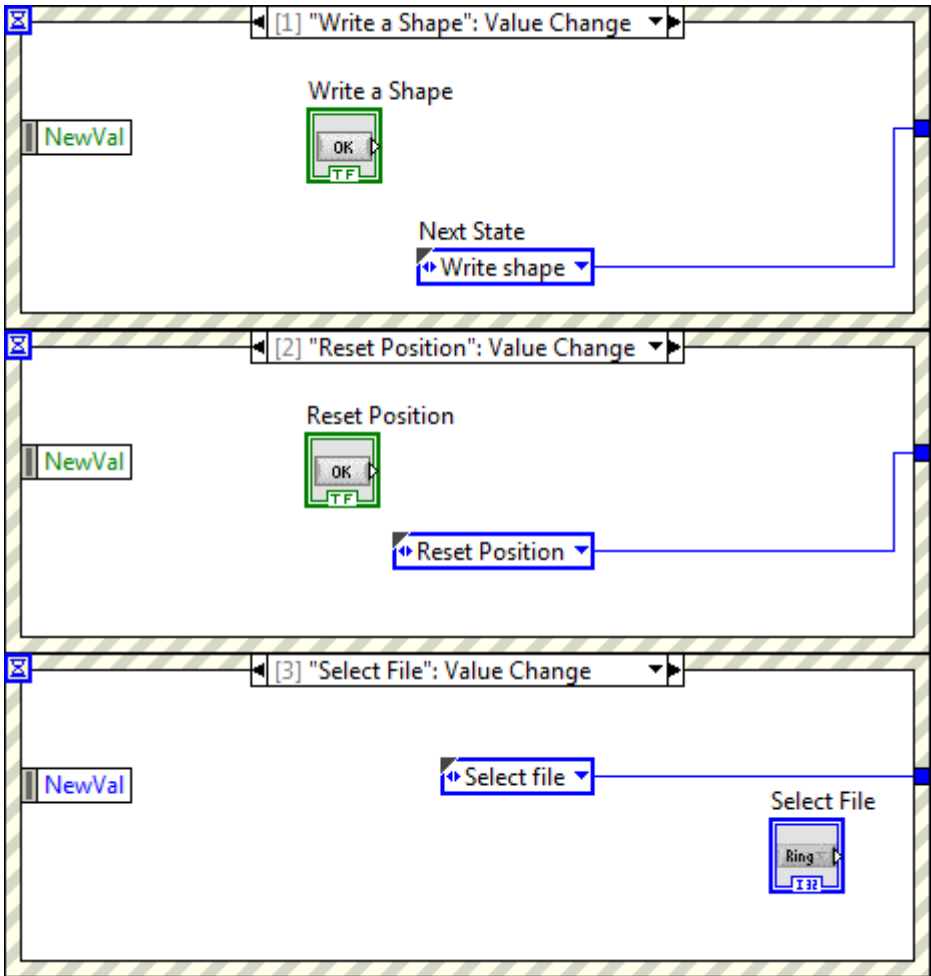
-  Write a Shape
-  Stop Program
-  Select File
-  Reset Position
-  Cancel Write
-  Nozzle Position
  -  element
-  Instructions
  -  element
-  Status
-  Write Preview

## Block Diagram

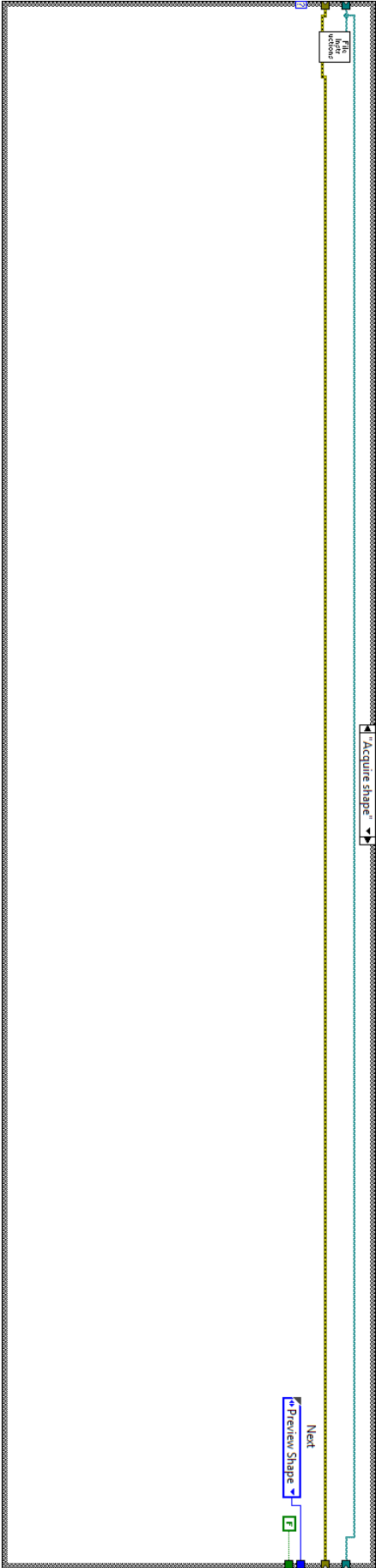


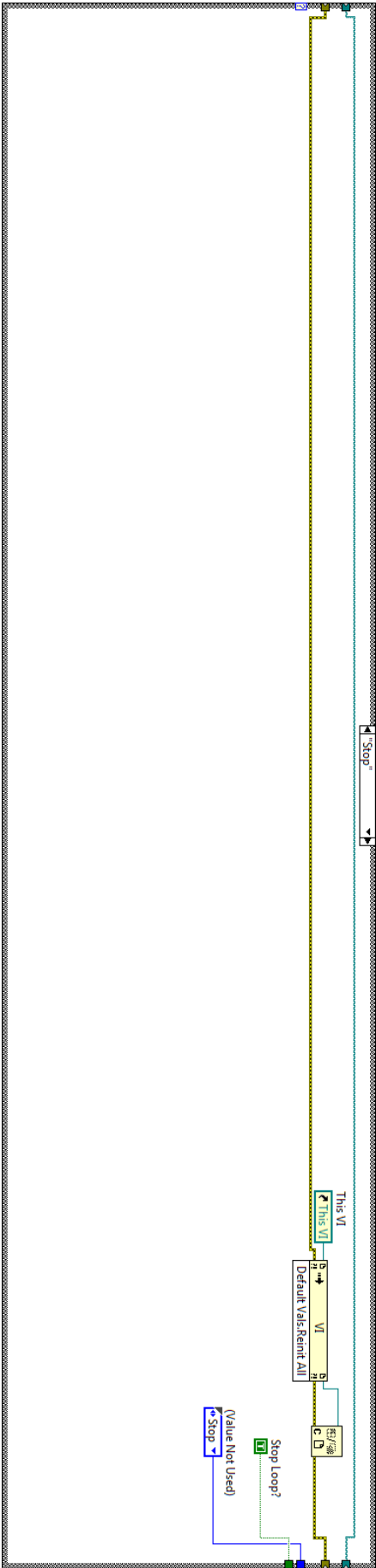




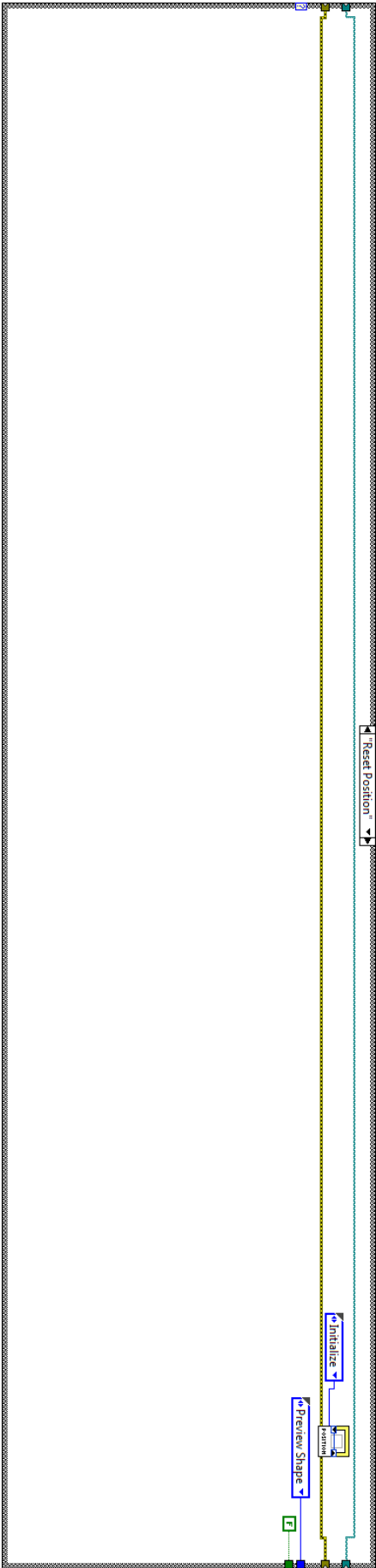












## List of SubVIs and Express VIs with Configuration Information



### Preview.vi

C:\Users\Kovar Lab\Dropbox\X-Y stage\Preview.vi



### Time Delay

Time Delay

Inserts a time delay into the calling VI.

-----

This Express VI is configured as follows:

Delay Time: 0.2 s



### Write Commands.vi

C:\Users\Kovar Lab\Dropbox\X-Y stage\Write Commands.vi



### Cancel FGV.vi

C:\Users\Kovar Lab\Dropbox\X-Y stage\Cancel FGV.vi



### Action Items.ctl

C:\Users\Kovar Lab\Dropbox\X-Y stage\controls\Action Items.ctl



### Instructions FGV.vi

C:\Users\Kovar Lab\Dropbox\X-Y stage\Instructions FGV.vi



### Instructions.vi

C:\Users\Kovar Lab\Dropbox\X-Y stage\Instructions.vi



### Position FGV.vi

C:\Users\Kovar Lab\Dropbox\X-Y stage\Position FGV.vi



### General Error Handler.vi

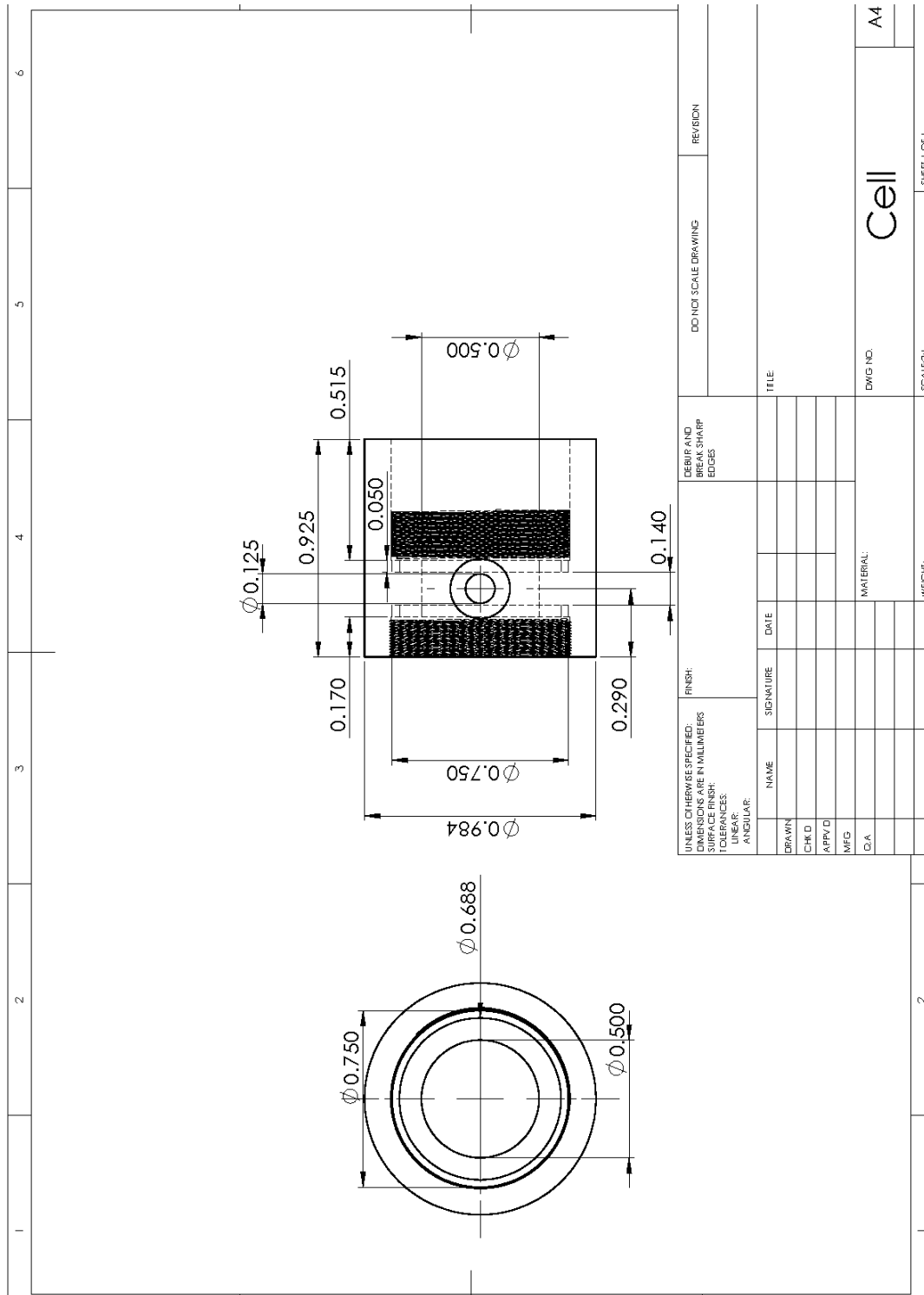
C:\Program Files\National Instruments\LabVIEW 2012\vi.lib\Utility\error.lib\General Error Handler.vi



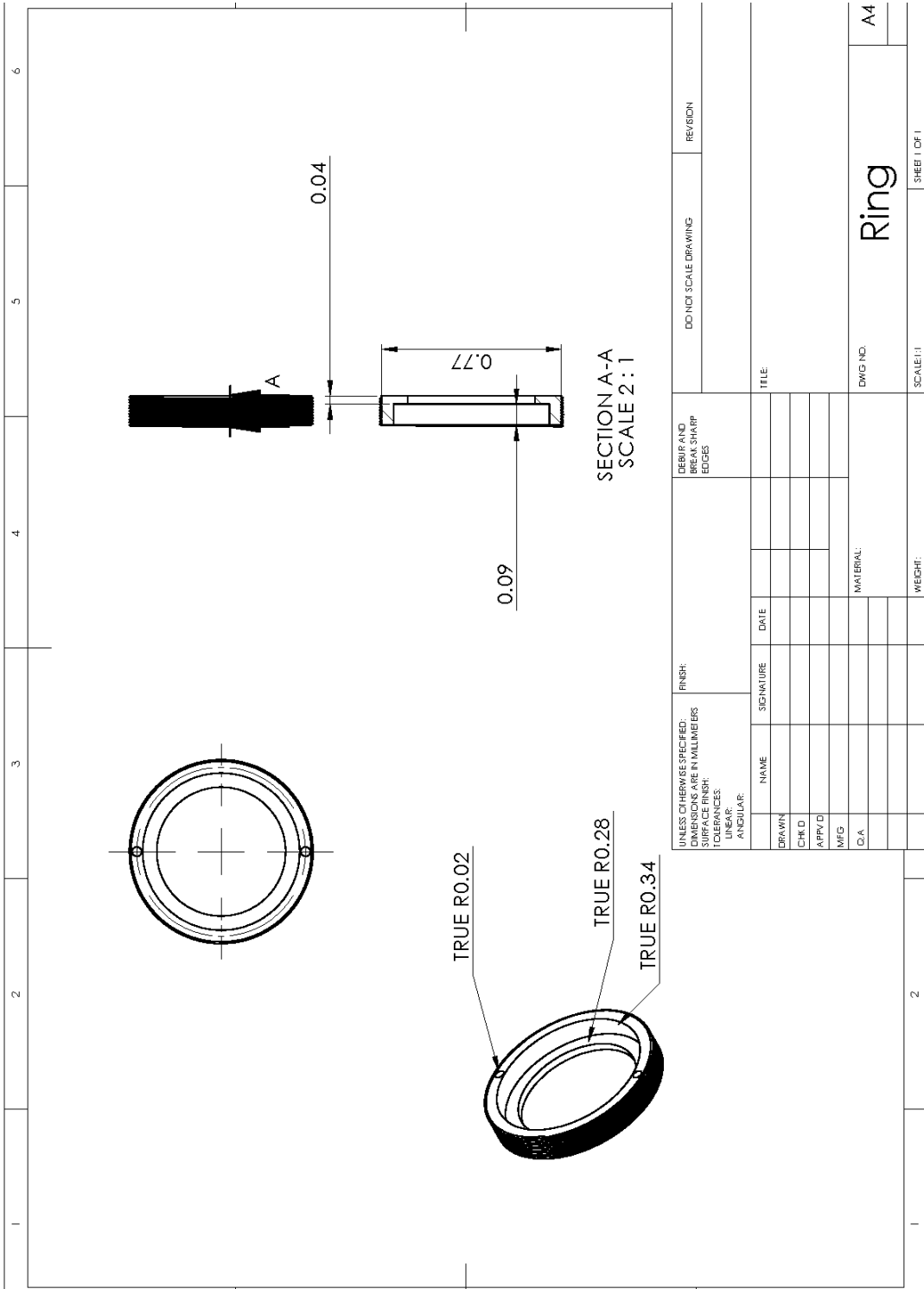
### State\_XY\_Stage.ctl

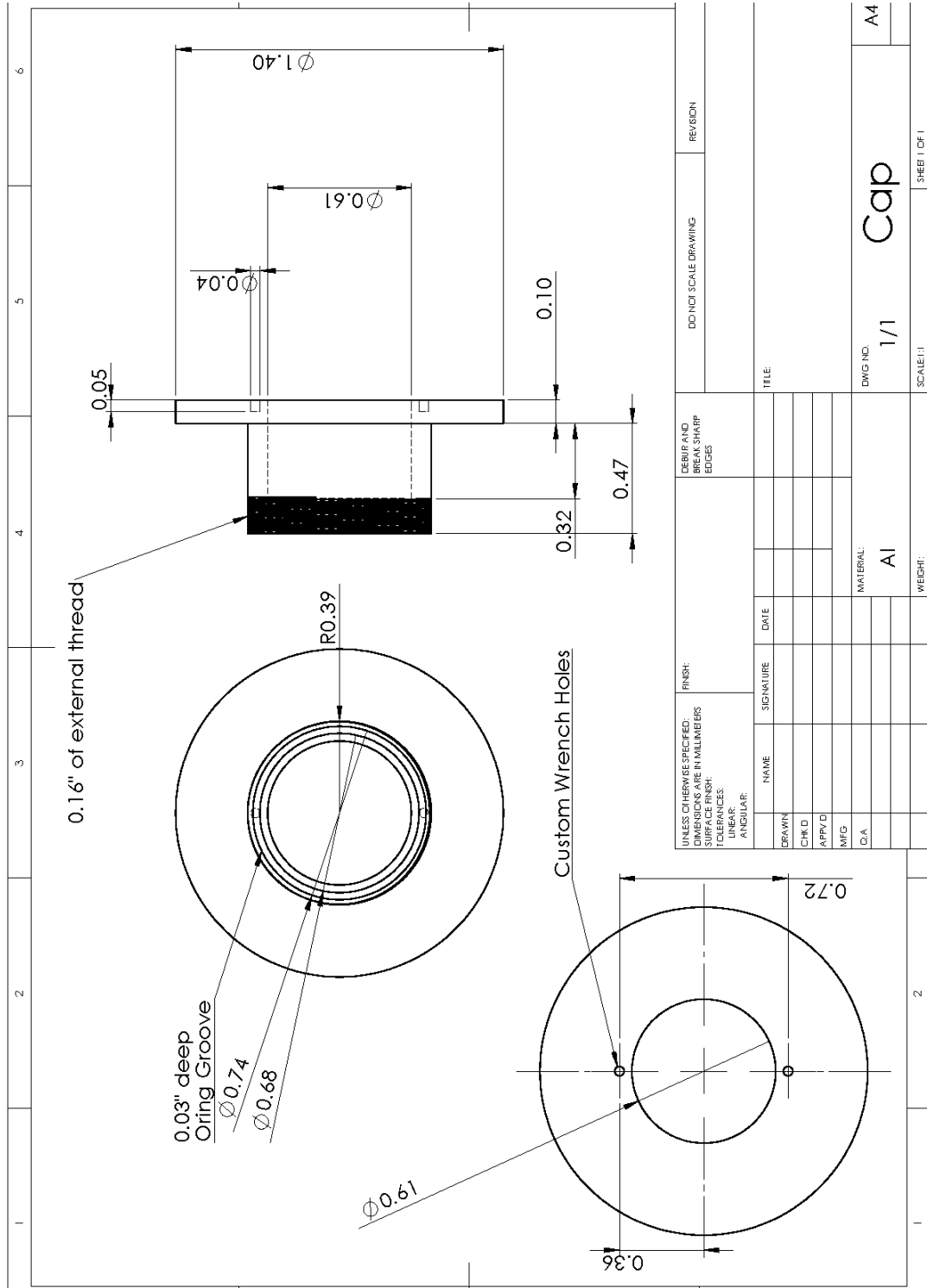
C:\Users\Kovar Lab\Dropbox\X-Y stage\controls\State\_XY\_Stage.ctl

# APPENDIX B: RAMAN GAS CELL SCHEMATICS



UNLESS OTHERWISE SPECIFIED: DIMENSIONS ARE IN MILLIMETERS SURFACE FINISH: TOLERANCES: ANGULAR:		FINISH:		DEBUR AND BREAK SHARP EDGES		DO NOT SCALE DRAWING		REVISION	
DRAWN	NAME	SIGNATURE	DATE			TITLE			
CHK'D									
APP'D									
MFG									
D.A.									
				MATERIAL:		DWG NO.		A4	
						SCALE: 2:1		SHEET 1 OF 1	
						WEIGHT:		Cell	





UNLESS OTHERWISE SPECIFIED: DIMENSIONS ARE IN MILLIMETERS		FINISH:		DEBUR AND BREAK SHARP EDGES		DO NOT SCALE DRAWING		REVISION	
SURFACE FINISH:		TOLERANCES:		MATERIAL:		DWG NO.		A4	
± ANGULAR:		± ANGULAR:		AI		1/1		Cap	
DRAWN		NAME		SIGNATURE		DATE		TITLE	
CHK'D		NAME		SIGNATURE		DATE		TITLE	
APP'D		NAME		SIGNATURE		DATE		TITLE	
MFG		NAME		SIGNATURE		DATE		TITLE	
D/A		NAME		SIGNATURE		DATE		TITLE	
SCALE: 1:1		WEIGHT:		SCALE: 1:1		SHEET 1 OF 1			

## REFERENCES

- [1] Evans, Anna, et al. Review on microfabricated micro-solid oxide fuel cell membranes. *Journal of Power Sources* **2009**, 194.1, 119-129.
- [2] You, Shijie, et al. Forward Osmosis with a Novel Thin-Film Inorganic Membrane. *Environmental science & technology* **2013**, 47.15, 8733-8742.
- [3] Shokouhimehr, Mohammadreza, et al. A magnetically recyclable nanocomposite catalyst for olefin epoxidation. *Angewandte Chemie* **2007**, 119.37, 7169-7173.
- [4] Brown, Michael D., et al. Plasmonic dye-sensitized solar cells using core-shell metal-insulator nanoparticles. *Nano letters* **2010**, 11.2, 438-445.
- [5] Haruta, Masatake. Size-and Support-Dependency in the Catalysis of Gold. *Catalysis Today* **1997**, 36, no. 1, 153–66.
- [6] Shao-Horn, Y; WC Sheng; S Chen; PJ Ferreira; EF Holby; and D Morgan. Instability of Supported Platinum Nanoparticles in Low-Temperature Fuel Cells. *Topics in Catalysis* **2007**, 46, no. 3–4, 285–305.
- [7] Nahar, Manuj. *Oxide-Metal Nanoparticles using Laser Ablation of Microparticle Aerosols*; M.S.E. Thesis: The University of Texas, **2009**.
- [8] Chen, Mingshu and D Wayne Goodman. Catalytically Active Gold on Ordered Titania Supports. *Chemical Society Reviews* **2008**, 37, no. 9, 1860–70.
- [9] Haruta, Masatake, et al. Gold catalysts prepared by coprecipitation for low-temperature oxidation of hydrogen and of carbon monoxide. *Journal of catalysis* **1989** 115.2, 301-309.
- [10] Goodman, DW. Catalytically Active Au on Titania: yet Another Example of a Strong Metal Support Interaction (SMSI)? *Catalysis Letters* **2005**, 99, no. 1–2, 1–4.
- [11] Barnes, William L.; Alain Dereux; and Thomas W. Ebbesen. Surface plasmon subwavelength optics. *Nature* **2003**, 424.6950, 824-830.
- [12] Chen, Weiqiang, et al. Fabrication and optical characterizations of smooth silver-silica nanocomposite films. *Laser Physics Letters* **2010**, 7.9, 677-684.
- [13] Pachón, Laura Durán, et al. Palladium-coated nickel nanoclusters: new Hiyama cross-coupling catalysts. *Physical Chemistry Chemical Physics* **2006**, 8.1, 151-157.
- [14] Evans, Anna, et al. Review on microfabricated micro-solid oxide fuel cell membranes. *Journal of Power Sources* **2009**, 194.1, 119-129.
- [15] Pinnau, Ingo; and Lora G. Toy. Solid Polymer Electrolyte Composite Membranes for olefin/paraffin Separation. *Journal of Membrane Science* **2001**, 184.1, 39-48.
- [16] Pozun, Zachary D.; and Graeme Henkelman. A Model to Optimize the Selectivity of Gas Separation in Membranes. *Journal of Membrane Science* **2010**, 364.1, 9-16.
- [17] Pozun, Z. D.; Tran, K.; Shi, A.; Smith, R. H.; and Henkelman, G. Why Silver Nanoparticles Are Effective for Olefin/Paraffin Separations. *J. Phys. Chem. C* **2011**, 115, 1811-1818.

- [18] Sheth, P. A.; Neurock, M.; and Smith, M. C. First-principles analysis of the effects of alloying Pd with Ag for the catalytic hydrogenation of acetylene-ethylene mixtures. *J. Phys. Chem. B* **2005**, *109* (25), pp 12449–12466.
- [19] Mei, D. and Neurock, M. Effects of alloying Pd and Au on the hydrogenation of ethylene: an *ab initio*-based dynamic Monte Carlo study. *Topics in Catalysis* **2002**, *20*, 1, 5-23.
- [20] Sanders, D. F.; Smith, Z. P. Guo, R.; Robeson, L. M.; McGrath, J. E.; Paul, D. R.; and Freeman, B. D. Energy-Efficient Polymeric Gas Separation Membranes for a Sustainable Future: A Review. *Polymer* **2013**, *54*.18, 4729-61.
- [21] Becker, M. F.; Brock, J. R.; Cai, H.; Henneke, D.; Hilsz, L.; Keto, J. W.; Lee, J.; Nichols, W. T.; and Glicksman, H. D. Metal Nanoparticles Generated by Laser Ablation. *Nanostructured Materials* **1998**, vol. 10, pp. 853-863.
- [22] K. L. Gleason. "Engineering nanocomposite polymer membranes for olefin/paraffin separation," Ph.D. Dissertation: The University of Texas at Austin, **2011**.
- [23] Malyavanatham, G.; O'Brien, D. T.; Becker, M. F.; Keto, J. W.; and Kovar, D. Au/Cu Nanoparticles Produced by Laser Ablation of Mixtures of Au and Cu Microparticles. *J. Nanoparticle Res.* **2004**, 6[6], 661-64.
- [24] Nichols, W.; Keto, J. W.; Henneke, D. E.; Brock, J. R.; Malyavanatham, G.; Becker, M. F.; and Glicksman, H. D. Large-Scale Production of Nanocrystals by Laser Ablation of Microparticles in a Flowing Aerosol. *Applied Physics Letters* **2001**, vol. 78, pp. 1128-1130.
- [25] Nahar, Manuj. "Highly conductive, nanoparticulate thick films processed at low processing temperatures." Ph.D. Dissertation: The University of Texas at Austin, **2012**.
- [26] Nichols, William T.; Malyavanatham, Gokul; Henneke, Dale E.; Brock, James R.; Becker, Michael F.; Keto, John W.; and Glicksman, Howard D. Gas and Pressure Dependence for the Mean Size of Nanoparticles Produced by Laser Ablation of Flowing Aerosols. *Journal of Nanoparticle Research* **2000**, 2.2, 141-145.
- [27] Huang, C.; Nichols, W.; O'Brien, D. T.; Becker, M. F.; Kovar, D.; and Keto, J. W. Supersonic Jet Deposition of Silver Nanoparticle Aerosols: Correlations of Impact Conditions and Film Morphologies. *Journal of Applied Physics* **2007**, 101.6, 064902.
- [28] Zahmakıran, M.; & Özkar, S. Metal nanoparticles in liquid phase catalysis; from recent advances to future goals. *Nanoscale* **2011**, 3(9), 3462-3481.
- [29] Joo, Sang Hoon, et al. Thermally stable Pt/mesoporous silica core-shell nanocatalysts for high-temperature reactions. *Nature materials* **2009**, 8.2, 126-131.
- [30] Zhang, Huigang; Xindi Yu; and Paul V. Braun. Three-Dimensional Bicontinuous Ultrafast-Charge and -Discharge Bulk Battery Electrodes. *Nat Nano* **2011**, 6, no. 5, 277–81.

- [31] Nahar, Manuj, et al. Metal-on-oxide nanoparticles produced using laser ablation of microparticle aerosols. *Journal of Nanoparticle Research* **2011**, 13.8, 3455-3464.
- [32] Gallardo, I.; K. Hoffmann; and J. W. Keto. CdSe & ZnS core/shell nanoparticles generated by laser ablation of microparticles. *Applied Physics A* **2009**, 94.1, 65-72.
- [33] Nichols, William Thomas. *Production and controlled collection of nanoparticles: toward manufacturing of nanostructured materials*. Ph.D. Dissertation: The University of Texas at Austin, **2002**.
- [34] Noiseau, Guillaume Jack Nicolas. *Study of atomic-scale mechanisms for deposition of nanostructured films from nanoparticles*. Ph.D. Dissertation: The University of Texas at Austin, **2015**.
- [35] Akemann, W. and A. Otto. Vibrational frequencies of C<sub>2</sub>H<sub>4</sub> and C<sub>2</sub>H<sub>6</sub> adsorbed on potassium, indium, and noble metal films. *Langmuir* **1995**, 11.4, 1196-1200.
- [36] Le Ru, Eric and Pablo Etchegoin. *Principles of Surface-Enhanced Raman Spectroscopy: and related plasmonic effects*. Elsevier: Amsterdam, 2008.
- [37] Wang, Lianzhou, et al. Synthesis of Mesoporous TiO<sub>2</sub> Spheres under Static Condition. *Chemistry Letters* **2000**, 12, 1414-1415.
- [38] Kresse, G. and Hafner, J. Ab Initio Molecular Dynamics for Liquid Metals. *Phys. Rev. B* **1993**, 47, R558-R561.
- [39] Hohenberg, P.; Kohn, W. Inhomogeneous Electron Gas. *Phys. Rev.* **1964**, 136, 864–871.
- [40] Kohn, W.; Sham, L. J. Self-Consistent Equations Including Exchange and Correlation Effects. *Phys. Rev.* **1965**, 140, 1133–1138.
- [41] Blöchl, P. E. Projector augmented-wave method. *Phys. Rev. B* **1994**, 50, 17953–17979.
- [42] Perdew, J. P.; Wang, Y. Accurate and simple analytic representation of the electron-gas correlation energy. *Phys. Rev. B* **1992**, 45, 13244–13249.
- [43] A. Tkatchenko and M. Scheffler. Accurate molecular Van der Waals interactions from ground-state electron density and free-atom reference data. *Phys. Rev. Lett.* **2009**, 102, 073005
- [44] Perdew, J. P.; Ruzsinszky, A.; Csonka, G. I.; Vydrov, O. A.; Scuseria, G. E.; Constantin, L. A.; Zhou, X.; and Burke, K. Restoring the Density-Gradient Expansion for Exchange in Solids and Surfaces. *Phys. Rev. Lett.* **2008**, 100, 136406.
- [45] Xie, W. and Schlücker, S. Rationally Designed Multifunctional Plasmonic Nanostructures for Surface-Enhanced Raman Spectroscopy: A Review. *Reports on progress in physics*, Physical Society **2014** (Great Britain), 77.11, 116502.
- [46] Guisbiers, G.; Mendoza-Cruz, R.; Bazán-Díaz, L.; Velázquez-Salazar, J. J.; Mendoza-Perez, R.; Robledo-Torres; Rodriguez-Lopez, J.L.; Montejano-Carirzales, J.M.; Whetten, R.L.; and José-Yacamán, M. Electrum, the Gold–Silver Alloy, from the Bulk Scale to the Nanoscale: Synthesis, Properties, and Segregation Rules. *ACS nano* **2015**, 10, 188-198.

- [47] Tang, W.; Zhang, L.; and Henkelman, G. Catalytic Activity of Pd/Cu Random Alloy Nanoparticles for Oxygen Reduction. *J. Phys. Chem. Lett.* **2011**, 2, 1328–1331.
- [48] Koh, S. and Strasser, P. Electrocatalysis on Bimetallic Surfaces: Modifying Catalytic Reactivity for Oxygen Reduction by Voltammetric Surface Dealloying. *J. Am. Chem. Soc.* **2007**, 129, 12624–12625.
- [49] Min, B. K.; W. T. Wallace; and D. W. Goodman. Synthesis of a sinter-resistant, mixed-oxide support for Au nanoclusters. *The Journal of Physical Chemistry B* **2004**, 108.38, 14609-14615.
- [50] M. Asoro; P.J. Ferreira; D. Kovar, In situ TEM and STEM Studies of Sintering of Ag and Pt Nanoparticles. *Acta Mater.* **2014**, 181, 173-183.
- [51] Nahar, Manuj. *Oxide-metal nanoparticles using laser ablation of microparticle aerosols*. Ph.D. Dissertation: The University of Texas at Austin, 2010.
- [52] Atsuko, Tomita; Takeshi, Miki; and Yitaka, Tai. Effect of water treatment and Fe doping on Pt sintering and the propane oxidation activity of Pt/Al<sub>2</sub>O<sub>3</sub>. *Applied Catalysis A: General* **2016**, <http://dx.doi.org/10.1016/j.apcata.2016.04.033>.
- [53] Noiseau, Guillaume Jack Nicolas. *Film deposition and mechanical properties of silver produced by impaction of nanoparticles*. Ph.D. Dissertation: The University of Texas at Austin, **2012**.
- [54] Malyavanatham, Gokul. *Structure and compositional studies of multi-component nanoparticles*. Ph.D. Dissertation: The University of Texas at Austin, **2002**.

## VITA

Michael Drew Gammage, son of Guy Gammage and Rebecca Racca, was born in Sulphur, LA on September 17, 1982. He enlisted in the U.S. Army as an airborne air traffic controller on September 18, 2001. He fought in Iraq in support of the 82<sup>nd</sup> Airborne Division during Operation Iraqi Freedom from September 2003 until April 2004. After an honorable discharge, he moved to Austin, TX to pursue his Bachelors of Science in Physics from The University of Texas at Austin, and graduated in May 2010. In August 2010, he began the Ph.D. program for Materials Science and Engineering at The University of Texas at Austin under the supervision of Dr. Desiderio Kovar.

Email: [gammageatx@gmail.com](mailto:gammageatx@gmail.com)

This dissertation was typed by the author.